



THE HONG KONG
POLYTECHNIC UNIVERSITY

香港理工大學

Pao Yue-kong Library

包玉剛圖書館

Copyright Undertaking

This thesis is protected by copyright, with all rights reserved.

By reading and using the thesis, the reader understands and agrees to the following terms:

1. The reader will abide by the rules and legal ordinances governing copyright regarding the use of the thesis.
2. The reader will use the thesis for the purpose of research or private study only and not for distribution or further reproduction or any other purpose.
3. The reader agrees to indemnify and hold the University harmless from and against any loss, damage, cost, liability or expenses arising from copyright infringement or unauthorized usage.

IMPORTANT

If you have reasons to believe that any materials in this thesis are deemed not suitable to be distributed in this form, or a copyright owner having difficulty with the material being included in our database, please contact lbsys@polyu.edu.hk providing details. The Library will look into your claim and consider taking remedial action upon receipt of the written requests.

Pao Yue-kong Library, The Hong Kong Polytechnic University, Hung Hom, Kowloon, Hong Kong

<http://www.lib.polyu.edu.hk>

**FABRICATION AND CHARACTERIZATION
OF TRANSPARENT OXIDE THIN FILM**

LAM KA KIN

MPhil

The Hong Kong Polytechnic University

2019



The Hong Kong Polytechnic University

The Hong Kong Polytechnic University

Department of Applied Physics

**FABRICATION AND CHARACTERIZATION
OF TRANSPARENT OXIDE THIN FILM**

LAM KA KIN

A thesis submitted in partial fulfillment of the requirements for the
degree of Master of Philosophy

August 2018



Certificate of Originality

I hereby declare that this thesis is my own work and that, to the best of my knowledge and belief, it reproduces no material previously published or written, nor material that has been accepted for the award of any other degree or diploma, except where due acknowledgement has been made in the text.

X

LAM Ka Kin



Abstract

Two types of transparent oxide thin film, namely, transparent ferroelectric thin film and transparent conductive oxide thin film has been studied. These transparent oxide thin films are commonly used in electro-optics applications. In this thesis, these two types of thin films were fabricated by various deposition methods such as pulsed laser deposition (PLD) and magnetron sputtering. Their structural, optical and electrical properties have been investigated.

In the first part of the thesis, strontium barium niobate $\text{Sr}_{0.5}\text{Ba}_{0.5}\text{Nb}_2\text{O}_6$ (SBN) films doped with gadolinium (III) oxide were fabricated. These SBN films were grown epitaxially on either (100) MgO substrates or Pt-coated MgO (100) substrates. The effects of the Gd-doping concentration on the structural and ferroelectric properties of these films were investigated. Besides, the optical properties of the prepared Gd-doped SBN thin films i.e. the refractive index and extinction coefficient were characterized by UV-Vis spectrometer and spectroscopic ellipsometry to retrieve the thickness dependent effects on the optical properties of these films. The thickness dependent optical properties were also studied to fully evaluate the potential application of these films on various optoelectronic devices. The ferroelectric properties of SBN with different Gd-doping concentration were measured by using Pt bottom electrode and Au top electrode. The ferroelectric measurements showed that the 4%-Gd-SBN films had good ferroelectric properties. Ramanent polarization of $+P_r = 1.36 \mu\text{C}/\text{cm}^2$ and $-P_r = -5.73 \mu\text{C}/\text{cm}^2$ and coercive field of $+E_c = 158.0\text{kV}$ and $-E_c = -30.8\text{kV}$ were obtained. Two values of ramanent polarization are reported due to the asymmetric electrode materials has been used, causing the central shifting hysteresis loop.

In the second part of the thesis, transparent conductive oxide Indium Tin Oxide plasmonic devices formed by inserting a thin gold spacer layer in between two ITO thin film i.e ITO/Au/ITO trilayer structure were fabricated. Symmetric Devices (i.e. have same top and bottom ITO layer thickness) with different top and bottom ITO thicknesses were fabricated in this thesis. The structural characterizations showed that the top and bottom ITO layers have different crystallinity due to the



effect of inserted gold spacer. The electrical properties including the carrier concentration, mobility and resistivity were measured by using Van der Pauw configuration, and the optical properties such as refractive index, extinction coefficient and absorption spectra were studied by using spectroscopic ellipsometry and UV-Vis-NIR transmittance measurement. The results showed that increasing ITO thickness can tune the crossover wavelength from the near visible range (830 nm) to near infrared range (1490 nm), corresponding to over 600 nm of plasmonic tuning ability. The performance in different types of plasmonic devices using such multilayer structures were also being evaluated and reported.

Finally, using the asymmetric structure (different in top and bottom ITO thickness in the trilayer structure), we differentiated the thickness contribution on bottom and top ITO layer to the trilayer structure on its electrical and optical properties. The asymmetric structure on the plasmonic properties can be fine-tuned on the epsilon-near-zero (ENZ) regimes.



Acknowledgements

I would like to express my special gratitude to my supervisor Dr. C.L. Mak as well as my co-supervisor Dr. C.W. Leung for their support and guidance.

Also, I would like to show my appreciation to all group members and colleagues for their supports on my two years study, including Mr. K.H. Chan, Mr. W.H. Fung, Dr. Y.K. Liu, Dr. S.M. Ng, Dr. H.F. Wong and Miss K.L. Wong, and Mr. W.F. Cheng for his valuable LabVIEW programs.

Furthermore, I would like to thank all technicians for their technical support on the experiments: Dr. Hardy Lu for the MRC equipment, Dr. Terence Wong for the cleanroom facilities



Table of Contents

Certificate of Originality.....	3
Abstract.....	4
Acknowledgements.....	6
Table of Contents.....	7
List of Figures.....	10
List of Tables.....	14
1 Introduction.....	15
1.1 Background.....	15
1.2 Outline of thesis.....	17
2 Literature review.....	19
2.1 Ferroelectric materials.....	19
2.1.1 Crystal structure of SBN.....	21
2.2 Introduction to the Tin doped Indium Oxide (ITO).....	23
2.3 Physical vapor deposition.....	24
2.4 Optical calcualtion.....	25
3 Experimental method.....	29
3.1 Ceramics PLD target fabrication.....	29
3.2 Pulsed laser deposition (PLD).....	30
Magnetron sputtering.....	31
3.3.....	31
3.4 Structural characterization method.....	33
3.4.1 X-ray diffractometry (XRD).....	33



3.4.2	X-ray Reflectometry (XRR)	35
3.4.3	Atomic Force Microscopy (AFM)	36
3.4.4	Scanning electron microscopy with energy dispersive X-ray spectroscopy (SEM-EDX)	36
3.4.5	Transmission electron microscope (TEM).....	37
3.5	Physical properties measurement method	38
3.5.1	Spectroscopic ellipsometry	38
3.5.2	Electrical and hall measurement	40
3.5.3	UV-Vis spectrometer	43
3.5.4	Polarization-electric field (P-E) hysteresis loop measurement	43
4	Fabrication and characterization of epitaxial Gd-doped SBN thin films	44
4.1	Gd-doped SBN ceramics target characterizations	44
4.2	Gd-doped $\text{Sr}_{0.5}\text{Ba}_{0.5}\text{Nb}_2\text{O}_6$ epitaxial thin film on MgO substrate characterizations.....	48
4.3	Thickness dependence of optical properties in 4% Gd-doped $\text{Sr}_{0.5}\text{Ba}_{0.5}\text{Nb}_2\text{O}_6$ epitaxial thin film on MgO.....	51
4.4	Ferroelectric properties of SBN thin film	59
4.4.1	Structural characterization of SBN thin film ferroelectric capacitors	60
4.4.2	Ferroelectric loop measurement.....	63
5	Characterization of optical and electrical properties of ITO/Au/ITO multilayer thin film ...	69
5.1	Introduction	69
5.2	Structural characterization of ITO/Au/ITO multilayer structures.....	70
5.3	Electrical properties of $\text{ITO}_t/\text{Au}/\text{ITO}_b$ trilayer structure.	75
5.4	Optical properties of $\text{ITO}_t/\text{Au}/\text{ITO}_b$ trilayer structure.	76
5.5	Evaluation of trilayer structure into plasmonic application	87



6	Characterization of optical and electrical properties of ITO/Au/ITO multilayer thin film with asymmetric geometry.....	93
6.1	Introduction	93
6.2	Structural properties on ITO/Au/ITO sandwich film asymmetric geometry	93
6.3	Electrical properties of the asymmetric trilayer structures.....	96
6.4	Plasmonic properties tuning in the asymmetric trilayer structures	102
7	Conclusion and Future work.....	105
	References.....	107



List of Figures

Figure 2-1 the dielectric permittivity ϵ and spontaneous polarization against temperature for (a) first-order and (b) second-order and (c) for a relaxor ferroelectric.[37].....	19
Figure 2-2 Hysteresis loop of ferroelectric materials [38].....	21
Figure 2-3 Projection of the TTB structure into the x-y plane [43].....	22
Figure 2-4 3D schematic diagram of SBN A1, A2 and C lattice with oxygens octahedral [13]..	23
Figure 2-5 Electronic energy band structure of (a) undoped In ₂ O ₃ and (b) Sn-doped In ₂ O ₃ .[48]	24
Figure 2-6 The schematic diagram of the deposit on the substrate [50].....	25
Figure 3-1 Schematic illustration of the pulsed laser deposition (PLD) setup[54].....	31
Figure 3-2 Schematic diagram of the XRD system with different axis of rotations.....	34
Figure 3-3 Schematic diagram of measurement of spectroscopic ellipsometer.	39
Figure 3-4 Schematic illustration of measurement of lateral resistance under magnetic field.	41
Figure 3-5 (Left) Schematic diagram of four-point measurement and (Right) the top view of the positions four points on the thin for measurement.....	42
Figure 4-1 XRD spectra of standard SBN 50 from ICDD database, pure SBN50 and SBN50 doped with 2% and 4% Gadolinium concentrations.....	45
Figure 4-2 XRD patterns of GSBN50 (x=0-0.04) bulk ceramics 2theta angle of (a) (311) plane and (b) (002) plane.....	46
Figure 4-3(a)-(d) SEM image of 4% Gd doped SBN50 target	47
Figure 4-4 XRD spectra of pure SBN50 and Gd doped SBN50thin film grown on MgO (100) substrate.	49
Figure 4-5 Shift of SBN (002) diffraction peak doped with various Gd dopant concentration... 50	50
Figure 4-6 XRD 360° phi-scans of SBN film on MgO (0 0 1) substrate.....	51
Figure 4-7 Observed transmittance spectra 4% Gd-doped SBN50 films with different thicknesses.	52
Figure 4-8 Calculated transmittance spectra 4% Gd-doped SBN50 films by transfer matrix method (TMM).	53



Figure 4-9 The dispersion of refractive index n and extinction coefficient k for 4%-GSBN50 thin film..... 55

Figure 4-10 X-ray reflectivity curve and the fitted curve of 4%-GSBN50 thin film with 5 minutes deposition times. 56

Figure 4-11 (a) The simulated transmittance spectra with different thickness of SBN sample. (b) The comparison of the simulated transmittance and the measured transmittance..... 57

Figure 4-12 Tauc's plot of 4%-Gd doped SBN thin film on MgO substrate with various thickness. 58

Figure 4-13 Schematic diagram of Au/ GSBN50 /Pt device (left) and the 3D structure of crossed bottom and top electrode structure. (right) 60

Figure 4-16 XRD θ - 2θ scan of GSBN50(500nm)/Pt(50nm)/MgO multilayer structure. Inset: ω -scan of SBN (001) and Pt (002)/SBN (002) diffraction peaks. 62

Figure 4-14 XRD phi scan showing epitaxial in-plane relationship of MgO(substrate)/Pt(film)/SBN (film). The substrate tilting at Chi-angle= 54.7° 62

Figure 4-15 Cross-section Field Emission SEM image of SBN/Pt/MgO structure..... 63

Figure 4-17 P-E hysteresis loops of undoped SBN and doped with Gd film measured at 1kHz with applied an electric field, $E = 20\text{kV/cm}$ 64

Figure 4-18 The P-E hysteresis loop of 4% Gd-doped SBN thin film with the varied electric field. 65

Figure 4-19 optical micrograph of the ferroelectric junctions. 66

Figure 4-20 The P-E hysteresis loop of ferroelectric device with 500nm active layer (a) 1%Gd-doped SBN film, (b) 2%Gd-doped SBN film and (c) 4%Gd-doped SBN film..... 67

Figure 4-21 Frequency dependence of the relative dielectric constant ϵ_r and dielectric loss of the different Gd doped SBN thin film grown on Pt/ MgO substrate. 68

Figure 5-1 XRR pattern of ITO (t nm)/Au (2.9 nm)/ITO (t nm) trilayer films with varying values of t. 71

Figure 5-2 (a) Cross-sectional TEM of the ITO (20 nm)/Au (3 nm)/ITO (20 nm) sample. (b) Selected-area diffraction patterns of top ITO layer, showing the polycrystalline structure. 72



Figure 5-3 (a) XRD pattern of ITO/Au/ITO trilayer with different ITO layer thicknesses (both top and down ITO thickness in trilayer structure remain the same). (b) X-ray diffraction pattern of ITO ceramic target. 73

Figure 5-4 FWHM of (400) peak of ITO/Au/ITO multilayers against top ITO thickness 74

Figure 5-5 carrier concentration, Hall mobility and resistivity as a function of ITO thickness ... 75

Figure 5-6 The schamitioc diagram of reflection ellipsometry 77

Figure 5-7 Real (solid symbol) and imaginary (open symbol) parts of permittivity against wavelength of Top ITO layer in the trilayer samples. 78

Figure 5-8 ψ and Δ of the ITO (22 nm)/Au (3 nm)/ITO (22 nm) sample measured by spectroscopic ellipsometry in the 400-2000 nm wavelength range..... 79

Figure 5-9 real (solid symbol) and imaginary (open symbol) parts of permittiity against wavelength of bottom ITO layer in the trilayer samples..... 79

Figure 5-10 The permittivity profile of gold thin film..... 80

Figure 5-11 crossover wavelength of bottom and upper ITO layers 80

Figure 5-12 ϵ_{\perp} with the real part (solid symbol) and the imaginary part (open symbol) of the trilayer layer samples calculated by effective medium approximation. 82

Figure 5-13 crossover wavelength as a function of bottom and top ITO thickness in the trilayer sample. 83

Figure 5-14 The effective refractive index and extinction coefficient of trilayer structure..... 84

Figure 5-15 schamatic diagram of TMM modeling trilayer structure by effective media approximation (EMA)..... 85

Figure 5-16 Schematic diagram of the simulated of ITO/Au/ITO layer by layer structure. 85

Figure 5-17 (a)spectral transmittance of trilayer samples with different top and bottom ITO thickness. (b) Simulation of transmittance of ITO/Au/ITO trilayer structure by Effective media approximation (EMA). (c) Simulation of transmittance of ITO/Au/ITO trilayer structure blayer by layer..... 86

Figure 5-18 . Quality factors of the trilayer samples for localized surface plasmon resonances (Q_{LSPR})..... 88

Figure 5-19 Schematic diagram of surface plasmon propagation and the related parameters.[102] 89



Figure 5-20 (a) Spatial profile of SPP for ITO–Au–ITO film and silicon substrate interface: (a) quality factors Q_{SPP} , (b) propagation length δ_{prop} , (c) SPP wavelength and (d) degree of confinement δ_{conf} 90

Figure 6-1(a) XRR pattern of ITO (40-t nm)/Au (3 nm)/ITO (t nm) asymmetric trilayer structures. (b) XRR pattern of ITO (20-t nm)/Au (3 nm)/ITO (t nm) asymmetric trilayer structures 94

Figure 6-2 (a) XRD pattern of ITO/Au/ITO trilayer with different ITO layer thicknesses (both top and down ITO thickness in trilayer structure remain the same). (b) XRD pattern of ITO/Au/ITO trilayer with different top and bottom ITO thicknesses (total thicknesses are 43nm). (c) XRD pattern of ITO/Au/ITO trilayer with different top and bottom ITO thicknesses (total thicknesses are 23nm). 96

Figure 6-3 Schematic diagram of the electrical properties of TCO/metal/TCO multilayer structures. 97

Figure 6-4 The schematic representation of the thickness variation on the asymmetric samples. 98

Figure 6-5 The electrical properties of asymmetric samples with only bottom layer thickness increment from 15nm to 60nm (black curve, bottom and left axis), the top ITO and gold layer was kept 5nm and 3nm respectively and only top layer thickness increment from 15nm to 60nm (colored curve, top and right axis), the bottom ITO and gold layer was kept 5nm and 3nm respectively. 100

Figure 6-6 carrier concentrations, Hall mobility and resistivity as a function of ITO top layer thickness (a) different top and bottom ITO thicknesses (total thicknesses are 23nm), (b) different top and bottom ITO thicknesses (total thicknesses are 43nm). 101

Figure 6-7 effective dielectric constant ϵ_{\perp} with the real part(solid line) and the imaginary part (dashed line) of the trilayer layer samples with different position of gold spacer layer calculated by effective medium approximation (a) different top and bottom ITO thicknesses (total thicknesses are 23nm), (b) different top and bottom ITO thicknesses (total thicknesses are 43nm). 103

Figure 6-8 (a) Epsilon near zero (ENZ) region of ϵ_{\perp} with the real part (solid line) of the trilayer layer samples with different position of gold spacer layer (total thicknesses are 43nm). (b) crossover wavelength against the position of inserted gold layer (total thicknesses are 43nm). (c) Epsilon near zero (ENZ) region of ϵ_{\perp} with the real part (solid line) of the trilayer layer samples



with different position of gold spacer layer (total thicknesses are 23nm). (d) crossover wavelength against the position of inserted gold layer (total thicknesses are 23nm). 104

List of Tables

Table 3-1 the mass of the powder for ceramic preparation. 30

Table 3-2 The interplanar spacing of different lattice system 34

Table 4-1 The lattice parameter of GSBN ceramics with different Gd³⁺ doping concentration .. 46

Table 4-2 The composition variation of the 4% Gd doped SBN targets at different position..... 47

Table 4-3 Calculated value C-lattice constant against the doping concentration 50

Table 4-4 Sellmeier parameters for the SBN indices of refraction..... 53

Table 4-5 The coercive field (E_c) and remnant polarization (P_r) as a function of the Gd-doping concentration..... 64

Table 5-1 the ITO depostion time and the trilayer thickness obtained fome the XRR measurment. 70

Table 5-2 Comparison of quality factors of three different plasmonic devices with different materials. The quality factor of 1.5 μm indicate the nanophotonic applications. (IAI structure data ends at 2 μm)[97] 92

Table 6-1 The deposition time and the ITO (top and bottom) thickness of (40-t nm)/Au (3 nm)/ITO (t nm) asymmetric structures. 94

Table 6-2 The deposition time and the ITO (top and bottom) thickness of (20-t nm)/Au (3 nm)/ITO (t nm) asymmetric structures. 94



1 Introduction

1.1 Background

Optoelectronic devices are a new branch of electronic devices based on the quantum mechanical behavior of light on electronic materials which is usually an interplay between electronic and optics, for example, photodiode, photodetector, photovoltaic device, optical modulator, light emitting diode(LED) and laser diode.[1] The dominated role on the photonic and optoelectronic devices in modern electronic applications, increase demand of the transparent and optical active materials. Beside the basic functions, the optoelectronic devices also required multifunctionalities nowadays. The addition of new functional material should not perturb the light transmission on the devices, which shows the importance of the transparent functional materials.[2, 3]. The transparent conductive oxides have long been used as an electrode on LED and solar cell instead of metal due to their electrical conductivity and optical transparency. Recent researches have suggested the integration of transparent piezoelectric ceramics on glass transducer which opens a new area of research on the transparent ferroelectric devices.[4]

The transparency is a fundamental physical property related to the light absorption by the materials. In modern physics, due to the wave-particle duality principle, the electromagnetic wave can be quantized as a photon incident on a solid-state material, the absorption of photon with certain wavelength is governed by the bandgap. If the photon energies are not large enough to excite the electron to occur the interband transition, the photon will pass through the material and the material appears to be transparent at that wavelength.

Strontium barium niobate $Sr_xBa_{1-x}Nb_2O_6$ (SBN:x) is a transparent ferroelectric material possessing tungsten bronze structure with wide range of dielectric, piezoelectric, pyroelectric and ferroelectric properties that applied into various electronic devices such as pyroelectric infrared sensor [5] and pyroelectric nanogenerator [6]. Apart from electronic applications, SBN is a promising material to be applied into optical applications, for example, optical waveguide[7] and electro-optic modulator[8] due to its extraordinary large electro-optic



coefficient[9-12] and photorefractive properties[13]. The advantage of transparent ferroelectric is that the optical characteristics can be controlled by applying electric field or any external action such as induced strain[14].

Moreover, the SBN crystal shows a great variability in the physical properties by controlling the structural properties such as changing the Sr/Ba ratio[15, 16] or doping rare earth elements.[17-19] To achieve better optical and ferroelectric properties of SBN, single crystal usually maintains better properties, however, fabricating process of single crystal SBN is challenging and costly, the product has poor mechanical strength make it difficult for practical applications. To address this problem, most of the studies will investigate the properties of ceramic and thin film SBN.[20, 21]

This project will focus on the fabrication of thin film heterostructure on gadolinium doped SBN50. The effects of rare earth dopant introduced into SBN bulk ceramic in improving the ferroelectric and pyroelectric properties had been widely investigated. Yao et al. reported that the Gd dopant can extraordinarily improve the pyroelectric coefficient of SBN ceramic by three times compared with other rare earth dopants at room temperature range.[17] The Gd dopant chosen not only showed an enhancement on the ferroelectric properties, but we also explored the optical properties modification by introducing Gd ions.

On the other hand, another type of transparent materials that extensively used in electronic and optoelectronic devices is the transparent conductive oxide (TCO). Comparing with conventional metal-based electrode, TCO preserves two key parameters strongly related to the performance of a device i.e. electrical conductivity and optical transparency. Even though the optical transparency can still be achieved by depositing an ultra-thin metal layer, there will be a trade-off between its electrical conductivity. According to the Lambert-beer law $T = e^{-\alpha t}$, the optical transparency T can be increased by reducing film thickness, where α and t are the absorption coefficient of the material and its film thickness respectively. However, the reduced thickness will generally increase the sheet resistance, according to Ohm's law $R_{Sheet} = \frac{1}{\sigma t}$. [22] Here R_{Sheet} is the sheet resistance and σ is the conductivity. Furthermore, the electrical conductivity of most of the metals such as copper will be degraded for long time exposure in air due to the oxidation process; while using noble metal such as gold and platinum will rapidly raise the costs of electronic devices. Those properties of metals will limit their application in optoelectronic devices.



Therefore, transparent conductive oxide is another choice for most of the optoelectronic device because of the optical transparency, electrical conductivity and oxidation resistance properties. The most common TCOs are the doped metal oxide such as Aluminum or Gallium doped Zinc oxide (AZO or GZO)[23, 24], Fluorine or Indium doped Tin Oxide (FTO or ITO),[25, 26] and Indium doped Magnesium Zinc oxide (IMZO) etc. [27, 28] These TCOs usually have a wide bandgap (> 3 eV), so that they have a high transparency in visible spectral range. Their electrical conductivities stem from the generation of oxygen vacancies, defects from interstitial site and the assisted carrier transported by introducing the metal dopants.[22] Especially, ITO has been used commercially for large-scale application and becomes a dominant role in most of the optoelectronic devices such as flat panel displays[29].

Even though TCO can reduce the overall cost from the materials viewpoint, it is still costly in the deposition processes of TCO. Since a high quality TCO thin film required various high energy deposition process such as pulsed laser deposition and magnetron sputtering. Also, usually TCO shows poor mechanical properties and environmental stability, and this limits the TCO to be applied into flexible optoelectronic devices. To address these problems, Fan et al. first proposed the multilayer structures to further improve the properties of TCO. [30] Then, TCO/Metal/TCO structures have been extensively studied on various TCO structures to obtain electrodes with better performance. An ultra-thin noble metal layer (e.g. Au and Ag) inserted between two TCO layers can introduce more free carriers for TCO electrode to reduce the resistivity of the whole structures, and at the same time the transparency can also be preserved. [31-33] Additionally, the ductility of metallic layer can give extra mechanical flexibility to this TCO structure, so that these structures can be applied into flexible electronic.[34, 35]

This thesis aims to explore the transparent oxide material individually including transparent ferroelectric oxide SBN and transparent conductive oxide ITO in the dielectric, ferroelectric and electrical properties by rare earth element doping and geometrical modification. From the result, the potential application will be further elaborated.

1.2 Outline of thesis

In chapter 1, an overview on the modern optoelectronic devices and the role of transparent oxide including the optoelectronic usage, the problem encountered current situations will be discussed. Then, a brief introduction will focus on transparent ferroelectric SBN and



transparent conductive oxide ITO. Finally, the possible outcomes on this project will be covered.

In chapter 2, the literature review on the topics related to the research project, for example, the structural properties of SBN, the origin of the ferroelectricity. The ITO crystal and the conduction mechanism of TCO will be introduced. Also, the optical properties related to basic electronic and the plasmonic properties will also be discussed.

In chapter 3, the experimental method will be discussed including the fabrication method of the materials such as Gd-doped SBN ceramic target prepared by solid-state reaction method, thin films deposited by pulsed laser deposition and magnetron sputtering, and devices fabricated by various microfabrication techniques like UV-lithography. Also, the common structural characterization methods will also be included in this chapter, for example the X-ray diffractometry (XRD), X-ray reflectometry (XRR), atomic force microscopy (AFM), scanning electron microscopy with energy dispersive X-ray spectroscopy (SEM-EDX) and transmission electron microscope (TEM), the working mechanisms and the operation procedures of each instrument will be covered in the discussion. Finally, the physical mechanism and procedure of post-fabrication physical properties measurement will also be covered. Furthermore, the measurement of thin film electrical properties by hall measurement with Van der Pauw configuration, optical properties characterization by spectroscopic ellipsometry and UV-Vis-NIR spectrometry and the ferroelectric hysteresis measurement will be covered.

In chapter 4, the experimental result of transparent ferroelectric SBN will be presented. The structural and composition characterizations of ceramic target are included. Then, the discussion will be focused on the SBN thin film by constructing the optical model of SBN film using spectroscopic ellipsometry. The SBN films have been fabricated as a heterostructure ferroelectric capacitors to measure the ferroelectric properties. The in-plane relationship of these heterostructure were investigated by XRD phi scan.

In chapter 5, the scope of discussion will be focused on the ITO, a type of transparent conductive oxide. The electrical and optical properties were modified by inserting an ultra-thin gold layer and characterized by using electrical measurement and spectroscopic ellipsometry. And the potential application on various plasmonic devices will also be discussed.

2 Literature review

2.1 Ferroelectric materials

The terms ferroelectric comes from the analogy of ferromagnetic because the ferroelectric materials have similar properties as the ferromagnetic materials. Under external magnetic field, a ferromagnetic material will exhibit spontaneous magnetization due to the special electronic configuration of iron atom or any element with unpaired electronic orbital, where the prefix Ferro- means iron in Latin. However ferroelectric material does not require iron atoms, ferroelectric only borrow the concept which exhibit spontaneous electric polarization under external electric field. The spontaneous polarization means that the ferroelectric material will gain a net dipole moment and align along external electric field. The net dipole will still exist even the electric being removed. [36] The ferroelectricity stem from the crystal structures. There are 32 classes of the crystal symmetry point groups and 21 of them are non-centrosymmetric, the rest are centrosymmetric. Only 10 groups of non-centrosymmetric structures will show the ferroelectricity. The common material that exhibit the ferroelectric properties have: i) perovskite structure, ii) bismuth oxide layered structure or iii) tetragonal tungsten bronze structure.

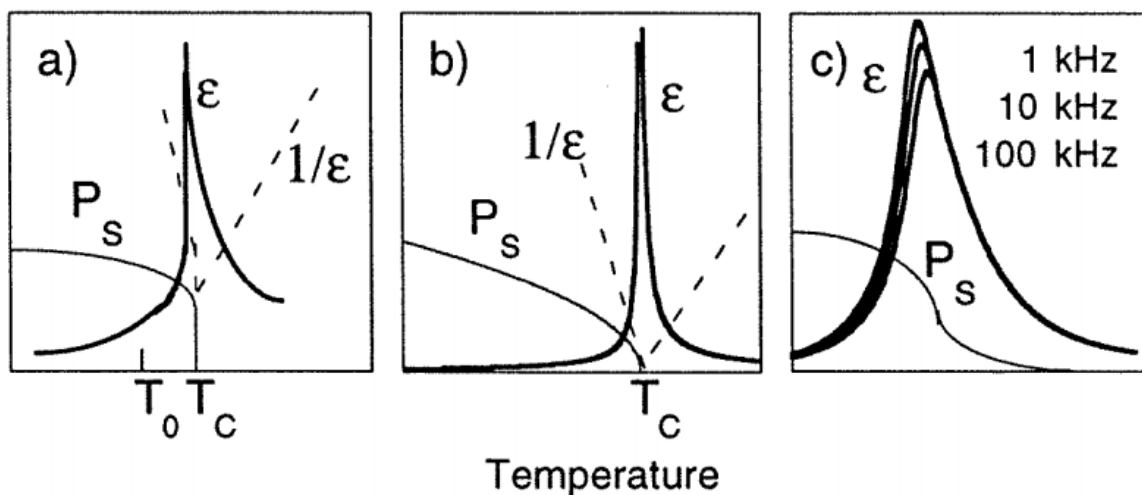


Figure 2-1 the dielectric permittivity ϵ and spontaneous polarization against temperature for (a) first-order and (b) second-order and (c) for a relaxor ferroelectric.[37]



The material only shows its ferroelectricity below the Curie temperature T_c . Beyond the Curie temperature, the ferroelectric material will become paraelectric and no longer exhibits ferroelectricity as shown in Figure 2-1, which is called the ferroelectric phase transition. The spontaneous polarization P_s will drop rapidly and the dielectric constant ϵ_r attain the maximum value near T_c . such behaviour can be described by the Curie-Weiss law:

$$\epsilon_r = \frac{C}{T - T_c} \quad (2.1)$$

where C is the curie constant.

The ferroelectric materials can be characterized by the hysteresis loop i.e. the ferroelectric materials are being poled by an AC electric field. The ferroelectric response will be similar to the hysteresis loop shown in Figure 2-2. The polycrystalline domain will align along the applied electric field resulted in polarization. When the applied electric field is small, the electric polarization is proportional to the field applied. If electric field further increase, the pinning by grain boundaries on polycrystalline material or the clamping by substrate on thin film will restrict the alignment of domain, resulting in the saturation polarization and attaining the maximum polarization attained. After the removal of electric field, most of dipole will restore to its original directions, some the electric dipole, however, unable to restore its original orientation, which gives the remnant polarization and the extra external field required to switch all the dipole into original alignment is called the coercive field.

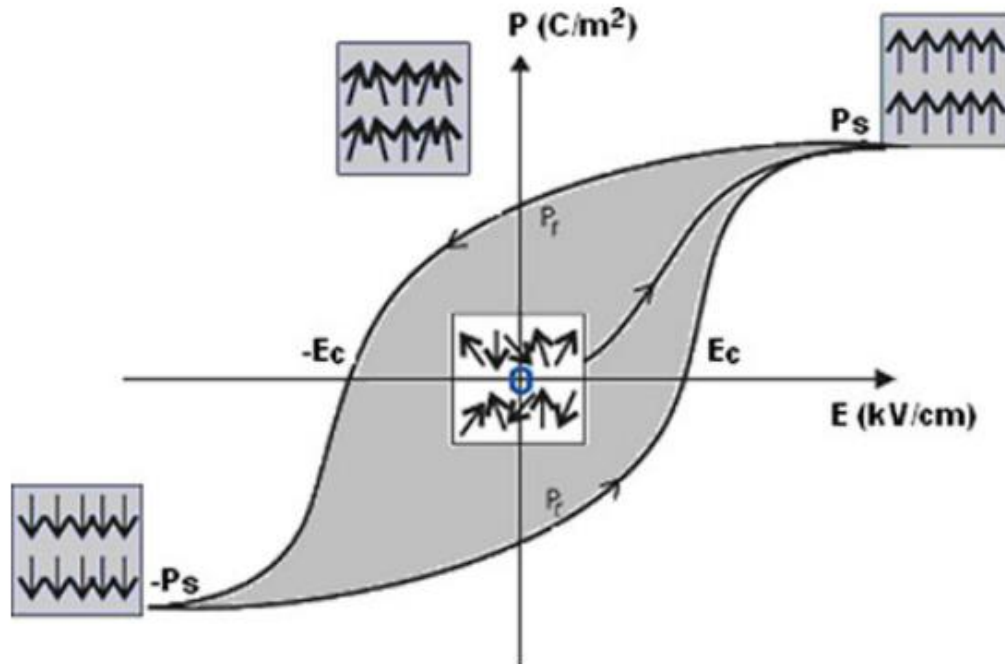


Figure 2-2 Hysteresis loop of ferroelectric materials [38]

2.1.1 Crystal structure of SBN

Strontium barium niobite $\text{Sr}_x\text{Ba}_{1-x}\text{Nb}_2\text{O}_6$ (SBN) is a relaxor ferroelectric material with tetragonal tungsten bronze (TTB) structure belonging to the $P4bm$ space group. It is a solid solution of SrNb_2O_6 (SNO) and BaNb_2O_6 (BNO) in the range from $x = 0.25$ to 0.75 composition. The term relaxor means that SBN possesses a diffused phase transition under dielectric measurement at different frequency.[39] The general chemical formula of TTB structure is $(A1_x, A2_{1-x}, C) M_2O_6$. [15] The Sr^{2+} and Ba^{2+} cations occupy the A1 and A2 sites respectively, and the C sites remain vacant. As shown in Figure 2-3 and Figure 2-4, the A1, A2 and C sites are formed by the oxygen octahedral with Nb atoms at the center. Pentagonal (square) A1 (A2) lattice site formed by five oxygen octahedral occupied either Sr or Ba atoms surrounded by 15 (12) nearest-neighbour oxygens. The trigonal C lattice site formed by three oxygen octahedral with 9 nearest-neighbour will remain vacant for pure SBN lattice. The properties of SBN is strongly dependent on the ratio of Sr/Ba ions, by the continuous variation of the Sr/Ba ratio, the curie temperature of SBN can be changed from 60 to 250 °C. [40] various studies showed that the ferroelectric properties of SBN attain the greatest value when the Sr to Ba ratio approximate to be even.[41] The TTB structure of SBN provides a great variability for

structural modification by changing the ratio of Sr/Ba cations. It also provides potential modifications in the designated composition of SBN ceramic by substituting the rare-earth to the A1 and A2 site [18, 19, 42] or adding small cations such as sodium and potassium into the interstitial C-site.

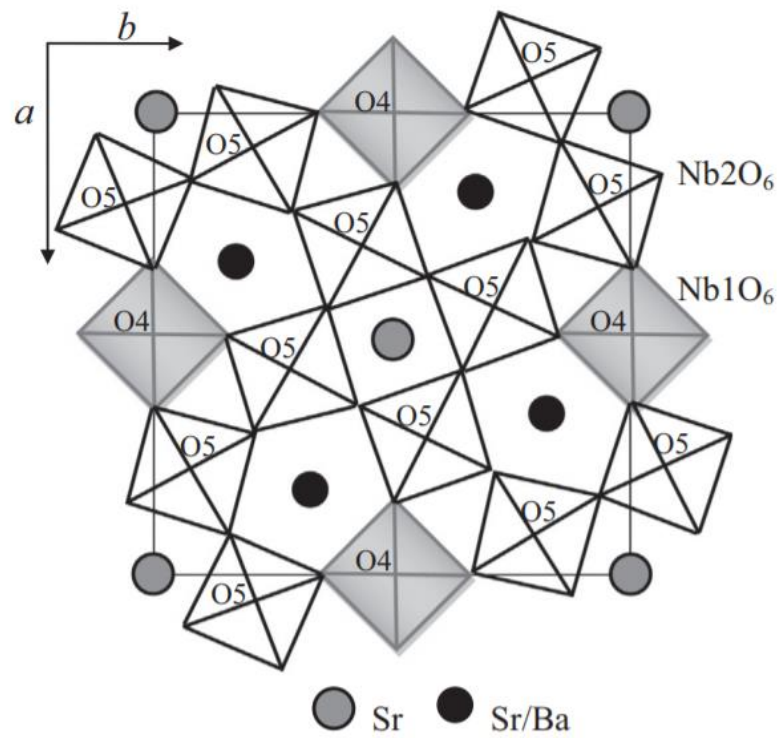


Figure 2-3 Projection of the TTB structure into the x-y plane [43]

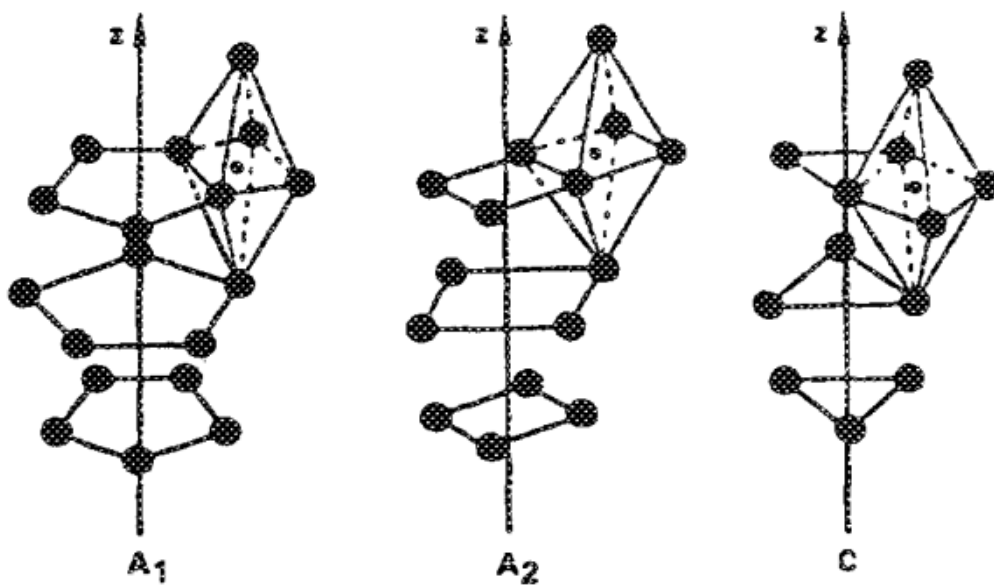




Figure 2-4 3D schematic diagram of SBN A1, A2 and C lattice with oxygens octahedral [13]

2.2 Introduction to the Tin doped Indium Oxide (ITO)

Indium Tin Oxide is a n-type transparent conducting oxide (TCO), which is conductive under room temperature and pressure. TCO preserves high transmittance in the visible wavelength i.e. transparent. This two main properties, namely electrical conductivity and optical transparency, help ITO being used in different electronic and optoelectronic devices.

Many fabrication techniques have been used to grow ITO thin film, including pulsed laser deposition (PLD), magnetron sputtering, e-beam evaporation, sol-gel, chemical vapor deposition and spray pyrolysis. Result showed that ITO properties are strongly depended on the fabrication techniques and deposition conditions.[44] Using magnetron sputtering as an example, ITO films show great variability in different sputtering conditions such as chamber base pressure, sputtering power, film thickness and deposition media gas pressure. [45, 46]

The fundamental conduction mechanism of ITO can be explained by its electronic band structure. The formation of the conduction band in the ITO is derived from the hybridization of Oxygen 2p state and Indium 5s state forming a free-electron like parabolic s state.[47] As shown in Figure 2-5, The Sn-doping provide additional 5s orbital to further hybridize the s-orbital of In and O states, forming a new conduction band minimum which the conduction band minimum is lower than the Fermi level (E_F) to help ITO becoming a n-degeneracy semiconductor . [48]

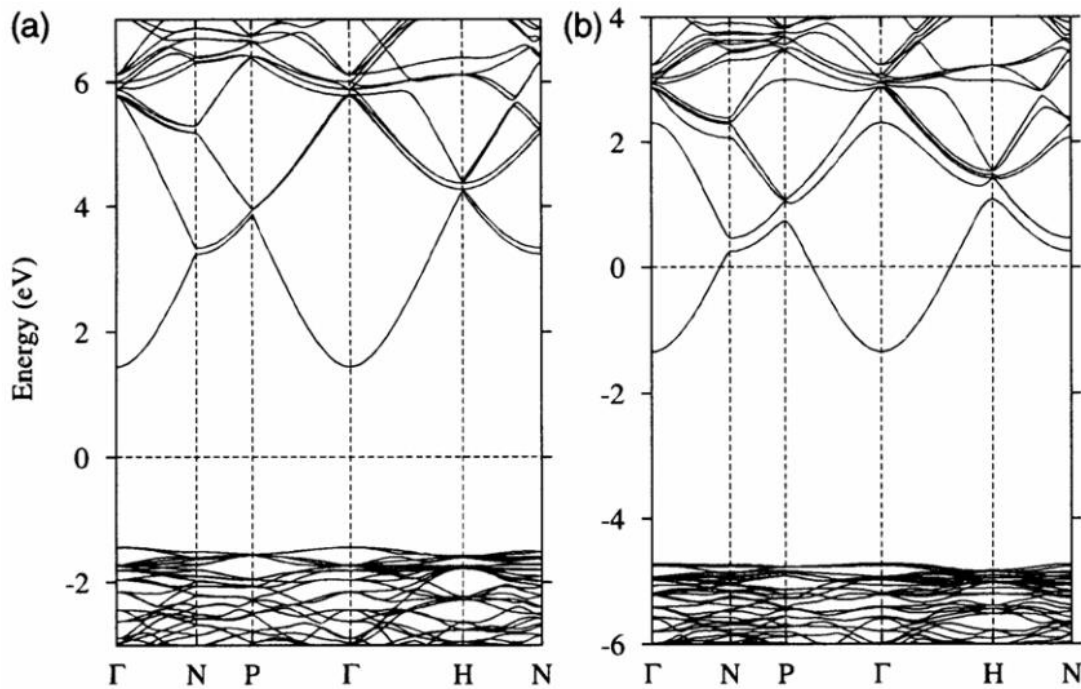
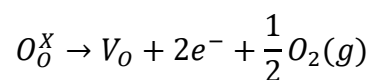


Figure 2-5 Electronic energy band structure of (a) undoped In_2O_3 and (b) Sn-doped In_2O_3 . [48]

Also, another conduction mechanism is the oxygen vacancies existed inside the non-stoichiometric indium oxide. The oxygen vacancies band will overlap with the bottom of the conduction band at high vacancy concentrations. The vacancies can provide at maximum two electrons to conduct electricity. The vacancies not only provides the conduction, but also acts as the mobilied O^{2-} ions for the conduction. [49]



2.3 Physical vapor deposition

Thin film deposition methods are mainly divided into three categories: physical deposition, chemical deposition and mixed deposition.

The physical vapour deposition process produces the gaseous state vapour using physical method without changing the materials chemical properties, for example laser ablation, thermal or electron beam evaporation, and sputtering.

The thin film growth modes are classified into three mechanisms: the Volmer-Weber growth (the three-dimensional island growth mode), the Frank-van der Merwe growth (the two-

dimensional layer growth mode) and the Stranski–Krastanov growth (2D layer growth initially, then 3D island growth).[50]

The growth mode is determined by the interfacial energy between the deposited material and substrate. The relation is given below:

$$\gamma_B = \gamma^* + \gamma_A \cos \varphi \quad (2.2)$$

where γ_B is the substrate tension, γ_A is the tension of droplet and γ^* is the interfacial tension of the droplet and substrate, and the φ is the angle between surface and droplet (illustrated on Figure 2-6 The schematic diagram of the deposit on the substrate). If $\varphi > 0$, which means $\gamma_B < \gamma^* + \gamma_A$, the island growth mode will be favoured. On the other hand, if $\gamma_B \geq \gamma^* + \gamma_A$, the layer growth will take place. Then, the Stranski–Krastanov growth is the combination of the previous two growth modes. Initially the layer by layer growth is favoured because deposit relaxation reduce the lattice misfit with the substrate. After the substrate surface being covered, the adhesive force is smaller than the elastic force, the droplets will therefore cluster to favour island growth. The Frank–van der Merwe growth usually occur on the growth of ultra thin film and the Stranski–Krastanov growth is usually the growth mode of thick film (>100nm).

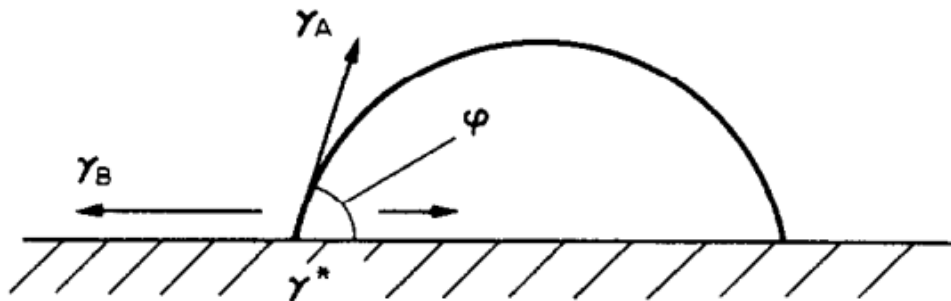


Figure 2-6 The schematic diagram of the deposit on the substrate [50]

2.4 Optical calculation

The optical properties of a material stem from the interaction between the electrons and external electric field. From Maxwell Equations, the nature of light is the oscillation of electric field and magnetic field. When light shines on a material, in macroscopic point of view, it will either be reflected, transmitted or absorbed, those properties depend on the optical properties



of the materials such as refractive index and extinction coefficient. In microscopic aspect, the electrons are actually driven to oscillate by the incident electromagnetic waves. The electron oscillation model is described by Fox.[51]

For the nearly free electron in metals or free carrier in semiconductors, the dielectric function is usually described by the Drude-Lorentz model, the dynamic of the electron can be described by the following equation of motion under an external electric field $E_0 e^{-i\omega t}$:

$$m_e \frac{d^2 x}{dt^2} + m_e \Gamma \frac{dx}{dt} + kx = -eE_0 e^{-i\omega t} \quad (2.3)$$

Here m_e is the effective mass of electron in the material and Γ is the scattering term and k is the coulombic force constant. Assuming the driving frequency ω is far from the band gap frequency, thus there is no interband transition. The harmonic oscillator term kx would be zero when the motion of electron treated as nearly free electron and did not bounded to particular atom. The solution of the equation is given by substituting $x = x_0 e^{-i\omega t}$

$$x(\omega) = \frac{-e}{m_e} \frac{E_0}{(\omega^2 + i\Gamma\omega)} \quad (2.4)$$

The polarization of the electron gas is $P = -Nex(\omega)$, where N is the electron density. By definition, the electric displacement D is related to the electric polarization P and relative permittivity ϵ_r

$$\begin{aligned} D &= \epsilon_r \epsilon_0 E = \epsilon_0 E + P \\ &= \epsilon_0 E - \frac{Ne^2}{\epsilon_0 m_e} \frac{E_0}{(\omega^2 + i\Gamma\omega)} \end{aligned} \quad (2.5)$$

Therefore the relative permittivity will be given by :

$$\epsilon_r(\omega) = 1 - \frac{Ne^2}{\epsilon_0 m_e} \frac{1}{(\omega^2 + i\Gamma\omega)} = 1 - \frac{\omega_p^2}{(\omega^2 + i\Gamma\omega)} \quad (2.6)$$

Here we define the plasma frequency ω_p :

$$\omega_p = \sqrt{\left(\frac{e^2 N}{\epsilon_0 m_e} \right)} \quad (2.7)$$



The plasma frequency depends on the intrinsic properties of materials including the carrier concentrations N , the effective mass of electron in such materials m_e and the vacuum permittivity ϵ_0 . When the driving frequency of external electric field ω is equal to plasma frequency ω_p , the real part of permittivity will become zero. This is the critical frequency that all the electrons will oscillate in-phase throughout the materials. However, when $\omega < \omega_p$, the real part permittivity will be negative, the optical properties of materials behave as reflective as metal.

After obtaining the spectral permittivity of materials, the optical properties such as transmittance and reflectance can be simulated by the means called transfer matrix method.[52]

The transfer matrix by one-layer thin film is given:

$$M = \begin{pmatrix} \cos(k_o \tilde{n} d \cos \psi) & \frac{-i}{\tilde{n} \cos \psi} \sin(k_o \tilde{n} d \cos \psi) \\ -i \tilde{n} \cos \psi \sin(k_o \tilde{n} d \cos \psi) & \cos(k_o \tilde{n} d \cos \psi) \end{pmatrix} \quad (2.8)$$

Where k_o is the wave vector of incident light and ψ is the angle between the normal of film and propagation vector. It is taken $\psi = 0$ for normal incident wave. \tilde{n} and d are the complex refractive index and the thickness of the film.

The overall transfer matrix for n layers thin film is the product of transfer matrix of each layers:

$$M_{multilayer} = \prod_{j=1}^N M_j(n_j, d_j) \quad (2.9)$$

The transmission coefficient t can be calculated by the matrix element of transfer matrix

$$t = \frac{2}{(m_{11} + m_{12}n_s) + m_{21} + m_{22}n_s} \quad (2.10)$$

Where m_{11} , m_{12} , m_{21} and m_{22} are the matrix elements of overall transfer matrix M

The overall transmittance of the light across n layers thin films is given by

$$T = \frac{n_{substrate}}{n_{air}} |t|^2 \quad (2.11)$$



Figure 5-17(b) is the simulation in the transmittance of trilayer structure by effective approximation. The light was assumed to be normal incident and the glass refractive index was set to be constant at 1.5 throughout the whole spectral range. The detailed calculation is given from Equation (2.8) to (2.11) The calculation was performed by Microsoft excel.



3 Experimental method

3.1 Ceramics PLD target fabrication

The PLD ceramic target was fabricated by conventional solid-state reaction through mixing strontium carbonate (SrCO_3), barium carbonate (BaCO_3), niobium pentoxide (Nb_2O_5) and gadolinium (III) oxide (Gd_2O_3) with designated compositions. Since the ionic radius of Gd^{3+} ion is 107.8 pm which is similar to the Sr^{2+} ion 132 pm, the Gd_2O_3 dopant is likely to replace the Sr^{2+} ion in the reaction. [53] Therefore, the chemical formula of GSBN50 is $\text{Gd}_y\text{Sr}_{x-3y/2}\text{Ba}_{1-x}\text{Nb}_2\text{O}_6$

The completed chemical reaction is listed below.



The weighted powders were ball-milled for 8 hours in an ethanol medium. After finishing the ball-milling process, ethanol was removed from the mixture by heating at 100°C in an oven for overnight. The collected powder was calcinated two times at 1150°C for 10 hours with ramping rate 5°C/min to undergo the complete chemical reaction. The resultant product was grinded using mortar and pestle. After that, PVA was added into the grinded powders as the binder. The powder then was shaped in the 2-inch mold and pressed by an oil-compressor with 200MPa pressure to form a small pellet. The pallet was first hold at temperature 650°C for two hours to remove PVA binder completely, then sintered at 1300°C for 10 hours with same ramping rate.



Table 3-1 the mass of the powder for ceramic preparation.

Molar mass(g/mol)	197.34	147.63	265.81	362.50	/
	BaCO ₃ (g)	SrCO ₃ (g)	Nb ₂ O ₅ (g)	Gd ₂ O ₃ (g)	Gd _y Sr _{x-3y/2} Ba _{1-x} Nb ₂ O ₆ (g)
SBN50	5.005	3.744	13.483	0	20
1%-GSBN50	5.001	3.630	13.474	0.0918	20
2%-GSBN50	4.998	3.515	13.465	0.184	20
4%-GSBN50	4.991	3.286	13.448	0.367	20

3.2 Pulsed laser deposition (PLD)

The pulsed laser deposition is one of the types of physical vapor deposition method employing the high energy focused laser beam is incident on ceramic materials to produce physical vapor deposited on a substrate.

Before the thin film deposition process, the substrates were first cleaned in acetone and then ethanol in an ultrasound bath for 10 minutes respectively and dried by a stream of nitrogen gas. Then the substrate was mounted on a heater using silver conductive paint. The silver conductive was painted on the bottom of the substrate as a coupling media to improve the thermal conductivity, ensuring that the substrate temperature, measured by a thermocouple, was the same as the heating element.

For thin film deposition, the PLD system (as shown in Figure 3-1) consisted of a simple vacuum chamber with rotary pump and turbo molecular pump which were used to evacuated to at least 10^{-4} Pa high vacuum base pressure measured by an ionization gauge. The heating block made by a tungsten filament was controlled by a PID controlled voltage source to attain the required temperature. After the vacuum pressure and temperature were stabilized, a Lambda-Physik KrF Excimer laser with 248 nm wavelength was employed for deposition. The laser beam was first focused by a focal lens, then incident on the target through a quartz window. The target was pre-ablated in 10 Hz repetition rate for two minutes to smooth the surface and remove impurities. In the deposition process, target was also rotated to avoid local damage.

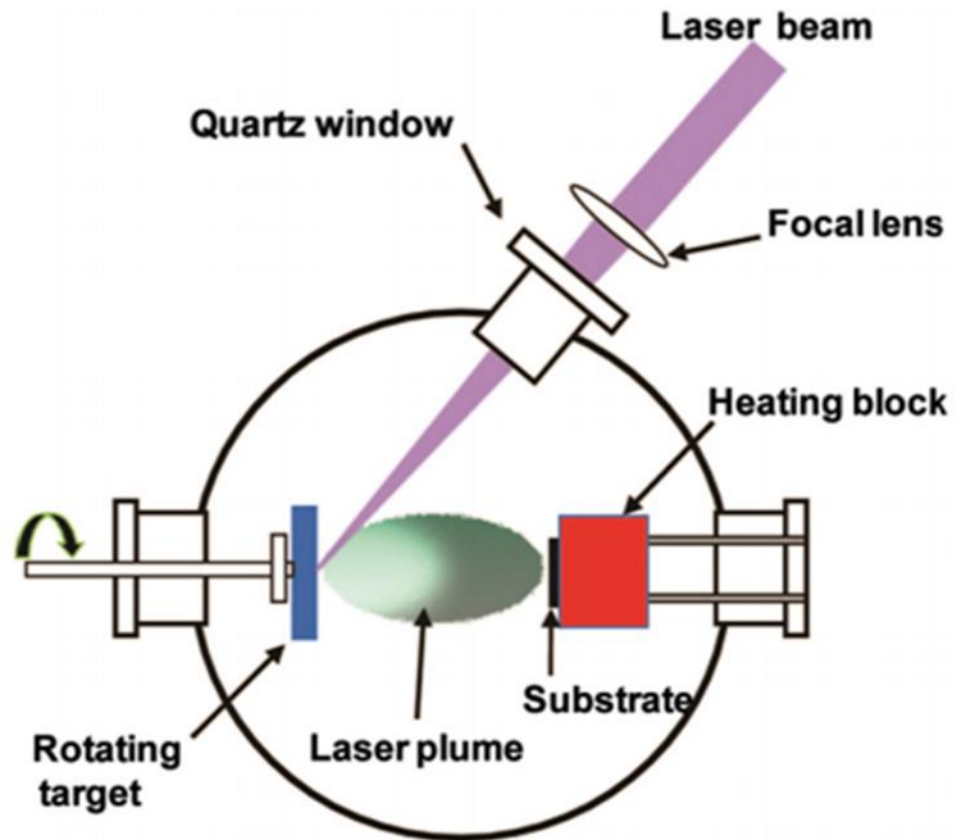


Figure 3-1 Schematic illustration of the pulsed laser deposition (PLD) setup[54]

3.3 Magnetron sputtering

Another type of physical vapor deposition method used in our experiments was magnetron sputtering (Denton sputtering system with Direct Current (DC) and Radio Frequency (RF) (13.56MHz) power supplies.) The ITO and Au thin films were deposited on Corning glass substrates (Corning Eagle XG AMLCD glass) and SiO₂/Si substrates of dimension 10 mm × 10 mm and thickness 0.7 mm by a DC and RF magnetron sputtering respectively. The magnetron sputtering system consisted the vacuum chamber with rotary pump and turbo molecular pump similar to PLD system to evacuate the chamber to 10⁻⁴ mtorr before begin deposition. In the deposition process, Argon gas was introduced into chamber to maintain chamber pressure to 1 mtorr for plasma generation. A negative voltage was applied to the sputtering gun to generate the electric field. Under the electric field, the Ar gas was being



ionized and attracted by the cathode bombarding on the target and sputtering out the target materials from the surface. The sputtered material travelled throughout the chamber and deposited on the substrate. The magnetron was used to generate magnetic field to move the charged ions in helical path increasing the probability of the ionized gas sputtering the target.

The substrates were first cleaned in acetone and ethanol in an ultrasound bath for 10 minutes respectively and dried by a stream of nitrogen gas.

After loading the substrates in the chamber, it was evacuated to a base pressure of 2×10^{-6} torr. A flow of 30 sccm argon gas was then kept in the deposition process. The substrates were heated to 100°C during the deposition process, as ITO films deposited at moderate temperatures showed lower resistivity compared with those deposited at room temperature of 100 °C, thus bringing better electrical performance for the ITO thin films.[55] Also, the temperature was not high enough for the Au layer to cluster, which ensured the deposited ultrathin gold layer is uniform and continuous.[56] The DC power of 80 W was applied to indium-doped tin oxide (ITO, In₂O₃/SnO₂ 90/10 wt%, Kurt J. Lesker Co.) target and RF power of 80 W was applied to the Au target (purity:99.99%) during deposition. All the three layers were deposited without breaking the vacuum to avoid interface contamination. By controlling the deposition time, the position of the insertion gold layer was varied in between the bottom ITO and top ITO layers. The substrates were rotated during the deposition process to obtain better thickness uniformity of the layers.



3.4 Structural characterization method

3.4.1 X-ray diffractometry (XRD)

The structural properties of the thin films and ceramics were characterized by X-ray diffraction method using Rigaku x-ray diffractometer operated at a CuK_α source with wavelength 0.154nm. X-ray diffraction (XRD) is one of the most widely used non-destructive material characterization methods.

The basic X-ray diffraction theory is based on Bragg's Law. When the electromagnetic wave incident on an atom, the electron clouds of the atom will be driven by incident wave. The movement of the electrons will re-radiate the electromagnetic wave with the same frequency of the incident wave. This effect is called elastic scattering. When the parallel X-ray incident on a lattice plane with regular array of atoms. The lattice plane will become a three-dimensional diffraction grating, the diffracted wave will produce constructive and destructive interference pattern at certain angular positions.

For the strongest intensities of constructive interference, the Bragg's law of Bragg's conditions must be fulfilled, i.e.

$$2d_{hkl} \sin \theta = n\lambda \quad (3.12)$$

Where d_{hkl} is the interplanar spacing between two successive crystallographic planes of the crystalline lattice, θ is the diffracted angle and λ is incident wavelength with the positive integer n indicate the order of diffraction peaks.

The interplanar spacing of different lattice plane can be calculated by the lattice constant of unit cell and Miller indices of corresponding lattice plane. The interplanar distance of different structures can be calculated as follow:



Table 3-2 The interplanar spacing of different lattice system

Cubic	$\frac{1}{d_{hkl}^2} = \frac{(h^2 + k^2 + l^2)}{a^2}$
Tetragonal	$\frac{1}{d_{hkl}^2} = \frac{(h^2 + k^2)}{a^2} + \frac{l^2}{c^2}$
Orthorhombic	$\frac{1}{d_{hkl}^2} = \frac{h^2}{a^2} + \frac{k^2}{b^2} + \frac{l^2}{c^2}$
Hexagonal	$\frac{1}{d_{hkl}^2} = \frac{4h^2 + hk + k^2}{3a^2} + \frac{l^2}{c^2}$

Where h, k and l are the Miller indices of the lattice plane and a, b, c are the lattice constant of the cell.

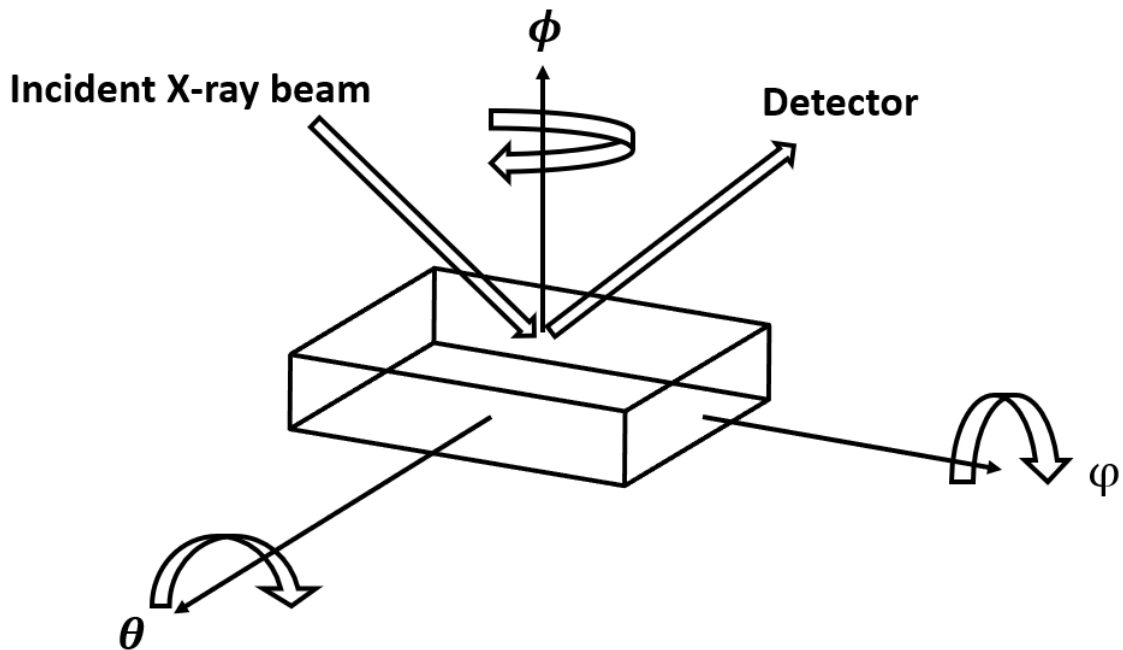


Figure 3-2 Schematic diagram of the XRD system with different axis of rotations.

The θ - 2θ scan is the most common used scan of the X-ray diffractometry, which can be used to analyze the phase structure, grain size and stress in either powders or thin film materials. In the θ - 2θ scan, the X-ray source is fixed at certain angle. When the sample is rotated an angle θ with respect to the X-ray beam propagation direction, the detector will follow the sample rotation and rotate two times of the angle θ to detect the reflected X-ray beam by the lattice



plane of the sample. For certain angle of the lattice which fulfill the Bragg's diffraction conditions, the strongest signal intensities will be detected due to constructive interference. The resultant XRD spectra will be plotted as the diffracted intensities against the 2θ angle, each material will produce its unique XRD profile, hence by comparing the XRD pattern with XRD profile of the standard material, the phase of the materials can be confirmed.

The omega scan, known as rocking curve measurement, is usually used to analyze the crystallinities of thin film materials. The ω angle is defined as the angle between the wave vector or propagation direction of the X-ray source and the sample. The rocking curve measurement is first fixed the θ - 2θ angle according to certain diffraction peak of the film observed in the θ - 2θ scan, then rocked few degrees relative to the diffraction peak. The obtained result can indicate the crystallinities of the target film orientation by analyzing the Full Width Half Maximum (FWHM) of the peak, the better crystallinities will result in a smaller FWHM value i.e. the more grains in the same orientation, the higher peak intensities will result a narrower peak width.

For the phi (ϕ) scan, the in-plane alignment relationship of substrate and films can be determined. The ϕ angle is defined as the angle of rotation along the axis perpendicular to the lattice plane. To perform 360° ϕ scan, the sample is first tilted to certain χ -angle which the lattice vector of the plane is parallel to the normal axis. Here the X-ray source, the detector and the lattice vector are lied on the same plane. For instance, to measure the (202) lattice plane on MgO (001) substrate, the χ angle is set to 45° i.e. the angle between (202) and (001) lattice plane. Also, the angle between (001) and (111) plane will be 54.7° . The angle between lattice planes are simply described by the dot product of the reciprocal lattice vector with the Miller indices.

$$\cos \theta = \frac{h_1 h_2 + k_1 k_2 + l_1 l_2}{\sqrt{h_1^2 + k_1^2 + l_1^2} \sqrt{h_2^2 + k_2^2 + l_2^2}} \quad (3.13)$$

Where h, k, l are the Miller indices of the corresponding lattice plane.

3.4.2 X-ray Reflectometry (XRR)



X-ray reflectometry is another non-destructive method providing the information in nanometer scale usually used in analyzing thin film materials, by measuring the reflectivity of the incident X-ray on thin films or substrates, the layer thickness, the material density and the surface roughness can be determined.

3.4.3 Atomic Force Microscopy (AFM)

The surface roughness of thin film was measured by atomic force microscope (Burker Nanoscope 8). The atomic force microscope consists three parts: The cantilever with a nano-sized needle probe, the laser light source and position sensitive photodetector. When the needle probe is approached to the sample surface, the Van der Waal's force between the probe and the rough surface becomes significant. Indeed, either the attractive or repulsive force can cause the deflection of the cantilever. This small deflection can be measured by optical lever method using laser to illuminate back side of the cantilever, and the laser will be reflected and detected by a photodetector. Once the probe is deflected by the atoms, the reflected light will be reflected to different position of the photodetector, therefore the deflection can be measured precisely. Then the surface topology can be obtained by scanning over the whole surfaces.

3.4.4 Scanning electron microscopy with energy dispersive X-ray spectroscopy (SEM-EDX)

The surface morphology and composition were characterized by TESCAN VEGA3 scanning electron microscope with Energy-dispersive X-ray spectroscopy (EDXs).

In the experiment, the electron emitted by thermionic, Schottky and field-emission were accelerated by the high voltage and focused by series of electromagnetic lens system on the sample surface. The incident electron beam, also called the primary electron, then generated electron signal by the secondary, backscattered and Auger electron through several interaction mechanisms and electromagnetic signals by emitting braking radiation between the electron and specimens. Those signals were then be collected by the detector inside the specimen chamber to form the image in the computer.[3-57]



3.4.5 Transmission electron microscope (TEM)

The thin film cross-section thickness and crystal structure were observed by the transmission electron microscope (Jeol JEM-2100F) which is a type of electron microscopy with ultra-high resolutions to observe the structure down to atomic scale.

The electron beam incident on the specimen can either be transmitted or diffracted. The transmitted electron beam is magnified by the electromagnetic lenses. The electron beam can be observed by series method such as the bright field and dark field imaging to obtain an image of specimen or electron diffraction to confirm the crystallographic structure and crystallinity of sample.

In the experiment, the substrate with thin film was first cut into half using a diamond cutter. Then two species were glued by M-bond 610 epoxy with the film surfaces facing each other. The bonded sample was heated at 120 °C for 1 hour drying and hardening using epoxy. After that the sample thickness was thinned down to approximately 20 μ m on the cross-section direction using series of sandpaper and polishing paper. The thinned sample was then bonded on the copper supporting gird with 3 mm outer and 2 mm inner diameter and further thinning by Argon gas ion milling until the perforation was observed. There would be a thin area surrounding the hole and was electron transparent for TEM observation.[58]



3.5 Physical properties measurement method

3.5.1 Spectroscopic ellipsometry

In the ellipsometry measurements, the commonly used technique is the rotating-analyser ellipsometry configuration, the Xenon lamp light source will be first passed through a polarizer before incident on the sample. Then the reflected light from the sample will pass through a rotating analyser being rotated to a certain angle and collected by the detector.

The spectroscopic ellipsometry is the technique that characterizes the optical properties of thin film materials such as complex reflection coefficients. A polarized light incident on a thin films, the polarization state will be changed upon the reflection on the surfaces or interfaces, the change of polarization state will depend on the optical and structural properties of the materials. [59] The ellipsometric parameters ψ and Δ are extracted by the reflection coefficient ratio between the p-polarization and s-polarization of the reflected light, r_{12}^p and r_{12}^s respectively [60]

$$r_{12}^p = \frac{\tilde{N}_2 \cos \phi_1 - \tilde{N}_1 \cos \phi_2}{\tilde{N}_2 \cos \phi_1 + \tilde{N}_1 \cos \phi_2} \quad (3.14)$$

$$r_{12}^s = \frac{\tilde{N}_1 \cos \phi_1 - \tilde{N}_2 \cos \phi_2}{\tilde{N}_1 \cos \phi_1 + \tilde{N}_2 \cos \phi_2} \quad (3.15)$$

Where \tilde{N}_1 and \tilde{N}_2 are refractive index of two materials

The total reflection coefficient from two interfaces are given by:

$$R^p = \frac{r_{12}^p + r_{23}^p e^{-i2\beta}}{1 + r_{12}^p r_{23}^p e^{-i2\beta}} \quad (3.16)$$

$$R^s = \frac{r_{12}^s + r_{23}^s e^{-i2\beta}}{1 + r_{12}^s r_{23}^s e^{-i2\beta}} \quad (3.17)$$

And ρ , the refractivity ratio will be obtained by

$$\rho = \frac{R^p}{R^s} = \tan(\psi) e^{i\Delta} \quad (3.18)$$

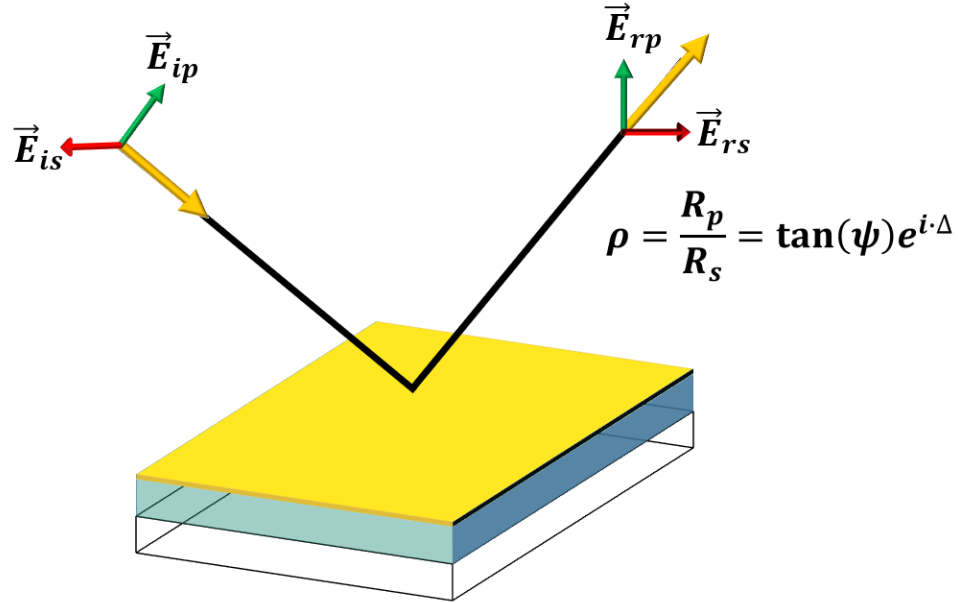


Figure 3-3 Schematic diagram of measurement of spectroscopic ellipsometer.

The standard procedure of ellipsometric measurement consists of four parts:

First, the sample is measured by either reflecting or transmitting ellipsometry to obtain the experimental (ψ, Δ) spectra. Then an optical model is needed based on the material properties and the structures, to generate a simulated spectrum. The simulated spectra are then fitted with the experimental data by varying the fitting parameters to retrieve the optical constants of the sample. The best fitting result are obtained by minimizing the error functions.

The goodness of fitting is estimated by the Mean Square Error (MSE) function given before [61, 62]

$$\text{MSE} = \sqrt{\frac{1}{2N - M} \left[\left[\sum_{i=1}^N \frac{\psi_i^{\text{Theo}} - \psi_i^{\text{exp}}}{\sigma_{\psi,i}^{\text{exp}}} \right]^2 + \left[\sum_{i=1}^N \frac{\Delta_i^{\text{Theo}} - \Delta_i^{\text{exp}}}{\sigma_{\Delta,i}^{\text{exp}}} \right]^2 \right]} \quad (3.19)$$

Noticed that the lowest MSE value does not mean the best description in the real situation. It will sometime lead to an unphysical result. Therefore, it is needed to add some physical constrains in the fitting process even though the final MSE result is not the lowest value.



3.5.2 Electrical and hall measurement

To characterize the intrinsic electrical properties of a bulk or thin film materials, the sheet resistance and the I-V characteristics were measured by four-point probe measurement, and the carrier concentrations and carrier mobility were measured by the Hall measurement.

3.5.2.1 Van der Pauw method

Generally speaking, there are two typical hall measurement methods commonly adopted, namely, the Hall bar configuration and the Van der Pauw configuration. The Van der Pauw configuration is usually used to measure the resistivity and hall coefficient of the samples with arbitrary shape proposed by L.J. Van der Pauw [63].

The Van der Pauw method is divided into two parts: the first part is the measurement of resistivity using four point probe configuration. As reported by L.J. Van der Pauw[63], the resistivity of the sample is written in Equation (3.20)

$$\rho = \frac{\pi d}{\ln(2)} \left(\frac{R_{12,43} + R_{14,23}}{2} \right) f \quad (3.20)$$

Where $R_{12,43} = \frac{V_{34}}{I_{12}}$, $R_{14,23} = \frac{V_{23}}{I_{14}}$, and the d is the film thickness and f is the geometric correction term which is the function of $R_{12,43}$ and $R_{14,23}$. The f value usually set as one for circular or square shaped sample.

The second part is the electrical measurement under constant magnetic field to measure the hall voltage V_H and obtain the Hall coefficient R_H .

$$R_H = \frac{V_H d}{IB} = \left[\frac{(R_{B+} - R_{B-})d}{2B} \right] \quad (3.21)$$

In this part, the $R_{B+}/B- = \frac{V_{42}}{I_{13}}$ is the lateral resistance under positive (into sample) and negative (out of sample) magnetic field respectively.

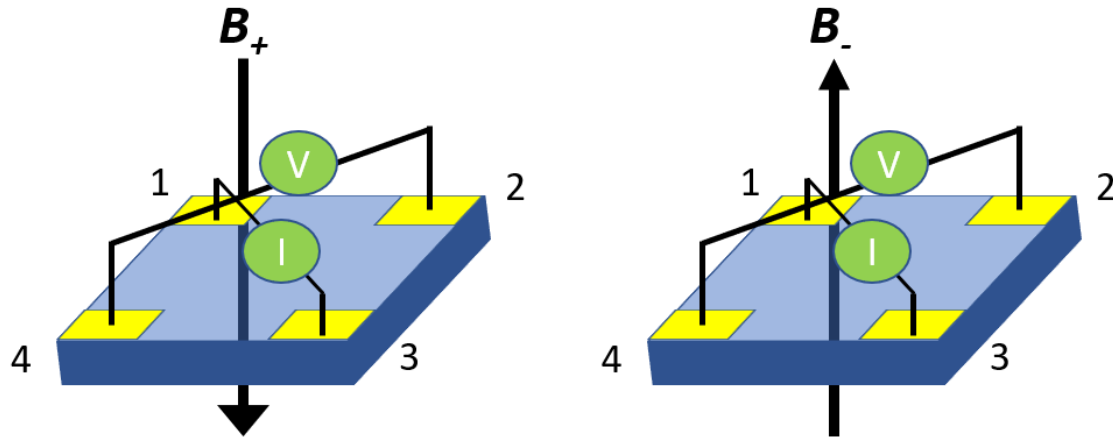


Figure 3-4 Schematic illustration of measurement of lateral resistance under magnetic field.

After obtaining the Hall coefficient, the carrier mobility and the carrier concentration can be converted as the following equations:

$$n = \frac{1}{eR_H} \quad (3.22)$$

$$\mu = \frac{R_H}{\rho} \quad (3.23)$$

Where $e = 1.6 \times 10^{-19}$ is the electron charge and the type of carriers in the film can be determined by the polarity of Hall voltage. If the Hall voltage is positive/negative, the carrier will be p-type/n-type inside the material respectively.

In this thesis, electrical properties (carrier concentration, Hall mobility and resistivity) were measured by a Keithley 6221 Current Source and a Keithley 2182A nanovoltmeter with four points probe measurement using Van der Pauw configuration, under an 0.5 T magnetic field. The advantage of using four-point measurement on bulk or thin film material is this configuration can eliminate the contact resistance and the measured value directly represents the resistivity of the materials.

In the measurement, four corners of the square sample were wire bonded to a printed circuit board connected to the Keithley 6221 Current Source and the Keithley 2182A nanovoltmeter, with were both connected to a 2700 Precision Data Acquisition System with a switch box to perform the program-controlled measurement. The magnetic field was produced by an

electromagnet with a voltage amplifier, the magnetic field strength was measured by a Lakeshore gaussmeter with a hall probe.

The schematic setup of four-point measurement is shown in left hand side of Figure 3-5 (Left) Schematic diagram of four-point measurement and (Right) the top view of the positions four points on the thin for measurement. Here, the measurement started with the two point I-V characteristics by applying a 1mA constant current to two points, and measuring the voltage response, then combining the I-V curve with different connection of two point I-V measurement to result the material electrical properties.

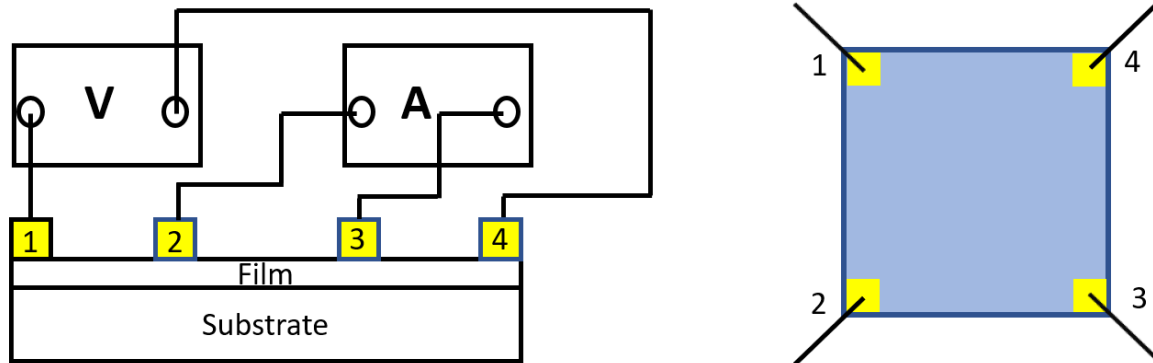


Figure 3-5 (Left) Schematic diagram of four-point measurement and (Right) the top view of the positions four points on the thin for measurement.



3.5.3 UV-Vis spectrometer

The transmittance spectra of thin films were measured by an UV-Vis spectrometer. The light source was generated by a halogen lamp. Then the light generated was passed through a monochromator and a beam splitter before incident on the sample (substrate deposited thin film) and the reference (bare substrate) separately. The light intensity after passing through the absorptive materials was recorded by the detector. The intensity decay of the sample relative to the reference according to Lambert-beer law was plotted as either transmission or absorption against wavelength to obtain the spectral response of the thin film materials.

3.5.4 Polarization-electric field (P-E) hysteresis loop measurement

The thin film ferroelectric hysteresis loop was measured by the RT-66 Precision Premier II Ferroelectric Tester (RADIANT Technologies). which is simply a Sawyer-Tower circuit [64]. In the measurement, an AC triangular shaped voltage was applied to the bottom electrode of the sample through a BNC cable. The sample was connected in series with a reference capacitor with a known capacitance C_{ref} much larger than that of the sample to ensure the samples capacitor would not be completely charged up. By measuring the voltage across the reference capacitor, the charge acumination can be estimated by,

$$Q = C_{ref}V_{ref} \quad (3.24)$$

$$P = \frac{Q}{A} \quad (3.25)$$

The polarization can be calculated by dividing the crossed-area of the electrodes. The signals from the sample and function generator were obtained by a digital oscilloscope and the Polarization-electric field curve was plotted. By changing the amplitude and frequency of the apply voltage to find the optimal polarization state of the sample was found.



4 Fabrication and characterization of epitaxial Gd-doped SBN thin films

4.1 GSBN ceramics target characterizations

The XRD θ - 2θ pattern of the Gd-doped SBN ceramic targets sintered at 1350 °C under an atmospheric pressure is shown in Figure 4-1. The bottom graph represents the powder diffraction data of SBN 50 from the ICDD database. The results showed that most of the peaks can be matched well with the database data. Thus, XRD spectra indicated that single TTB phase of SBN 50 ceramic was successfully sintered and no secondary phases were observed. The single phase TTB structures without any impurities implied that the Gd ions had diffused into the lattices forming solid solution with SBN crystals.

Using Bragg diffraction equation

$$2d_{hkl} \sin \theta = n\lambda \quad (4.26)$$

And the interplanar spacing for tetragonal lattice

$$\frac{1}{d_{hkl}^2} = \frac{h^2 + k^2}{a^2} + \frac{l^2}{c^2} \quad (4.27)$$

The lattice parameters of GSBN50 ceramics were calculated by using the (311) and (002) diffraction peaks. The results are shown in Table 4-1. As the Gd ions doping concentration increased, the X-ray diffraction peaks shifted to high angle, indicating that the Gd³⁺ dopant changed the lattice parameters of SBN unit cell. This can be explained by the ionic radius of the Strontium ions (Sr²⁺ ~ 0.112nm), barium ions (Ba²⁺ ~ 0.135nm) and gadolinium ions (Gd³⁺ ~ 0.111nm). [53] Since the ionic radius of Gd³⁺ ion is 111 pm which is similar to the Sr²⁺ ion, the Gd₂O₃ dopant is likely to replace the Sr²⁺ ion into the A sites in the reaction. Also, the substitution of Sr²⁺ ion by Gd³⁺ ions will gain excessive positive charges, which needs to be compensated by cationic vacancies to remain the charge neutrality. Therefore, point defect such as oxygen vacancies in the unit cell is resulted which will reduce the tetragonality factor (c/a). Even though the Gd dopant is different in off-valance configuration (+3 charges) compared with Sr and Ba ions (+2 charges), the 4% doping concentrations is approximately equivalent to a molar substitution and far below the probable limit of rare earth ion solubility in the SBN



crystal. The deterioration effect on the pyroelectric and phase transition properties can be ignored. [65]

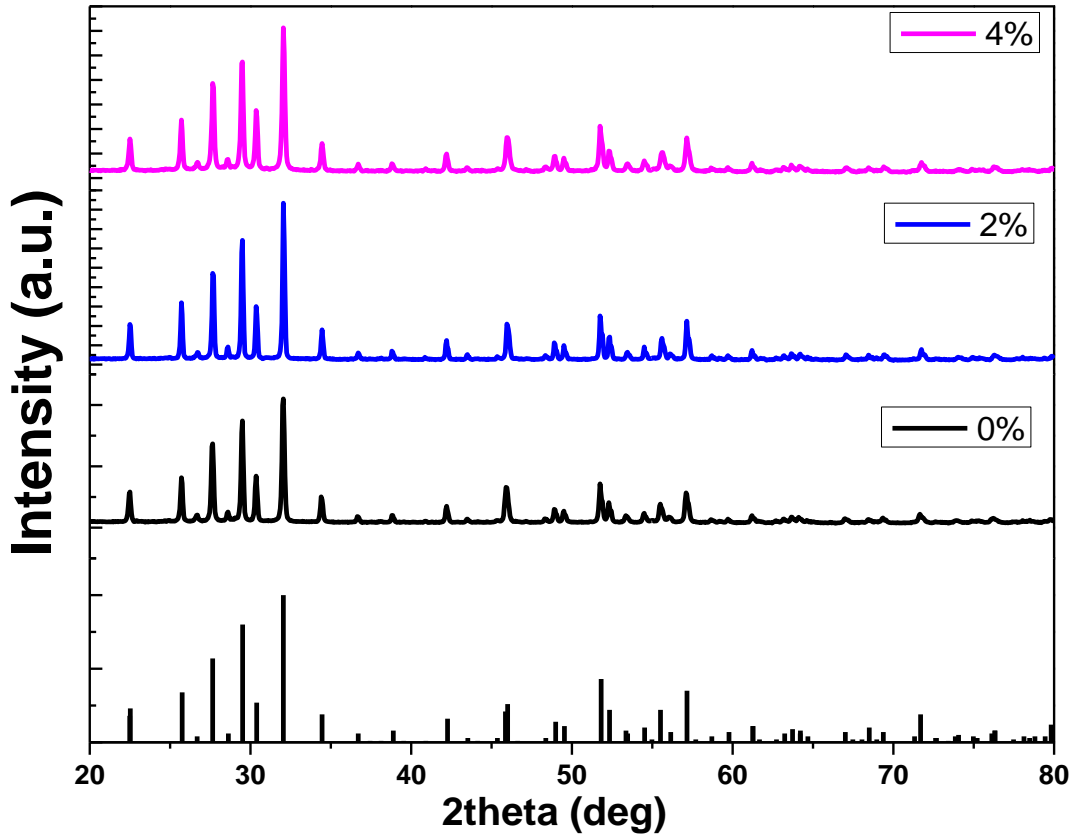


Figure 4-1 XRD spectra of standard SBN 50 from ICDD database, pure SBN50 and SBN50 doped with 2% and 4% Gadolinium concentrations.

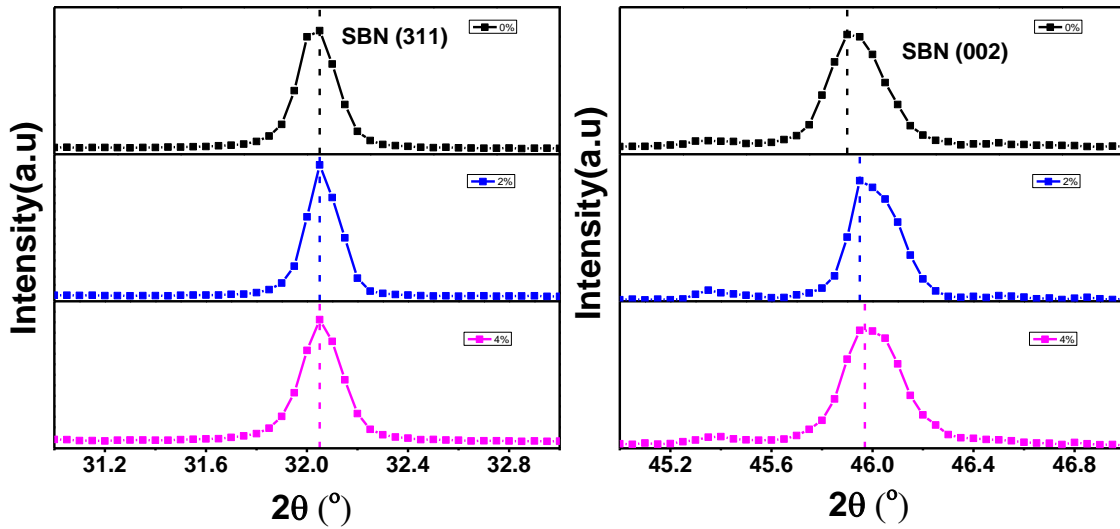


Figure 4-2 XRD patterns of GSBN50 ($x=0-0.04$) bulk ceramics 2theta angle of (a) (311) plane and (b) (002) plane

Table 4-1 The lattice parameter of GSBN ceramics with different Gd^{3+} doping concentration

Sample	a (nm)	c (nm)	tetragonality factor (c/a)
SBN	1.2459	0.3954	0.3174
GSBN2	1.2472	0.3945	0.3163
GSBN4	1.2477	0.3944	0.3161

The surface morphology and the composition were analyzed by scanning electron microscopy with energy Dispersive X-ray spectroscopy (SEM-EDX). For the 4%-Gd-SBN50, the nominal composition is $(Sr_{0.44}, Gd_{0.04}) Ba_{0.5} Nb_2 O_6$, the EDx measurement showed a slightly deviation to the nominal value. However, the compositions of the target were still within the relaxor ferroelectric composition ($0.25 \leq x \leq 0.75$). It is believed that the ferroelectric properties can



be preserved. Also, the Gd ions signal is resulted, which proved that the dopants were successfully doped into the SBN ceramics.

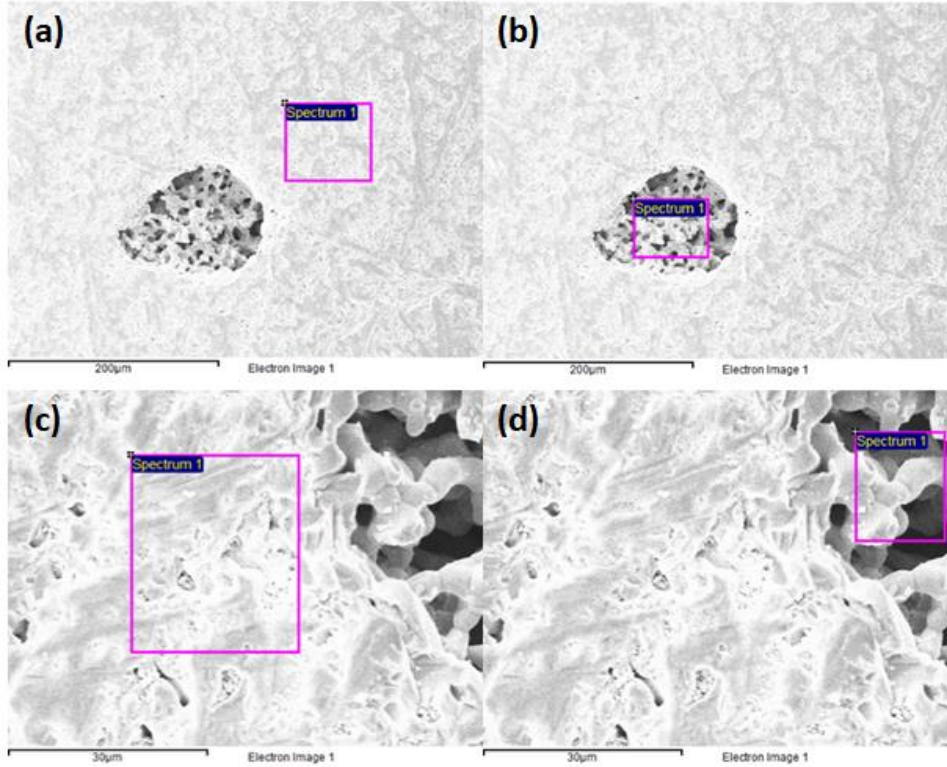


Figure 4-3(a)-(d) SEM image of 4% Gd doped SBN50 target

Table 4-2 The composition variation of the 4% Gd doped SBN targets at different position

	Position (a)	Position (b)	Position (c)	Position (d)
Sr composition	0.37716	0.28736	0.356506	0.316096
Ba composition	0.434632	0.382548	0.44451	0.360098
Gd composition	0.028736	0.004932445	0.029634	0.069146
Nb composition	1.789714	1.62987	1.826532	1.633462
O composition	6.34886	6.543726	6.32192	6.6003
Composition of target	(Sr _{0.38} , Gd _{0.03}) Ba _{0.43} Nb _{1.79} O _{6.34}	(Sr _{0.29} , Gd _{0.004}) Ba _{0.38} Nb _{1.63} O _{6.54}	(Sr _{0.36} , Gd _{0.03}) Ba _{0.44} Nb _{1.83} O _{6.3}	(Sr _{0.32} , Gd _{0.07}) Ba _{0.36} Nb _{1.63} O _{6.60}



4.2 Gd doped $\text{Sr}_{0.5}\text{Ba}_{0.5}\text{Nb}_2\text{O}_6$ epitaxial thin film on MgO substrate characterizations

Strontium barium niobite $\text{Sr}_x\text{Ba}_{1-x}\text{Nb}_2\text{O}_6$ single crystal, where $0.25 \leq x \leq 0.75$, has a high electro-optic coefficient[66] and outstanding photorefractive properties[67] that can be potentially applied in various optical applications. However, growing a large single crystal SBN is a difficult challenge, so the heteroepitaxial growth of SBN thin film is a relatively easier method to obtain crystalline SBN, since tetragonal tungsten bronze structure can be easily integrated onto cubic substrates, one of the most frequently used growth techniques is physical vapor deposition (PVD) such as pulsed laser deposition (PLD). Many reports had been demonstrated that SBN thin film was epitaxially grown on several cubic substrates for example, MgO[68] and SrTiO₃[69]. In this chapter, MgO (001) single crystal substrates were chosen for the growth of SBN thin films in order to find out the optimal deposition conditions including the deposition temperature and oxygen pressure using PLD method.

A KrF Excimer laser with 248 nm wavelength was employed for the growth of epitaxial films. The PLD system consisted of a simple vacuum chamber with rotary pump and turbo molecular pump which were used to evacuate the chamber to a 10^{-4} Pa high vacuum. The SBN film was grown at 700 °C substrate temperature with oxygen pressure of 26 Pa (200mTorr). Substrate to target distance was kept at 4 cm. Laser energy was 220 mJ with 5 Hz repetition rate. The sample was then annealed *in-situ* at the same growth temperature for 15 minutes to improve the crystallinity.

The crystal structure of SBN thin film was investigated by the X-ray diffraction spectra. Figure 4-4 shows the θ - 2θ scan of SBN50 and Gd doped SBN50 thin films deposited on MgO (100) substrates. Apart from the MgO (002) substrate peak ($2\theta=42.905^\circ$), there were only two peaks compared with the SBN polycrystalline ceramics, indicating that the polycrystalline ceramic became single crystal growth in the physical vapor deposition process. Since the material in plasma phase being deposited on high temperature substrate, the ions in plasma will situate in the position with the lowest electric repulsions. Therefore, the film deposited on substrate usually has its preferred orientations, a single phase domain is formed. The two peaks ($2\theta=22.47^\circ$ and $2\theta=45.85^\circ$) are corresponding to the SBN50 (001) and (002) lattice plane respectively. Both lattice planes were c-axis oriented which means that the c-axis was



perpendicular to the substrate interface. i.e. the SBN thin film was grown on MgO substrate with single c-axis orientation.

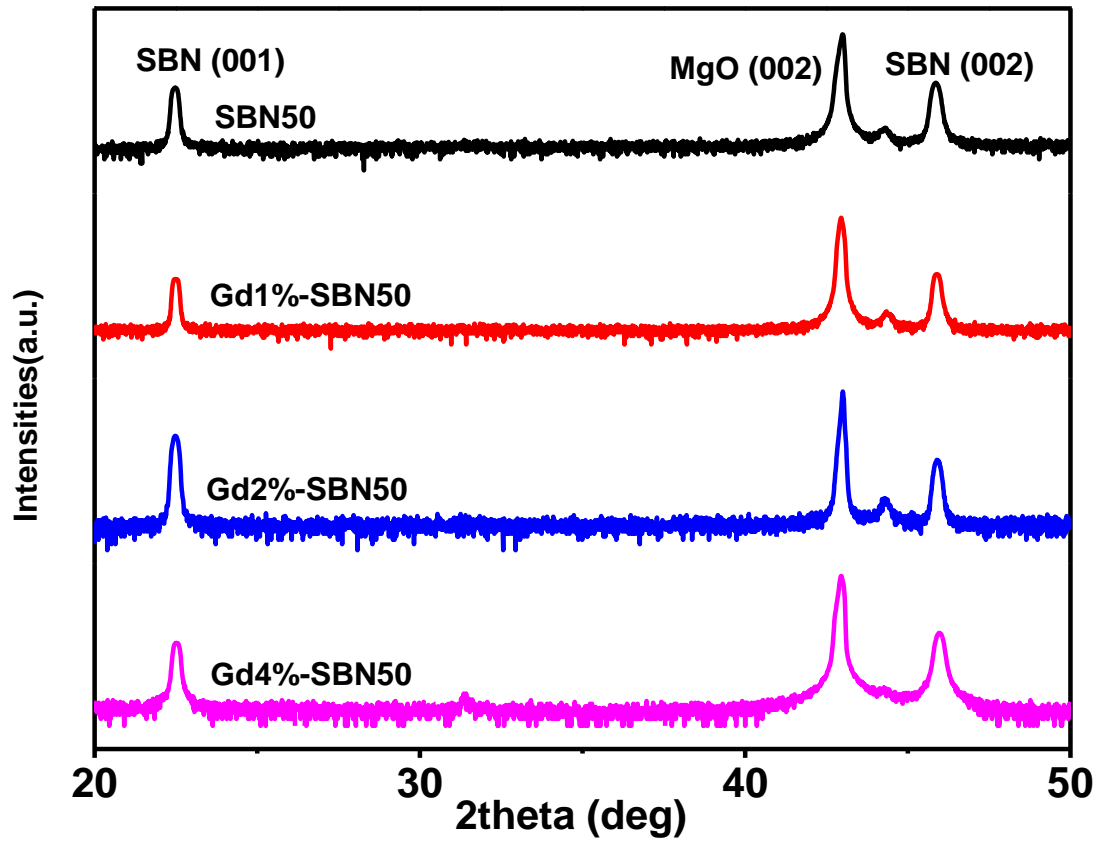


Figure 4-4 XRD spectra of pure SBN50 and Gd doped SBN50 thin film grown on MgO (100) substrate.

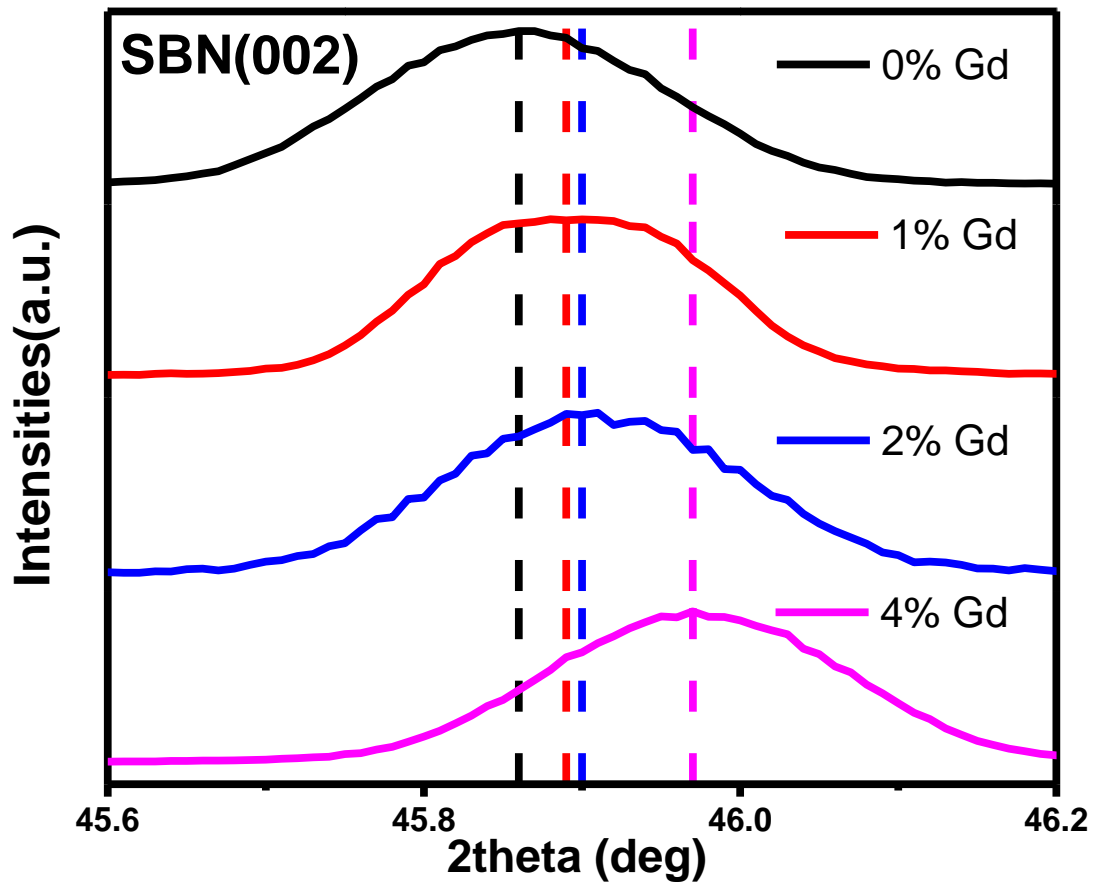


Figure 4-5 Shift of SBN (002) diffraction peak doped with various Gd dopant concentration.

Table 4-3 Calculated value C-lattice constant against the doping concentration

Sample	C-lattice constant(nm)
SBN50	0.3952
Gd-1% SBN50	0.3950
Gd-2% SBN50	0.3949
Gd-4% SBN50	0.3943

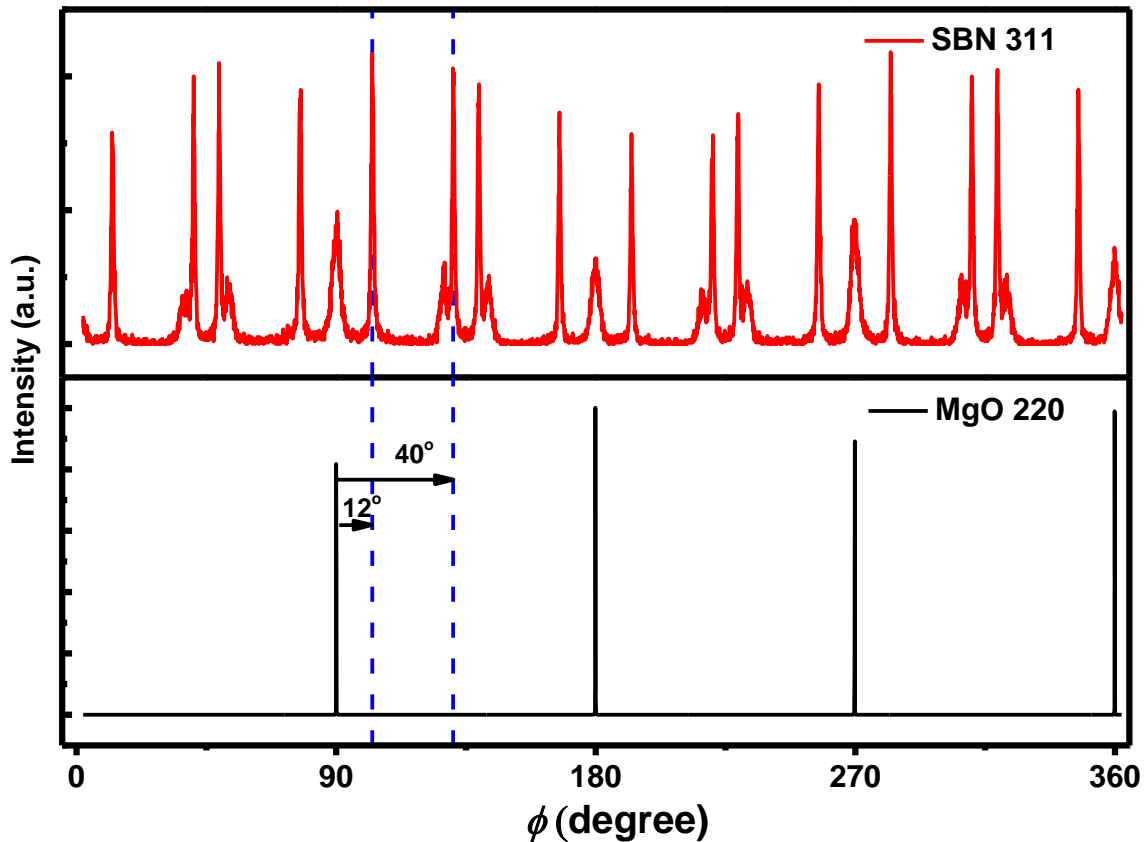


Figure 4-6 XRD 360° phi-scans of SBN film on MgO (0 0 1) substrate

Figure 4-6 shows the phi-scan of SBN thin film grown on MgO (1 0 0) substrate. By tilting the chi angle of the sample to 45° and maintaining the two-theta angle to 62.26°, the MgO (2 2 0) plane can be detected. Then rotating the sample by 360°, four diffraction peaks can be observed. The reason of four diffraction peak being observed is that the MgO (2 2 0) plane has four-fold symmetry. Then, the SBN (3 1 1) plane with two-theta angle 32.1° was scanned to investigate the epitaxial relationship with MgO. Apart from the 90°, there are two side peaks in between two consecutive MgO diffraction peak. The results indicate that the SBN films grown on MgO have two anti-phase domains. The SBN peak is rotated by 12° and 40° with respect to the MgO diffraction peak.

4.3 Thickness dependence of optical properties in 4% Gd-doped $\text{Sr}_{0.5}\text{Ba}_{0.5}\text{Nb}_2\text{O}_6$ epitaxial thin film on MgO



Figure 4-7 shows the transmittance spectra of different thickness of GSBN50 thin film with 4% Gd doping is measured by UV-vis spectrometer in the wavelength range 400 nm and 900 nm. The films show over 80 % transmittance in visible range.

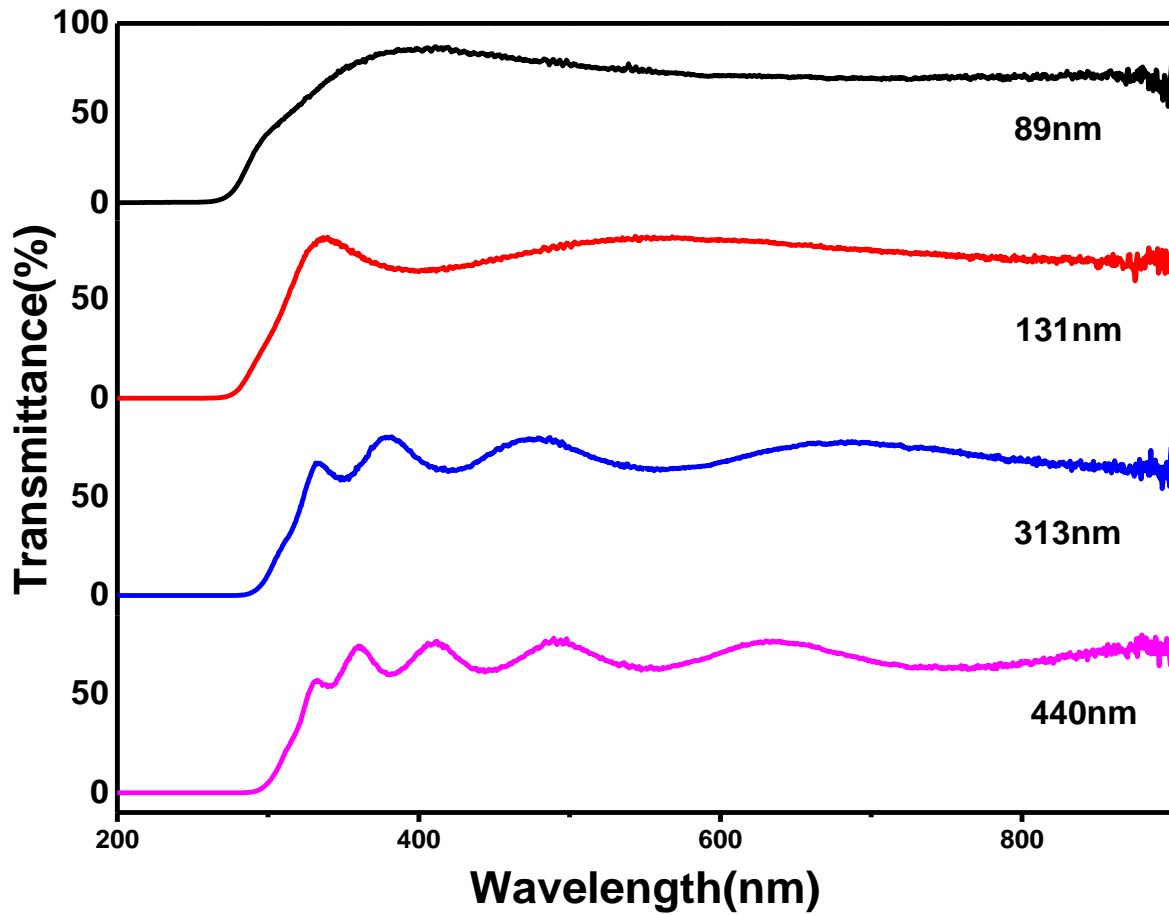


Figure 4-7 Observed transmittance spectra 4% Gd-doped SBN50 films with different thicknesses.

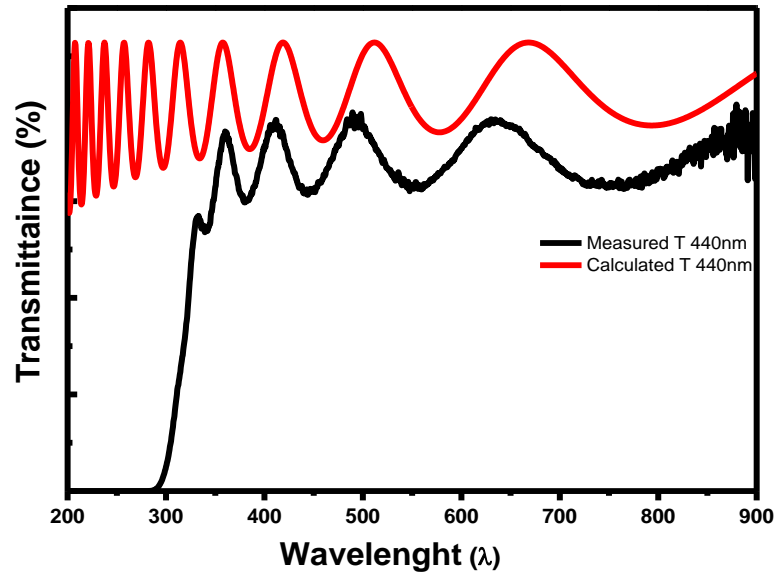


Figure 4-8 Calculated transmittance spectra 4% Gd-doped SBN50 films by transfer matrix method (TMM).

Figure 4-8 represented the calculated transmittance spectra of the 4%-GSBN50 thin film with different thickness using transfer matrix method. The modelling consisted a tri-layer system: Air ($n = 1$)/SBN ($n(\lambda)$)/MgO ($n = 1.73$). For the transparent region ($E \leq E_g$), the refractive index of SBN thin film for the calculations were calculated by using the conventional Sellmeier equation. [70]

$$n^2(\lambda) = A + \frac{B}{\lambda^2 - C} - D\lambda^2 \quad (4.28)$$

Where the A, B, C and D are the fitting parameters with was reported by Woike et al. [71]

Table 4-4 Sellmeier parameters for the SBN indices of refraction

Refractive index	A	B(μm^2)	C(μm^2)	D(μm^{-2})
n_o	4.9661	0.1342	0.0584	0.0275

The Fabry-Perot oscillation can be observed on both measured spectrum and calculated spectrum by TMM. Even though the transmittance peaks wavelength were slightly shifted, the calculated spectrum still showed the same order of the peaks with the highest transmittance. It is believed that the Sellmeier model fitted well with the refractive indices of GSBN thin film in long wavelength range.



However, when the wavelength decreases, the transmittance curve deviates significantly. The reason behind is related to the photon energies increase, electrons can be excited by the photons and causing interband transition. The transmittance will drop quickly when the wavelength of incident light decreases due to the absorption of photons by the thin film. For the interband region, the optical properties of SBN thin film can be modelled by the Tauc-Lorantz oscillator.[70]

The single Tauc-Lorantz dispersion equation is defined as following:

$$\varepsilon_2(E) = \begin{cases} \frac{AE_0C(E - E_g)^2}{(E^2 - E_0^2)^2 + C^2E^2} \frac{1}{E} & (E > E_g) \\ 0 & (E \leq E_g) \end{cases} \quad (4.29)$$

where the initial parameters of SBN thin films for calculation including the transition matrix element A, the peak transition energy E_0 , the broadening term C, the band gap energy E_g , and the high frequency dielectric constant ε_∞ were reported previously. [72] The $\varepsilon_2(E)$ is called the complex part of electric permittivity, which can be measured by the spectroscopic ellipsometry (HORIBA Jobin Yvon Ellipsometer) with the model fitting using equation (4.29) with the experiment data. The complex permittivity can finally be obtained.

$$\varepsilon_1(E) = \varepsilon_\infty + \frac{2}{\pi} P \int_{E_g}^{\infty} \frac{\omega \varepsilon_2(E)}{\omega^2 - E^2} d\omega \quad (4.30)$$

After obtaining the imaginary dielectric constant, the real part of dielectric constant can be calculated by Kramers-Kronig relation shown in Equation (4.30) and the analytical solution was reported by Jellison Jr. and Modine [73, 74] The calculation results are shown in Figure 4-9, which shown the refractive index tends to a constant value in long wavelength, this is coincident with the description with Sellmeier equation. The extinction coefficient increases rapidly when the approaching short wavelengths. This is related to the inter-band optical loss due to the absorption of incident photon.

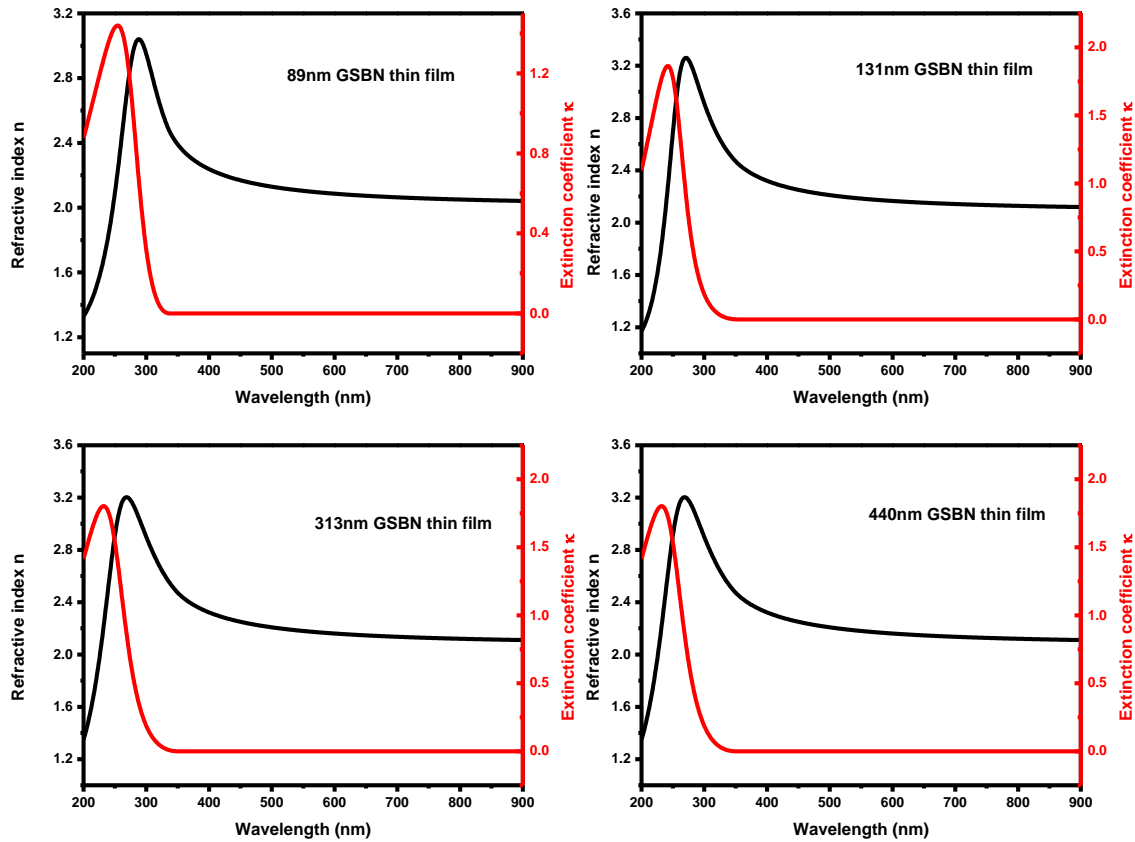


Figure 4-9 The dispersion of refractive index n and extinction coefficient k for 4%-GSBN50 thin film.

To estimate the validity of the retrieved parameter and the modelling, the Transfer matrix method was used to calculate the transmittance using the initial parameters retrieved from the spectroscopic ellipsometry.

Figure 4-10 shows the X-ray reflectivity measurement and the reflectivity curve fitting. The fitting result showed the film thickness of SBN thin film in 5 minutes deposition time was 84nm. The film thickness was then used as the fixed parameters for TMM calculation. The calculation results were shown in Figure 4-11. Among four samples with different thickness, the calculation can successfully model the transition range, the absorption edge and the number of the oscillation fringes. It is believed that the measured ellipsometric parameters are successfully describing the optical properties of the SBN thin films.

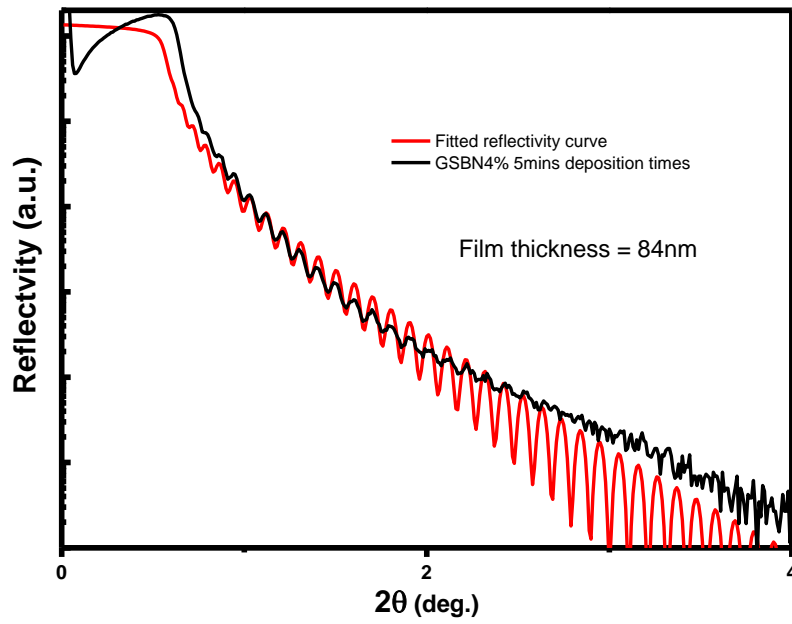
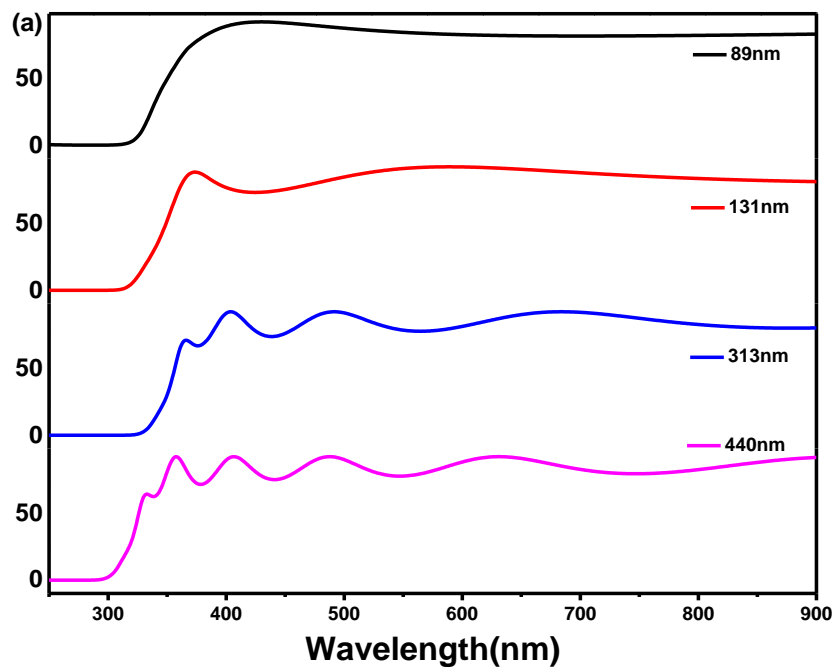


Figure 4-10 X-ray reflectivity curve and the fitted curve of 4%-GSBN50 thin film with 5 minutes deposition times.



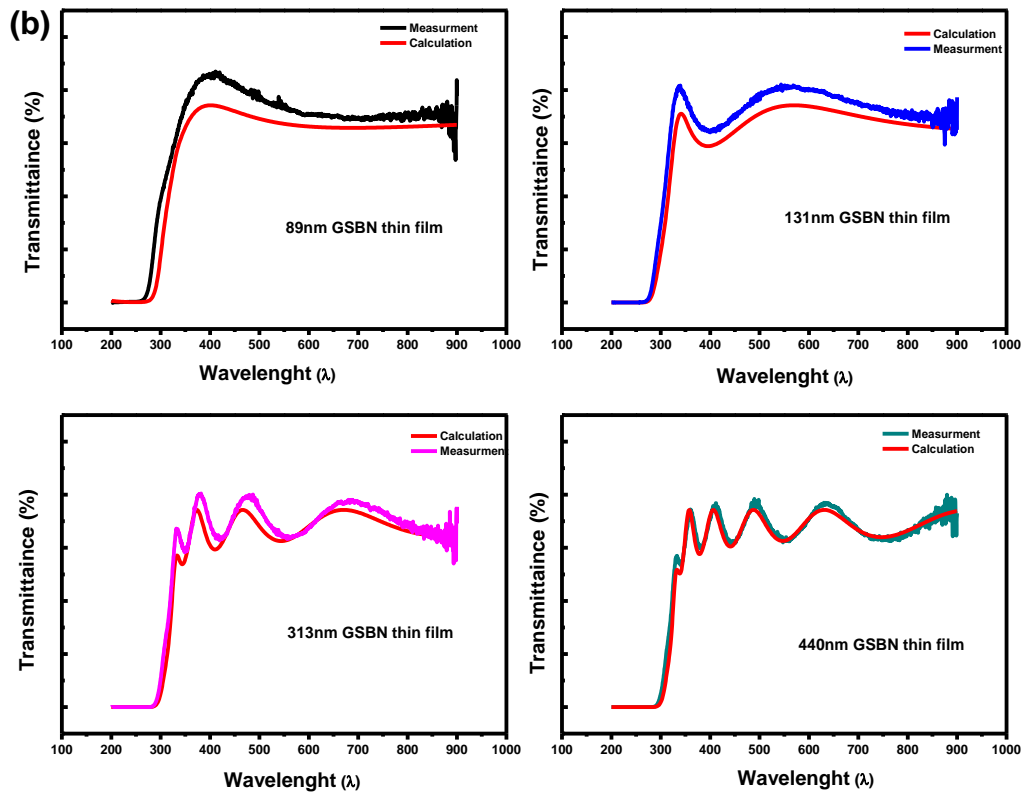


Figure 4-11 (a) The simulated transmittance spectra with different thickness of SBN sample. (b) The comparison of the simulated transmittance and the measured transmittance.

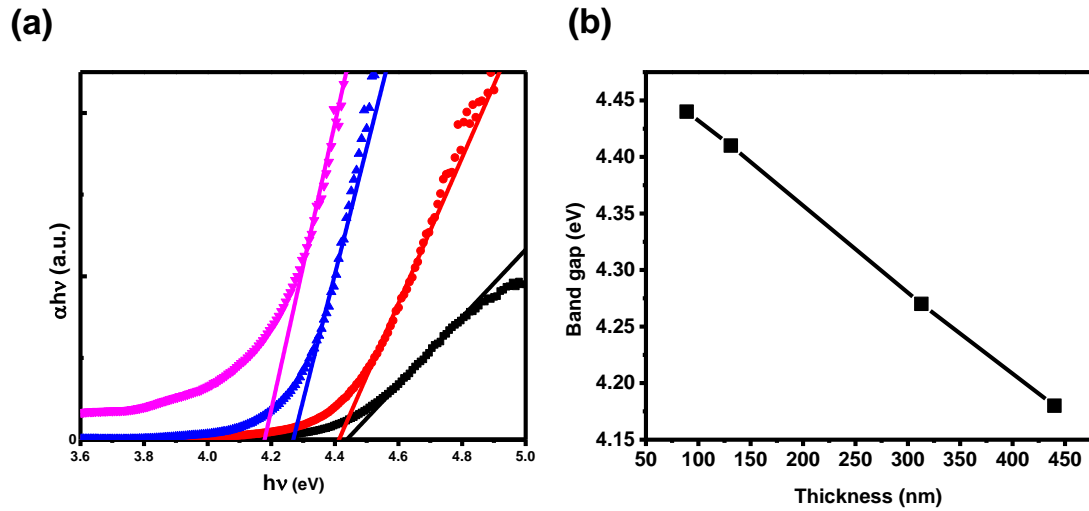


Figure 4-12 Tauc's plot of 4%-Gd doped SBN thin film on MgO substrate with various thickness.

The absorption coefficient can be obtained from the absorption edge of transmittance spectra using Tauc model.

$$\alpha = \frac{1}{d} \ln \frac{1}{T} \quad (4.31)$$

Where α , d and T are absorption coefficient, film thickness and transmittance.

$$(\alpha h\nu) = A(h\nu - E_g)^n \quad (4.32)$$

where α is the absorption coefficient, A is an energy independent constant, E_g is the optical band gap and n is a constant, which determines the type of optical transition, $n = 1/2, 2, 3/2$ or 2 for allowed direct, allowed indirect, forbidden direct and forbidden indirect electronic transitions, respectively. [75] By plotting $(\alpha h\nu)^2$ against $h\nu$ and fitting the linear range of the curve, the optical band gap can be estimated by the x-intercept by extrapolating the linear region in the graph.



The Tauc plot is shown in Figure 4-12(b) plotted the optical band gap against the film thicknesses of the SBN thin film. The optical band gap ranging from 4.18 eV to 4.44 eV, which is decreased with the film thickness increase. There are large variations in the optical edge of the films with an increase in thickness. It is also known that the thickness becomes important in the thin films. The thickness of the film causes a shift in the optical absorption edge and therefore a change in the band structure of the films. It is found that the optical absorption edge varies with increasing film thickness. This suggests that the defects in thin films occur during the formation of the films. Thus, unsaturated bonds can be produced because of an insufficient number of atoms. These bonds are responsible for the formation of some defects in the films and these defects produce localized states in the films. The thicker film increases the width of localized states in the optical band. [76] Provided that the measured bandgap is much larger than the bulk SBN single crystal, which the value reported is about 3.4 eV. One of the reasons causing such larger difference in the bandgap value can be accounted for the crystalline size on the film smaller than bulk ceramic. [77]

4.4 Ferroelectric properties of SBN thin film

The ferroelectricity is an important part to evaluate the applicability of SBN thin film. Since SBN is a typical non-central symmetric material. Most of the applications, apart from the electro-optic application, will be making a use of its ferroelectric properties. Also, previous studies had reported that the introducing the gadolinium dopant into SBN ceramic would improve the ferroelectric properties. [17, 18] It will be interest to verify whether the improvement by rare-earth dopant can be extend to the thin film devices.

The ferroelectric properties were investigated by multilayer stacking heterostructure as Figure 4-13(a) shown. The ferroelectric capacitor using vertical parallel plate structure, the 50 nm epitaxial Platinum thin as bottom electrode grown on (100) MgO substrate and 50 nm Gold thin a top electrode. Figure 4-13(b) reveals the 3D structure of the ferroelectric devices, the bottom and top electrodes are placed perpendicularly, and the ferroelectric thin film was inserted in between two crossed electrodes. The advantages of such structure are that reduce the possibility of electrical shorting of top and bottom electrodes in wire bonding process, also the effective Electric field only applied within the overlapping area of two electrode. The



concept is similar to the variable capacitor, the capacitance is dependent to the overlapping area of the plates. Therefore, the junction area can be controlled by the widths of the electrodes and the junction size will possibly be reduced.

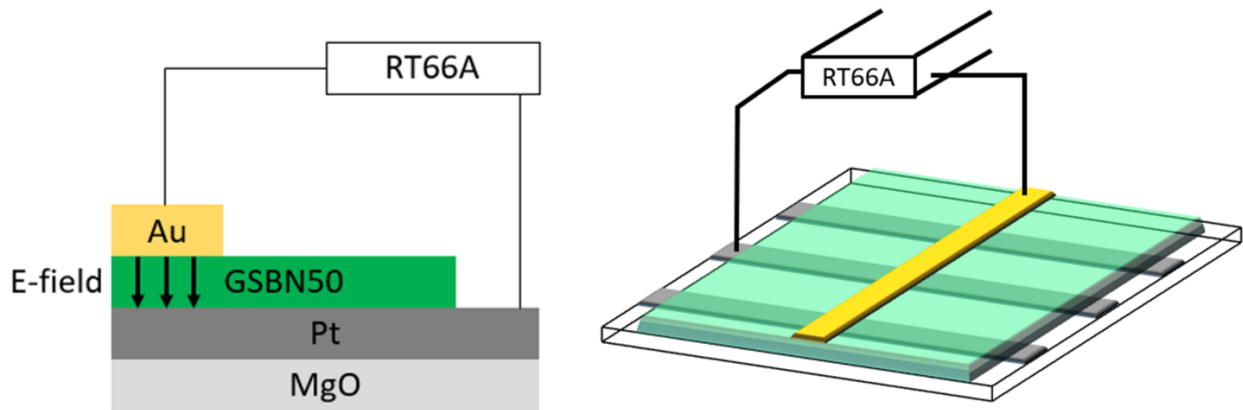


Figure 4-13 Schematic diagram of Au/ GSBN50 /Pt device (left) and the 3D structure of crossed bottom and top electrode structure. (right)

4.4.1 Structural characterization of SBN thin film ferroelectric capacitors

Figure 4-14 shows XRD θ - 2θ scan of the GSBN/Pt/MgO heterostructure. The Pt thin films are orientated in (002) lattice plane ($2\theta=46.12^\circ$) instead of (111) lattice plane ($2\theta=39.68^\circ$). The (111) phase of Pt can barely be observed. Since the Pt film was deposited at 700°C , which is favour the (001)-oriented crystallites instead of (111)-orientation due to relatively lower interfacial energy for (110) Pt/ (110) MgO at high temperature reported by McIntyre et al.[78] The volume fraction of (111) orientation was suppressed at high substrate temperature, Pt thin film will show the dominated (002) phase in deposition process. Also, due to the similarity of c-axis length of cubic Pt unit cell and TTB structure SBN ($a_{\text{Pt}}=0.392\text{nm}$ and $c_{\text{SBN}}\approx 0.39\text{nm}$), the 2θ angle separation between two film peaks were smaller than the FWHM of both peaks, cannot be resolved and only one peak observed at 46.12° . The advantage of selecting the (001)-oriented Pt film rather than (111) because such orientation can cubic to cubic epitaxy growth on (100) MgO substrates. The inset figures in Figure 4-14 were probing the rocking curve (ω -scan) of SBN (001) peak and Pt/SBN (002) film peaks. The red solid lines represent the Lorentzian fitting of the peaks to obtain the FWHM value. After the Lorentzian fitting, the



result shows the FWHM of SBN (001) and Pt/SBN (002) rocking curve are 1.64° and 0.43° respectively.

X-ray 360° Φ -scans of MgO (111), Pt (111) and SBN (221) are plotted in Figure 4-15(a). Two set of in plane orientation rotation of $\pm 45^\circ$ and $\pm 56^\circ$ from the substrate are observed. It is believed that the SBN thin film with (221) lattice was epitaxial growth on Pt (111) thin film which shows the similar relationship as the SBN thin film grown on LSCO (111) thin film due to the similarity in lattice constant of Pt and LSCO as reported.[79] Unlike the conventional epitaxial relationship between MgO (001) substrate and SBN thin film with the in-plane rotation by 18° and 31° [80, 81], the difference in the alignment angle may be caused by the lattice misorientation of the lattice or the lattice distortion due to elastic strain on the films.[82] The orientation of SBN had been reported with different values, it is believed that the orientations are strongly dependent to the processing conditions on the PLD process.

Figure 4-15(b) illustrates the epitaxial relationship and the in-plane orientation of MgO, Pt and SBN. The in-plane orientation of $\pm 56^\circ$ can be described as SBN (001)/Pt (320)//MgO (320). In this orientation the lattice mismatch is about 14%. Also, there is still a possibility of in-plane rotation in $\pm 45^\circ$ with the in-plane alignment SBN (001)/Pt (220)//MgO (220), the lattice mismatch of such alignment is about 10%.

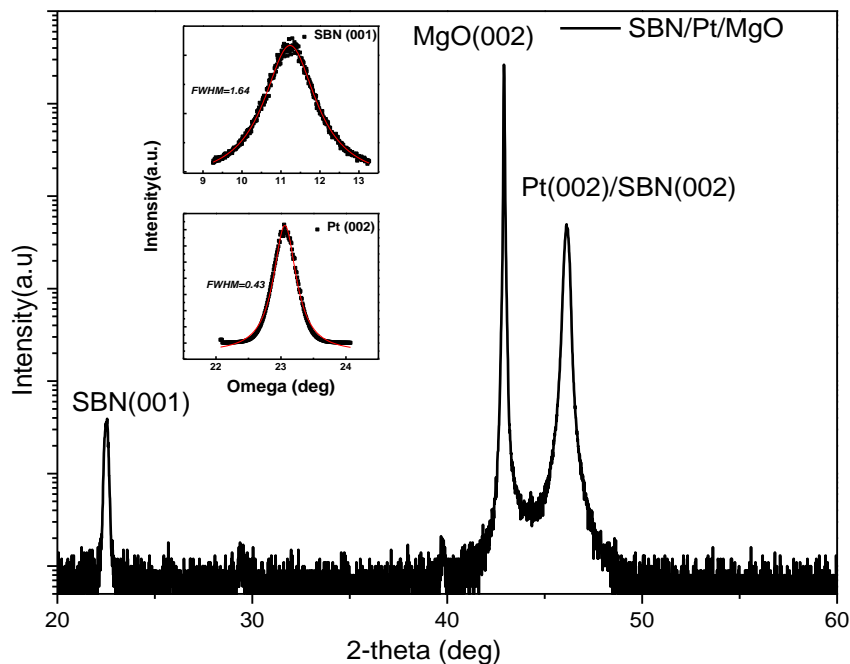




Figure 4-14 XRD θ - 2θ scan of GSBN50(500nm)/Pt(50nm)/MgO multilayer structure. Inset: ω -scan of SBN (001) and Pt (002)/SBN (002) diffraction peaks.

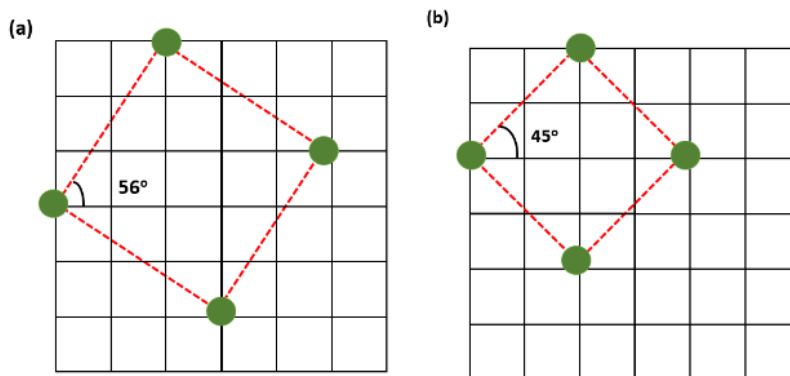
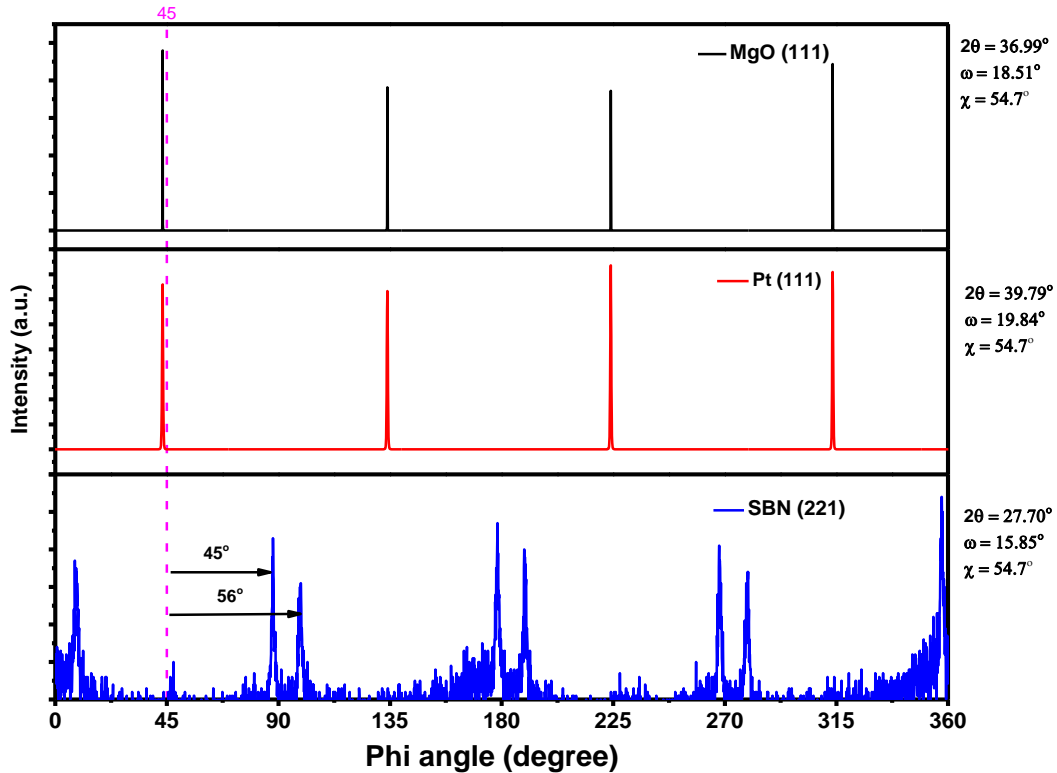


Figure 4-15 XRD phi scan showing epitaxial in-plane relationship of MgO(substrate)/Pt(film)/SBN (film). The substrate tilting at Chi-angle= 54.7° .

A scanning electron microscope was employed to characterize the cross-sections morphologies of the heterostructures. From the cross-section micrograph shown in Figure 4-16, two discernible layers are observed, the interface between the GSBN thin film and the Pt layer is smooth and sharp. From the Figure 4-16, the thickness of the GSBN and Pt layers are estimated to be 500nm and 50nm respectively.

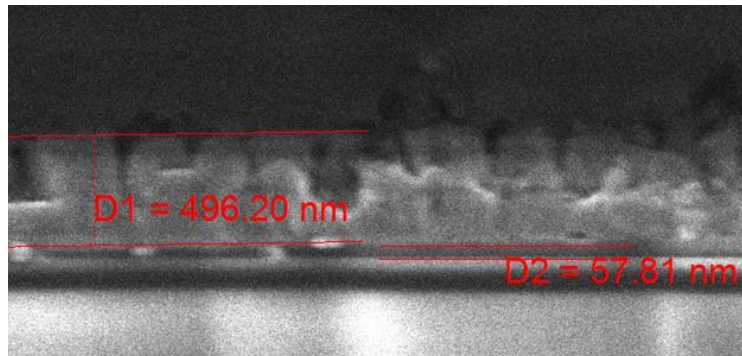


Figure 4-16 Cross-section Field Emission SEM image of SBN/Pt/MgO structure

4.4.2 Ferroelectric loop measurement

Figure 4-18 shows the ferroelectric hysteresis measurement of 500nm Gd4%-SBN50 thin film. All the hysteresis measurements were done under room temperature and atmospheric pressure. The voltage was applied to the top and bottom vertically, as shown as **Error! Reference source not found.**, the applied voltages were then converted to the lateral electric field by dividing the film thicknesses. The film thickness was confirmed by observing the cross-section using the Field emission SEM and the SEM micrograph was shown in Figure 4-16. The electric polarizations were calculated by the measured polarization dividing the junction area which is defined by the area crossed of top and bottom electrodes, which is determined by the width of top and bottom electrodes. The hysteresis measurements were done by Radiant Ferroelectric Test system (Radiant Technologies Inc. NM, USA). Since the virtual ground mode of the ferroelectric tester will cause the polarization relaxation due to the temporary memory. This mode will cause the discontinuity of the P-E loops. Therefore, all the hysteresis measurements were done by double loop and the first polarization loop was neglected. The voltage profile was shown in Figure 4-18(b). [83] When the applied electric field as large as $500\text{kV}/\text{cm}^2$, all the dipoles begin to align with the field and reach the saturation polarization gradually, resulted in the ramanent polarization values $+P_r = 1.36\ \mu\text{C}/\text{cm}^2$ and $-P_r = -5.73\ \mu\text{C}/\text{cm}^2$ and coercive field of $+E_c = 158.0\ \text{kV}$ and $-E_c = -30.8\ \text{kV}$ were obtained.

Noticed that the measured P-E loop was right shifted and being polarized asymmetrically because of the different material of top and bottom electrode. The similar phenomenon also reported by Masruroh and Masayuki Toda on investigation of PZT thin films with Au top



electrodes and Pt bottom electrodes.[84] The difference of work function of Pt bottom electrode and Au top electrode resulted in different polarization and coercive field.

On the other hand, the shape of the measured hysteresis loops cannot show the typical poling abilities as the single crystal and ceramic with a clear and sharp edges of saturation polarization. This is the typical problem of thin film ferroelectric materials. Since the substrate did not change the dimension under electric field, it would limit the switching properties of ferroelectric thin film and cause the strain in the film and substrate interface when the thin film was being switched. Thus, reducing the polarizing abilities of ferroelectric thin film. To address this problem, the thin film system must contain a large number of highly orientated domains, which means the film should be grown epitaxially on the desired orientations. [85]

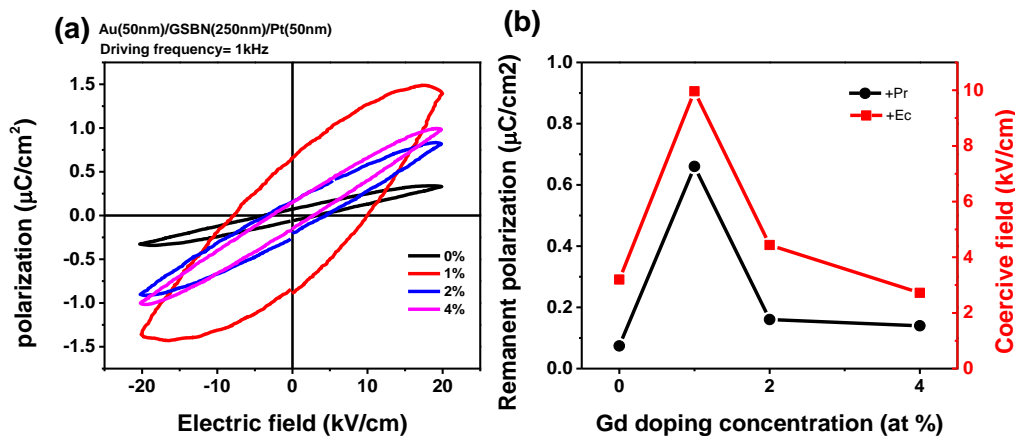


Figure 4-17 P-E hysteresis loops of undoped SBN and doped with Gd film measured at 1kHz with applied an electric field, $E = 20\text{kV}/\text{cm}$

Table 4-5 The coercive field (E_c) and remnant polarization (P_r) as a function of the Gd-doping concentration



Sample	Coercive field (kV/cm)	Remnant polarization($\mu\text{C}/\text{cm}^2$)
SBN50	3.25	0.07
Gd-1% SBN50	9.94	0.66
Gd-2% SBN50	4.46	0.16
Gd-4% SBN50	2.72	0.14

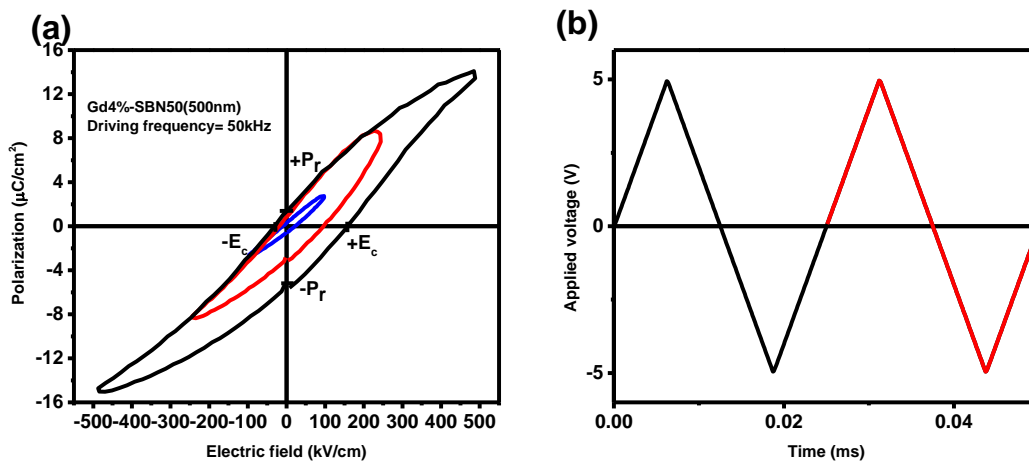


Figure 4-18 The P-E hysteresis loop of 4% Gd-doped SBN thin film with the varied electric field.

For the ferroelectric thin film devices, the leakage current is a serious problem to limit the performance of the devices. For example, the 100nm ferroelectric thin film can prudence 10^{-5} Acm^{-2} leakage current upon applied 1V potential.[86] There are many possible mechanism of the origin of leakage current such as ion drift and carriers conduction[87] To reduce the leakage current, one of the method is to reduce the junction area. Figure 4-19 shows the optical micrograph of the ferroelectric junctions. The bottom electrodes were the vertical lines with



the width 10 μm patterned by photolithography. The top electrode is the horizontal line with the width 50 μm using shadow mask for deposition. In this geometry, the junction area is the crossed area of two electrodes, which is approximate 500 μm^2 , the 20 times smaller than the previous devices.

Figure 4-20 plotted the hysteresis loop 500 μm^2 SBN thin film ferroelectric junction with different Gd-doping concentrations. Compared with the previous device with the same film thickness (500nm), a smaller junction can be switched by a slower frequency to obtain a typical hysteresis loop. It is strongly related to the time dependent switching properties into applications, such as the pyroelectric properties (a time varying temperature).

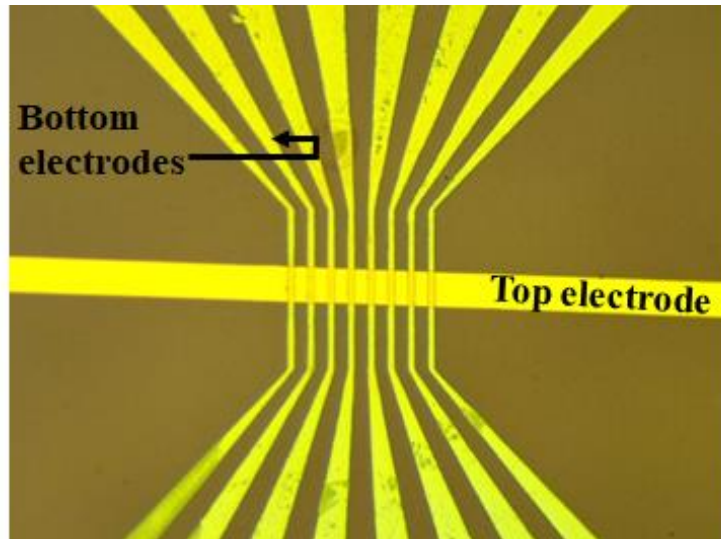


Figure 4-19 optical micrograph of the ferroelectric junctions.

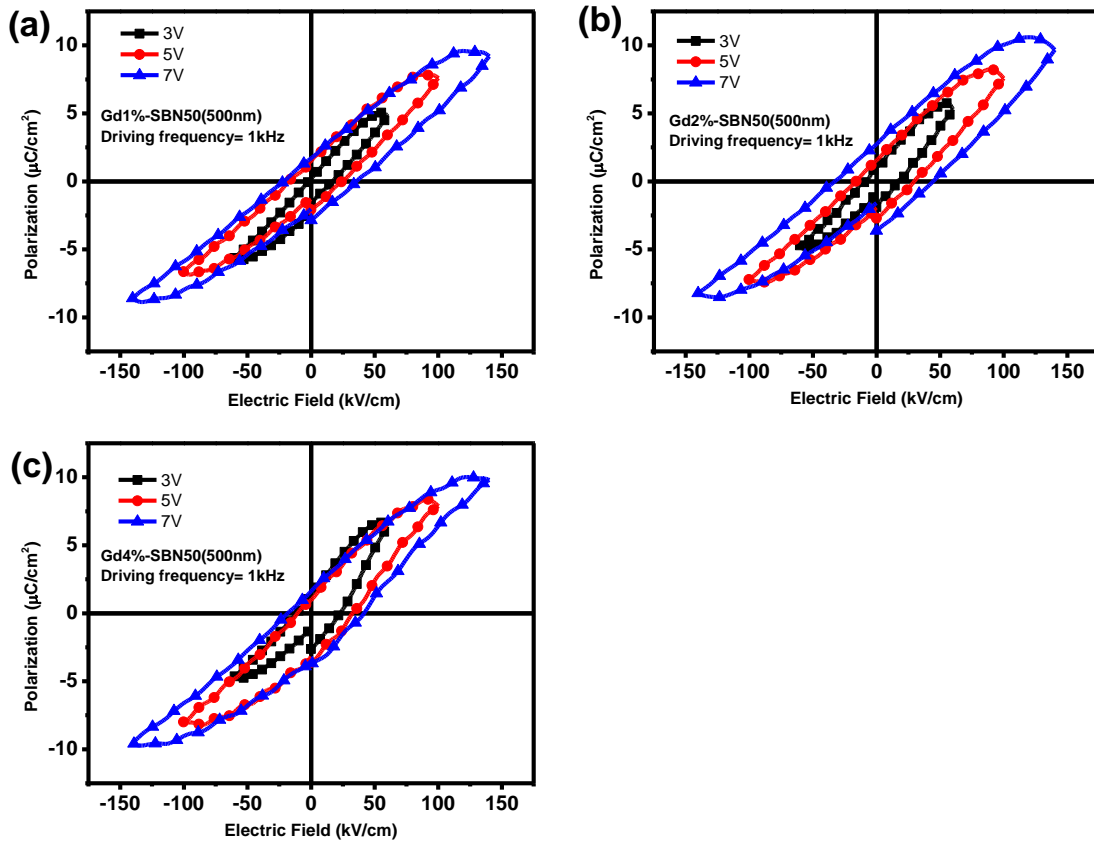


Figure 4-20 The P-E hysteresis loop of ferroelectric device with 500nm active layer (a) 1%Gd-doped SBN film, (b) 2%Gd-doped SBN film and (c) 4%Gd-doped SBN film.

Figure 4-21(a) shows the frequency dependent relative dielectric constant measured at room temperature to estimate the capacitive frequency response of the ferroelectric junctions. The result shows that the doped SBN thin films generally possess higher relative dielectric constants compared with the undoped one, indicating that introducing rare-earth element increases the relative permittivity of the ferroelectric parallel plate capacitor. However, larger ϵ_r will usually accompany with larger dielectric loss as shown in Figure 4-21(b). The relative permittivity was decreased slowly as the frequency increased, but as it approached to about 100 MHz, the relative permittivity suddenly increased rapidly. As the doping concentrations increased, this turning point seemed to be shifted to lower frequency. The dispersion spectrum is important parameter for considering the device performance under various driving frequencies.

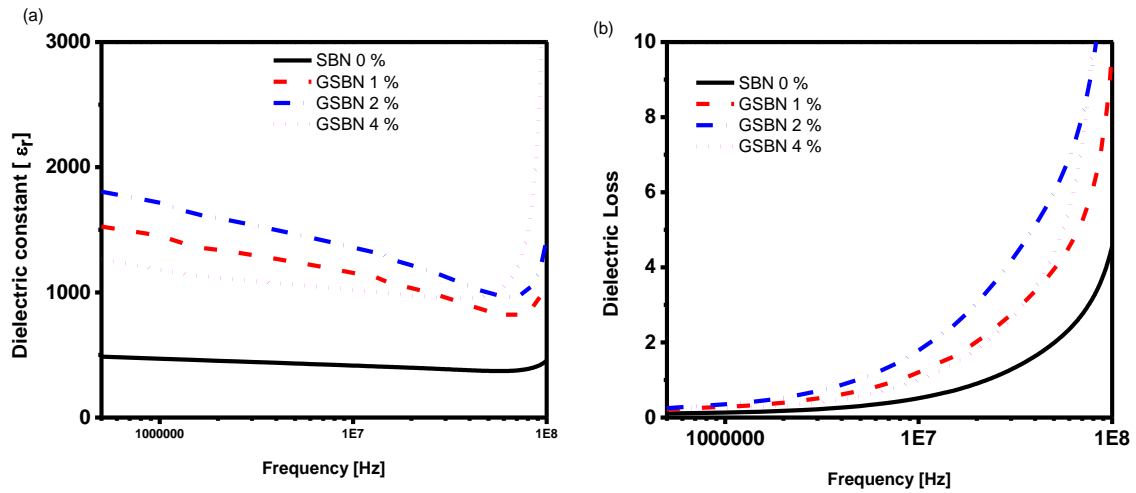


Figure 4-21 Frequency dependence of the relative dielectric constant ϵ_r and dielectric loss of the different Gd doped SBN thin film grown on Pt/MgO substrate.



5 Characterization of optical and electrical properties of ITO/Au/ITO multilayer thin film

5.1 Introduction

In this chapter, another type of transparent thin film will be discussed. As mentioned in chapter II, Tin doped Indium Oxide (ITO) is a widely used transparent and conductive oxide for different optoelectronic devices such as organic light emitting diode and solar cell, because of its high light transparency in the visible range and relatively high electrical conductivities. However, it has limitation in the plasmonic applications since the plasmonic resonance wavelength for ITO usually falls in the range of Mid-infrared to near-infrared range.

On the other hand, noble metals such as gold (Au) and silver (Ag) are usually being used in electronic and plasmonic applications due to their high free carrier densities, highly electric conductivities and negative real permittivity throughout the visible to near-infrared (NIR) range. Nevertheless, they also possess high optical losses due to the inter-band electron scattering, limiting them for fully application as optical devices in different wavelength.

One of the solutions will be combining the TCO and noble metal to form a vertical thin film multilayer structure. A typical multilayer structure is TCO/metal/TCO trilayer structure which has been widely studies in many fields such as electronics,[33] plasmonic devices[88] and hyperbolic metamaterials[89]. This multilayer structure possesses both advantages of TCO and noble metal, for example an ultra-thin noble metal film inserted in between two TCO can greatly influence the carrier density on TCO while the TCO layer can still preserve the high transparency in visible wavelength. [90]



5.2 Structural characterization of ITO/Au/ITO multilayer structures

Previous study by Fang et al. on ITO/Au/ITO trilayers with changing thickness of inserted gold layer had reported that the top and bottom ITO thin films will exhibit different degrees of crystallinity due to the insertion of gold thin layer. [91] To verify this hypothesis, series of samples with systematically changing the top and bottom ITO layer thickness were fabricated by magnetron sputtering. Since the ITO film thickness is easily controlled by programme-controlled sputtering process, the growth rate for ITO thin film was kept constant at approximately 1 Å/s by using fix deposition conditions. The gold insertion layer was kept approximately 3.0nm. The thicknesses of each trilayer samples were confirmed by X-ray reflectivity (XRR) measurement. Figure 5-1 shows the XRR spectra of samples with different ITO thicknesses. The measured XRR spectra were fitted in order to retrieve parameters including the film thickness and surface roughness. As expected, the results indicate that the ITO thickness is proportional to the deposition time with a constant ITO deposition rate.

Table 5-1 shows the relationship between the deposition time and thickness of the films. As expected, when the deposition time increased, both the top as well as bottom ITO film thickness obtained from the fitting XRR result also increased.

Table 5-1 the ITO deposition time and the trilayer thickness obtained from the XRR measurement.

Sample	ITO Deposition time (sec.)	Top ITO thickness (nm)*	Au thickness (nm)*	Bottom ITO thickness (nm)*
S1	100	11	2.9	11
S2	200	22	2.8	22
S3	300	33	2.9	33
S4	400	44	2.8	44
S5	500	55	2.9	55

*Obtained from the fitting XRR result

Figure 5-3(a) shows the X-ray diffraction (XRD) spectra of ITO/Au/ITO trilayer with different ITO layer thickness. The top and bottom ITO layer thicknesses are increased simultaneously



from 11 nm to 55 nm. From the XRD spectra, there are two peaks being observed, i.e. one broad peak and one sharp peak. The sharp peak position is 35.1° , which corresponds to the ITO (400) peak and has been confirmed by the diffraction spectra of ITO powder shows in Figure 5-3(b). In order to observe the effect of the thickness on the crystallinity of the top ITO layer. Figure 5-4 plots the Full Width Half Maximum (FWHM) of ITO (400) peak as a function of film thickness. Indeed, the FWHM value is related to the average grain size of the film as calculated by Scherrer's equation,

$$D = \frac{0.9\lambda}{\beta \cos\theta} \quad (5.33)$$

where D is the average grain size, β is the FWHM of the peak and θ is the Bragg's diffraction angle. As the FWHM value is inversely proportional to the average grain size, therefore the grain size is increased when the film thickness increase, i.e. as film thickness increased, better crystallinity of the film is resulted.

As shown in Figure 5-3 (a), the sharp ITO (400) peak is believed to be arisen from the top ITO layer and we believed that the bottom layer is still in amorphous form as we will explain in next chapter.

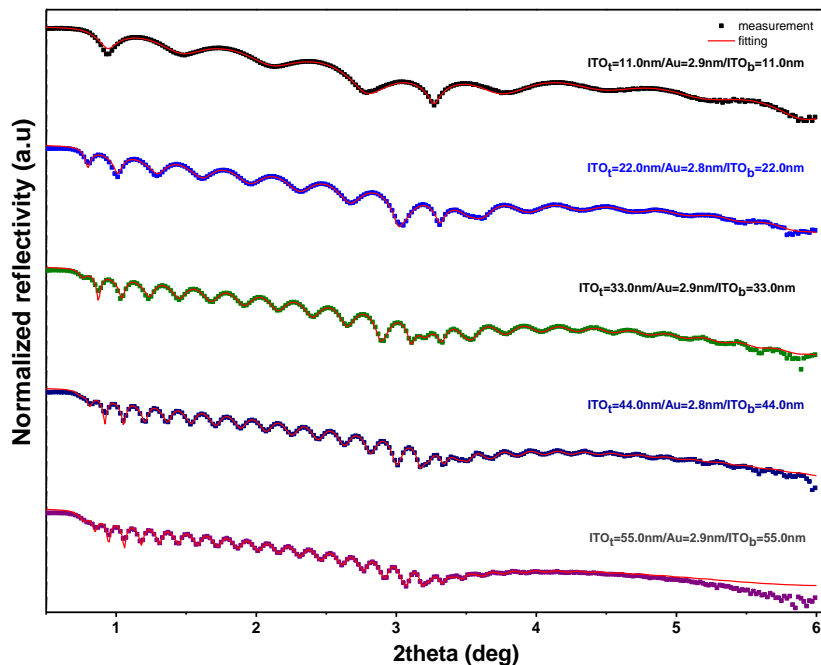


Figure 5-1 XRR pattern of ITO (t nm)/Au (2.9 nm)/ITO (t nm) trilayer films with varying values of t .

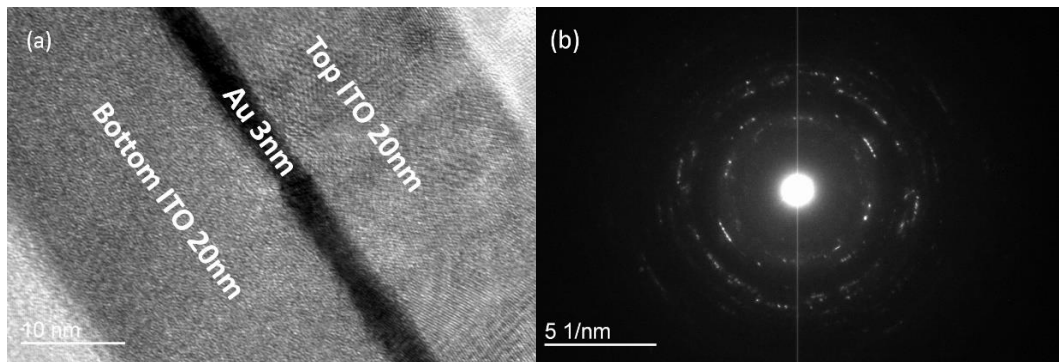


Figure 5-2 (a) Cross-sectional TEM of the ITO (20 nm)/Au (3 nm)/ITO (20 nm) sample. (b) Selected-area diffraction patterns of top ITO layer, showing the polycrystalline structure.

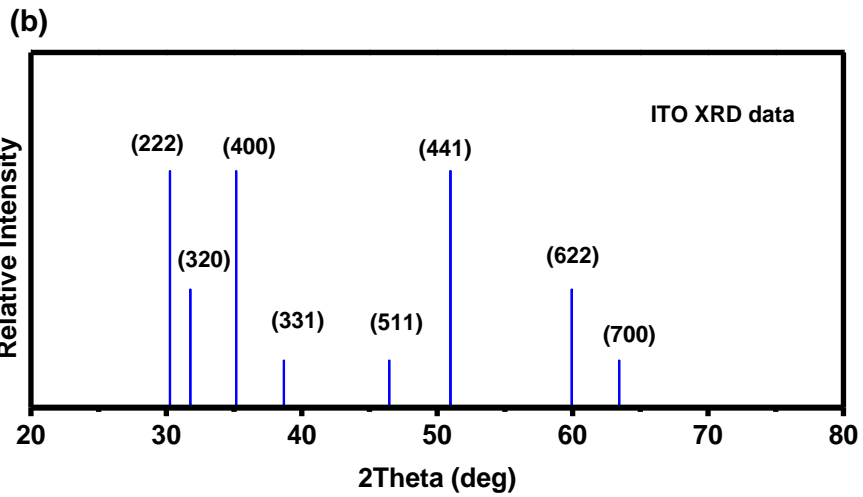
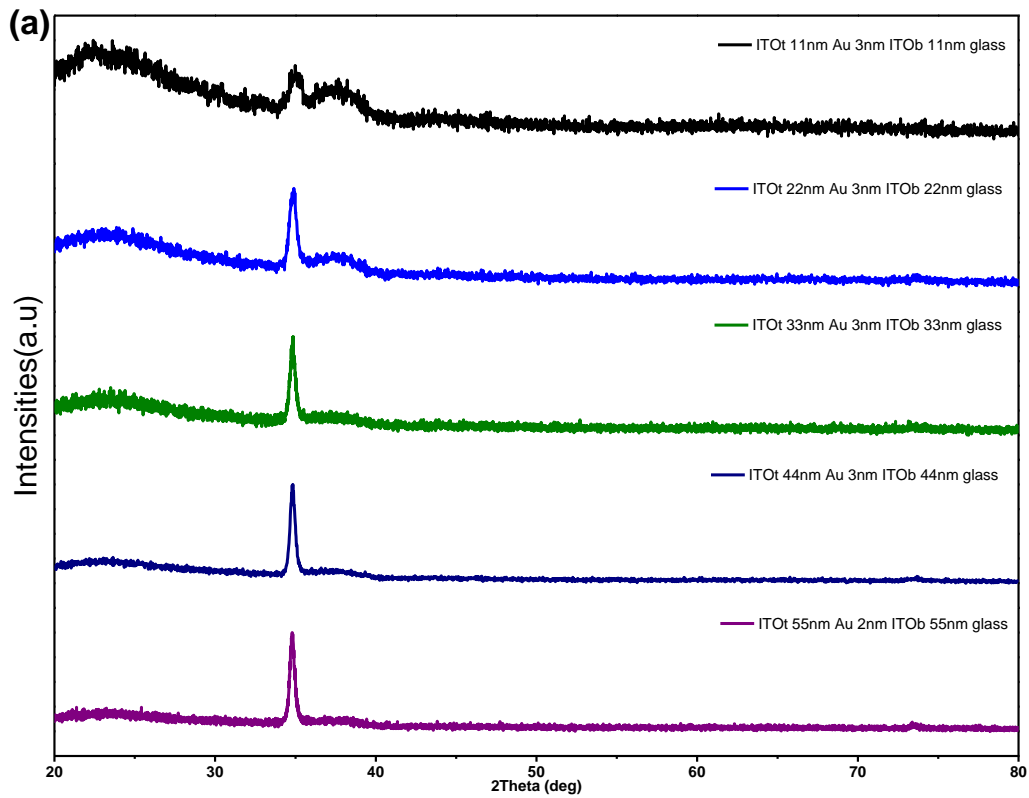


Figure 5-3 (a) XRD pattern of ITO/Au/ITO trilayer with different ITO layer thicknesses (both top and down ITO thickness in trilayer structure remain the same). (b) X-ray diffraction pattern of ITO ceramic target.

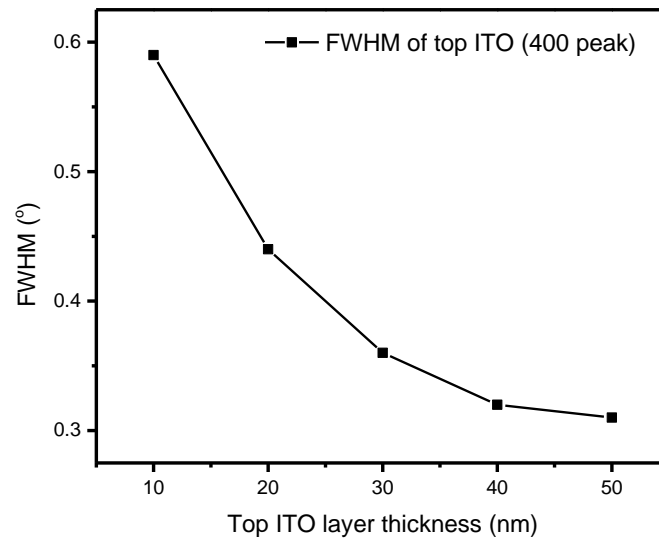


Figure 5-4 FWHM of (400) peak of ITO/Au/ITO multilayers against top ITO thickness

To verify the fitting result from XRR patterns, a cross-section TEM micrograph on the structure of the ITO/Au/ITO system were obtained. TEM micrograph shown in Figure 5-2(a). For the denser materials, the scattering effect on the electrons is more significant compared with less dense material. i.e. less electrons can pass through the sample and will be collected by the detector. Therefore, the gold layer is observed as a darker view compared with the less dense ITO thin films. As a result, it is noticed that an ultrathin darker gold layer is inserted in between two brighter ITO layers. From the micrograph the thicknesses of each layers are confirmed, and the layer thicknesses matched well with the fitting in the XRR measurement Apart from the thickness measurement, the uniformity and crystallinity can also be observed by such technique with the resolution up to atomic scale. The ultrathin gold film shows a long-range uniformity and well-defined boundaries sandwiched with two ITO thin film. Thus, the multilayer film can be considered as the vertical stacking layers without interface interactions.

Figure 5-2(b) represents the electron diffraction pattern of top ITO layer, instead of the continuous ring diffraction patterns due to the amorphous material, the top ITO layer shows some clear and distinguishable spot in the diffraction patterns. Thus, the top ITO layer is polycrystalline in nature instead of amorphous.



5.3 Electrical properties of ITO_t/Au/ITO_b trilayer structure.

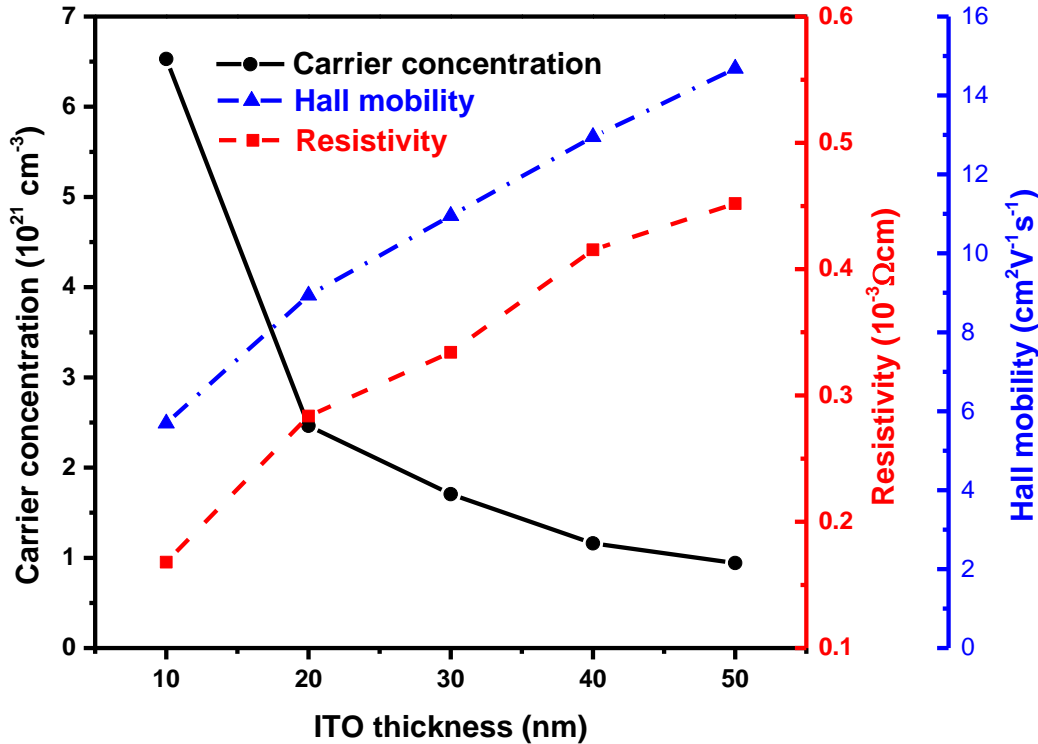


Figure 5-5 carrier concentration, Hall mobility and resistivity as a function of ITO thickness

In this section, we try to study the effect of top and bottom ITO film thickness on the electrical properties of the trilayer structure. However, the electrical as well as optical properties of the ITO films are highly depended on the processing conditions [92, 93], thus in order to eliminate the effects of processing conditions on the electrical and optical properties of the structures, the ITO films in the experiment were prepared under the same processing conditions, such as the O₂/Ar ratio and pressure and the substrate temperature during deposition. In this case, we believe that all the ITO films should be identical in the intrinsic properties such as oxygen vacancies and doping concentration. The variation of electrical properties observed in the hall measurement only arisen from the film thickness and difference in crystallinity, not due to their intrinsic properties variation.

The electrical properties such as carrier concentration, hall mobility and resistivity of the ITO trilayer sample were measured by a Keithley 6221 Current Source and a Keithley 2182A nanovoltmeter using the van der Pauw configuration, under a 0.5 T magnetic field.



Compared with the pure ITO film (carrier concentration $n_i \approx 4.48 \times 10^{19} \text{ cm}^{-3}$, carrier mobility $\mu = 20.4 \text{ cm}^2 \text{ V}^{-1} \text{ s}^{-1}$ and resistivity $\rho = 6.4 \times 10^{-3} \text{ } \Omega \text{ cm}$), it is noticed that the carrier concentrations of the ITO/Au/ITO structures are higher. It is believed that the enhancement of the trilayer carrier concentration is due to the carrier injections from the electron- rich Au layer being inserted between the ITO layers.[94] When the top and bottom ITO thickness increases, the carrier injections become insignificant and the overall carrier concentration approached to pure ITO value.

On the other hand, the Hall mobilities of the trilayer structures are smaller than that of the pure ITO ($\approx 20 \text{ cm}^2 \text{ V}^{-1} \text{ s}^{-1}$) because the carrier movement is severely affected by the interface scattering between Au and ITO layers.[95] However, as the film thickness increases, the effect of the interface scattering becomes less significant. The resistivity of the pure ITO film ($\approx 6.4 \times 10^{-3} \text{ } \Omega \text{ cm}$), although possessing higher carrier mobility but lower carrier concentration, is much larger than that of the multilayer structures. Among the ITO/Au/ITO multilayer films, the carrier concentration gradually decreases while the mobility gradually increases with rising ITO film thickness. Provided that the electrical resistivity is reciprocal of the product of charge mobility and carrier concentrations, the electrical resistivity only changes slightly in the multilayer structure with increasing ITO thickness, therefore the increase in the mobility will cause the charge carrier concentrations to be decreased.

Furthermore, we believe that the larger grain size of the top ITO film also improve the mobility of the ITO films. From the XRD spectra shown in Figure 5-3 and Figure 5-4, the average grain sizes increases as indicated by smaller FWHM values. The larger grain size reduces the number of grain boundaries, which will reduce the grain boundary scattering effect. Thus the charge mobility will therefore increase.[96]

5.4 Optical properties of ITO_t/Au/ITO_b trilayer structure.

The optical and dielectric properties of the ITO/Au/ITO multilayer films were measured by a Spectroscopic Ellipsometer with reflection mode. The light source was incident on the sample with 70° angle and the detector collected the reflected light at -70° angle. The polarization of the incident light was set at 0° rotation and the analyzer was set to 45° rotation. The spectrum was measured from 400nm to 2000nm with a 10nm increment. The optical permittivity of the



sample was obtained by fitting the ellipsometric angles ψ and Δ using the WinElli II software with Lorentzian optical models.

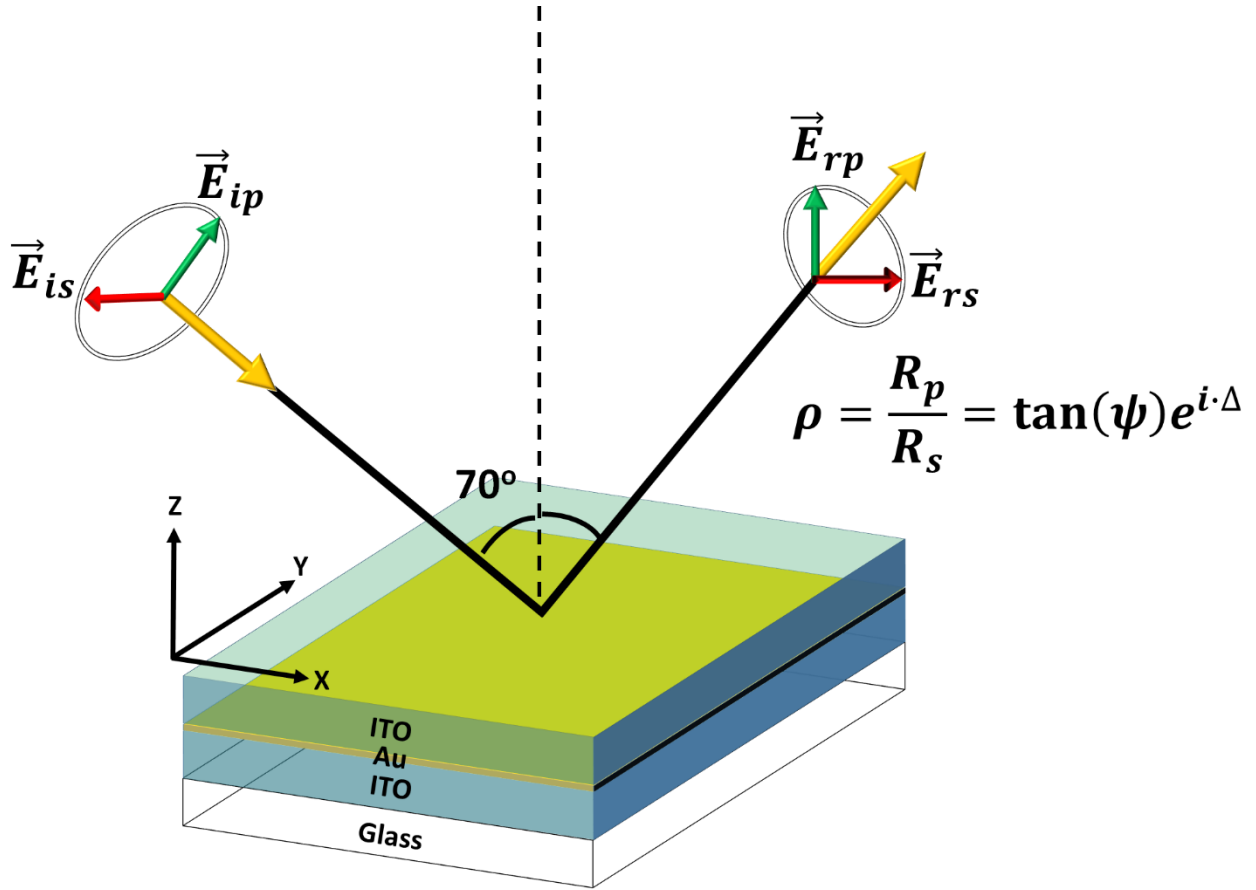


Figure 5-6 The schamitioc diagram of reflection ellipsometry

$$\varepsilon = \varepsilon_{\infty} + \frac{\omega_p^2}{-\omega^2 + i\Gamma_D \omega} + \sum_{j=1}^2 \frac{f_j \omega_{oj}^2}{\omega_{oj}^2 - \omega^2 + i\Gamma_j \omega} \quad (5.34)$$

$$\varepsilon = \varepsilon_{\infty} + \left(\frac{-\omega_p^2}{\omega^2 + \Gamma_D^2} \right) - i \left(\frac{\Gamma_D \omega_p^2}{\omega^3 + \Gamma_D^2 \omega} \right) + \sum_{j=1}^2 \frac{f_j \omega_{oj}^2}{\omega_{oj}^2 - \omega^2 + i\Gamma_j \omega} \quad (5.35)$$

$$\omega_p^2 = \frac{n e^2}{\varepsilon_0 m^*} \quad (5.36)$$

Here, ε_{∞} is the high frequency permittivity, Γ_D is Drude damping term. For the Lorentz oscillators, the f_j , Γ_j are the strength of oscillator and the damping constant of Lorentz oscillator respectively, ω_{oj}^2 is the resonant angular frequency of the oscillator which is related



to the energy band gap of materials. ω_p is the plasma frequency of the material, the relation is given in Equation (5.36). Here the plasma frequency is directly proportional to the carrier density n and inverse proportion to the effective electron mass of the materials.

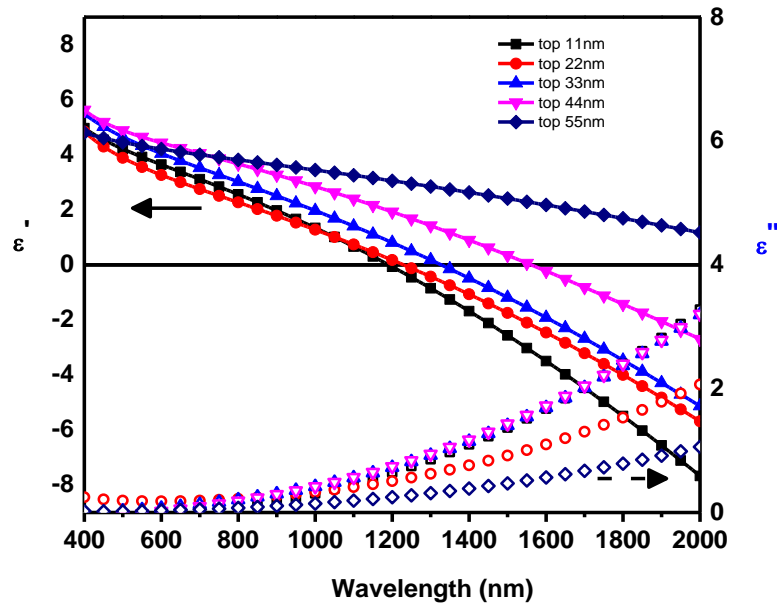


Figure 5-7 Real (solid symbol) and imaginary (open symbol) parts of permittivity against wavelength of Top ITO layer in the trilayer samples.

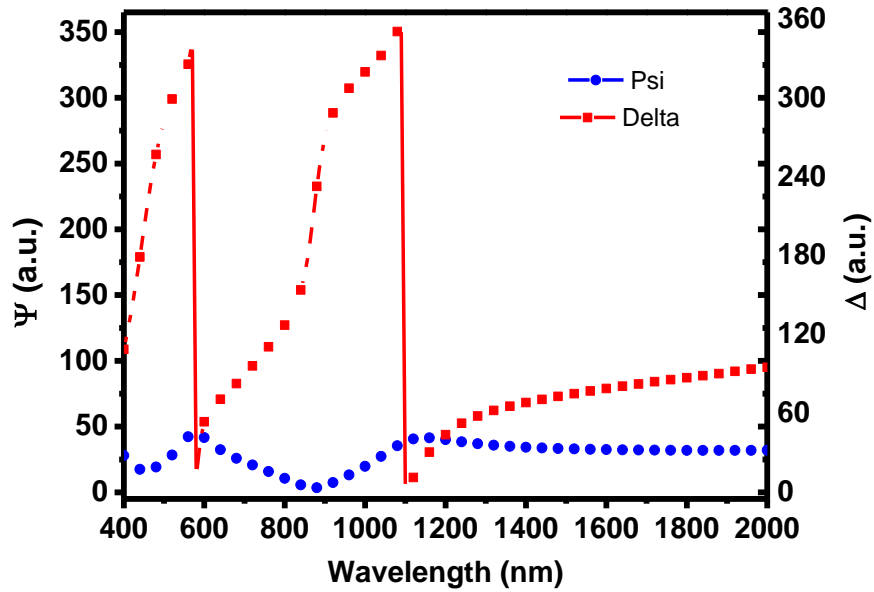


Figure 5-8 ψ and Δ of the ITO (22 nm)/Au (3 nm)/ITO (22 nm) sample measured by spectroscopic ellipsometry in the 400-2000 nm wavelength range.

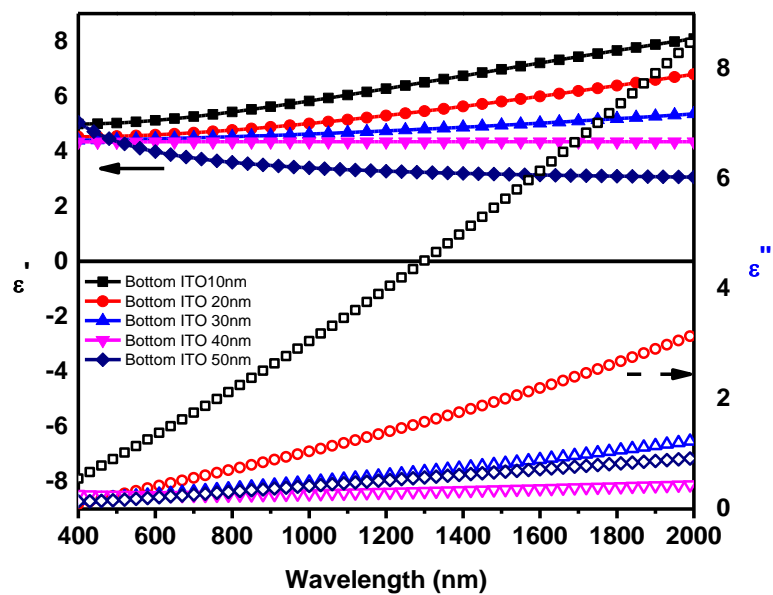


Figure 5-9 real (solid symbol) and imaginary (open symbol) parts of permittivity against wavelength of bottom ITO layer in the trilayer samples

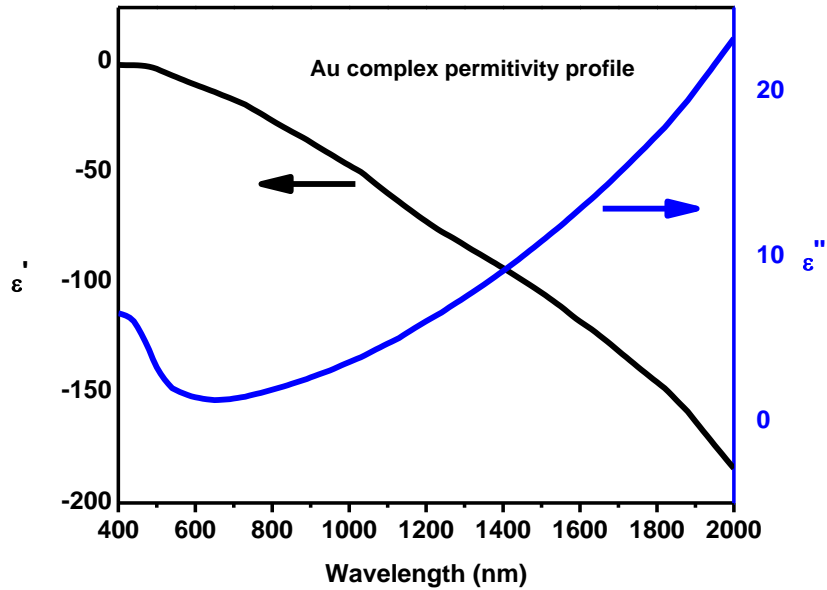


Figure 5-10 The permittivity profile of gold thin film.

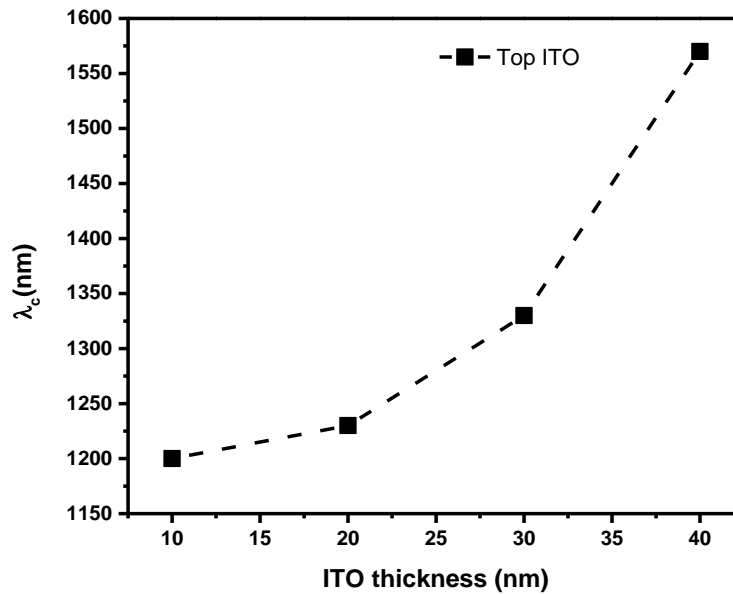


Figure 5-11 crossover wavelength of bottom and upper ITO layers

Figure 5-7 shows the variation of the dispersion relation of the top ITO layer with different thickness. As discussed in the last part, the top ITO is polycrystalline compared with the bottom amorphous ITO. The ITO top layer dispersion relation has been described using the Drude-Lorentz model in reported as the literature [97]. For the real permittivity, the plasma frequency



can be characterized by the crossover wavelength, at which the real-part permittivity changes from positive to negative.[98] It is well known that the dielectric properties is strongly related to the electrical properties. As the ITO thickness increased, the free carrier density decreases accordingly as shown in Figure 5-5. The decrease in the carrier concentration is the reason of the red shift of the crossover wavelength of top ITO layer, because according to the Drude-Lorentz model, the plasma frequency is directly proportional to the square root of carrier density. Also, the plasma oscillation frequency i.e. thickes film is inversely related to the wavelength. Thus, ITO layer with less free carrier concentration will result in a larger crossover frequency. The imaginary part of permittivity is responsible for the optical losses due to plasma damping and free carrier absorptions. For the thinner sample with larger free carries, the degree of free carrier absorption is also larger. [99] So, the ϵ'' will increase for NIR wavelength. The degree of increment for the thinner ITO film will be also higher and decrease with thickness.

Figure 5-9 represents the permittivity profiles of the bottom ITO films. Unlike top ITO layer, the real part permittivity of the bottom layer shows more positive profile and the crossover point within the spectral range generally is not observed. The reason can be accounted for the difference in the crystallinity which has been confirmed by the XRD in the structural characterizations part. The amorphous bottom ITO layers only give a slight variation in the real permittivity. However, the imaginary permittivity of the bottom ITO is larger than that of the top counterparts. The amorphous layer is responsible for more optical loss due to various mechanism such as light scattering.[100]

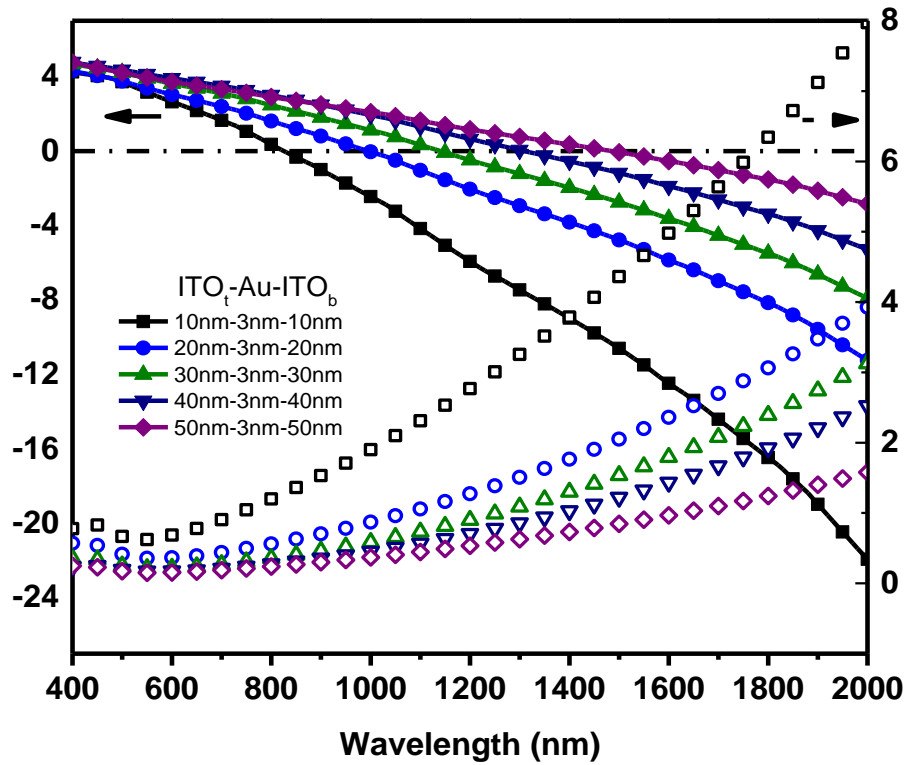


Figure 5-12 ϵ_{\perp} with the real part (solid symbol) and the imaginary part (open symbol) of the trilayer layer samples calculated by effective medium approximation.

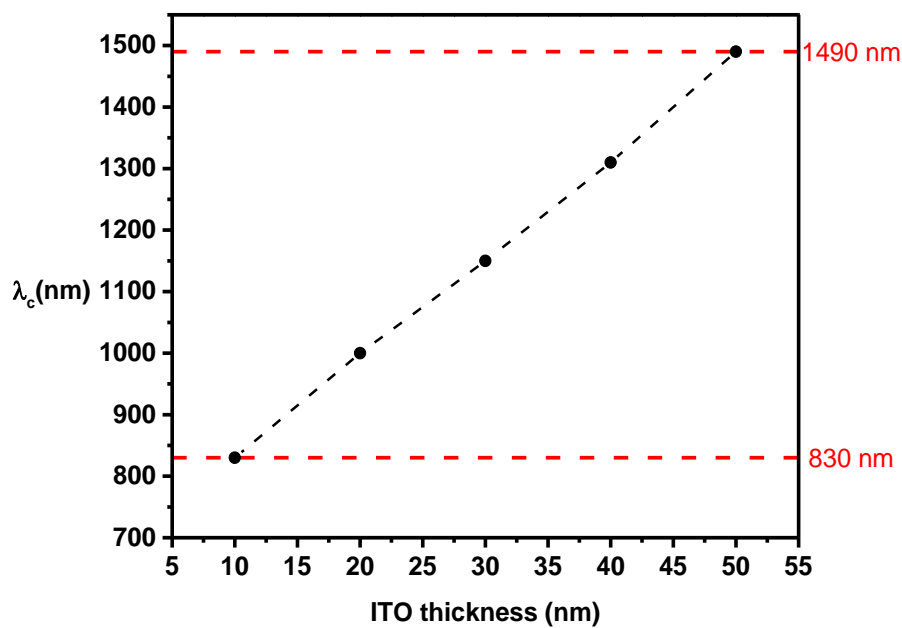




Figure 5-13 crossover wavelength as a function of bottom and top ITO thickness in the trilayer sample.

For the semiconductor-metal-semiconductor multilayer structure, an effective model is needed to estimate the collective effect contributed by the three individual layers. Previous reported effective medium approximation on multilayer hyperbolic metamaterials has been used to treat the multilayer structure as a single optical anisotropic medium with two effective dielectric tensors (ϵ_{\perp}) and ($\epsilon_{\parallel}^{-1}$) on the parallel and perpendicular directions.[101] The derivation of the effective medium approximation was based on the Maxwell's equation with appropriate boundary conditions. The expression is given in equation (5.37) and (5.38), and the calculation of effective tensors are based on the electric permittivity and the thickness of each layers. For the light incident on the vertical staked multilayer structures as shown in Figure 5-15, the light propagation will be affected by the perpendicular dielectric tensor as reported. The perpendicular effective tensor of trilayer structure is shown in Figure 5-12. Due to the optical anisotropy of this metal-dielectric multilayer stacking, when one of the effective permittivity become negative in particular wavelength range (either $\epsilon_{\perp} > 0$ and $\epsilon_{\parallel}^{-1} < 0$ or $\epsilon_{\perp} < 0$ and $\epsilon_{\parallel}^{-1} > 0$) the dispersion relation will become a hyperbola with a extraordinary effect such as negative refractive index.

$$\epsilon_{\perp} = \frac{1}{d_{ITO_{top}} + d_{Au} + d_{ITO_{bottom}}} (\epsilon_{ITO_{top}} d_{ITO_{top}} + \epsilon_{Au} d_{Au} + \epsilon_{ITO_{bottom}} d_{ITO_{bottom}}) \quad (5.37)$$

$$\epsilon_{\parallel}^{-1} = \frac{1}{d_{ITO_{top}} + d_{Au} + d_{ITO_{bottom}}} \left(\frac{d_{ITO_{top}}}{\epsilon_{ITO_{top}}} + \frac{d_{Au}}{\epsilon_{Au}} + \frac{d_{ITO_{bottom}}}{\epsilon_{ITO_{bottom}}} \right) \quad (5.38)$$

Where $d_{ITO_{top}}$, d_{Au} , $d_{ITO_{bottom}}$ are the thicknesses of each layer and the $\epsilon_{ITO_{top}}$, ϵ_{Au} , $\epsilon_{ITO_{bottom}}$ are the complex permittivities of each layer obtained from ellipsometry measurement.

Then, the refractive index and extinction coefficients of the trilayer structure, \tilde{n} can be given by the following equation.



$$\tilde{n} = n + i\kappa$$
$$n = \sqrt{\frac{|\tilde{\epsilon}_{\perp}| + \tilde{\epsilon}_{\perp,r}}{2}} \quad (5.39)$$
$$\kappa = \sqrt{\frac{|\tilde{\epsilon}_{\perp}| - \tilde{\epsilon}_{\perp,r}}{2}}$$

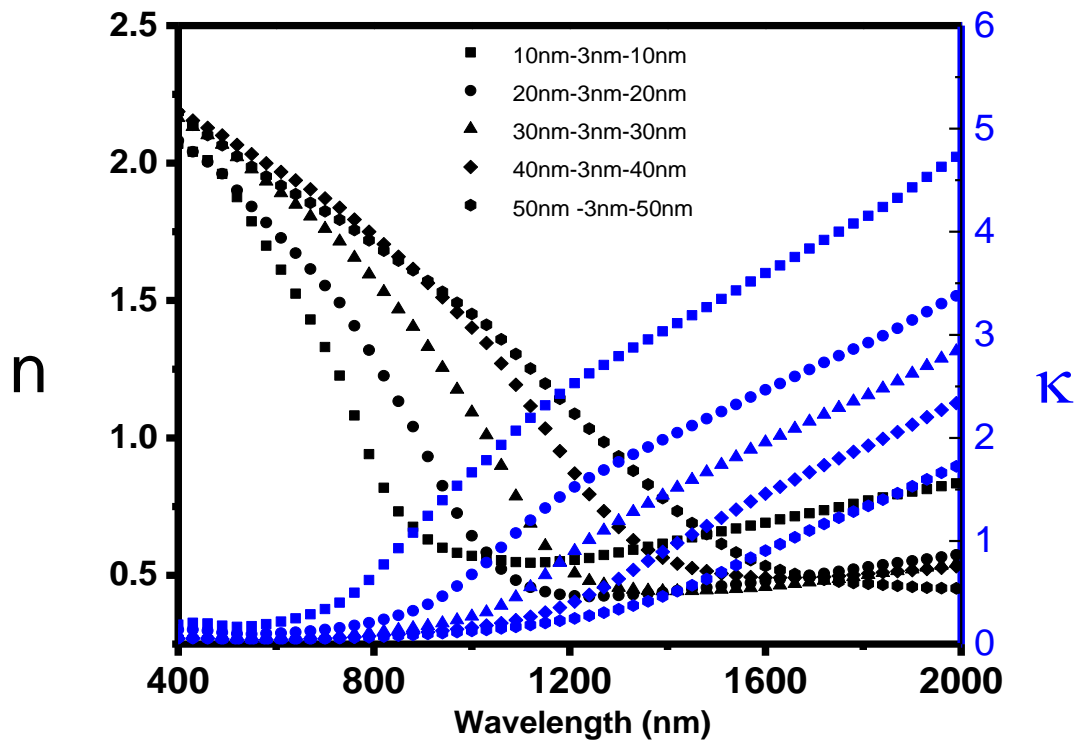


Figure 5-14 The effective refractive index and extinction coefficient of trilayer structure.

Figure 5-17(a) show the spectral transmittance of trilayer structures with different top and bottom ITO thickness measured by the UV-Vis-NIR spectrometer from 400nm to 2000nm. Both trilayer structures show over 60% transmittance in the visible range. Thus, even though an Au layer was inserted, the overall transmittance of ITO did not affect much. The inserted gold layer is thin enough to preserve the transparency of the whole structure. As the thickness of the ITO film increases, the observed ripple on the transmittance curve is due to the collective interference effect from each interface (ITO/Au and ITO/glass). For the long wavelength, the transmittances drop to 40%, this is a typical effect due to the free carrier absorption.



To estimate the validity of using EMA to model the trilayer samples. The effective transmittance of the trilayer samples with different thickness of sandwiched ITO layer in the symmetrical structures has also been investigated. The ellipsometry data was verified by the simulation of transmittance spectra of multilayer structure. The simulated transmittance was calculated by the Transfer Matrix Method (TMM) [52]

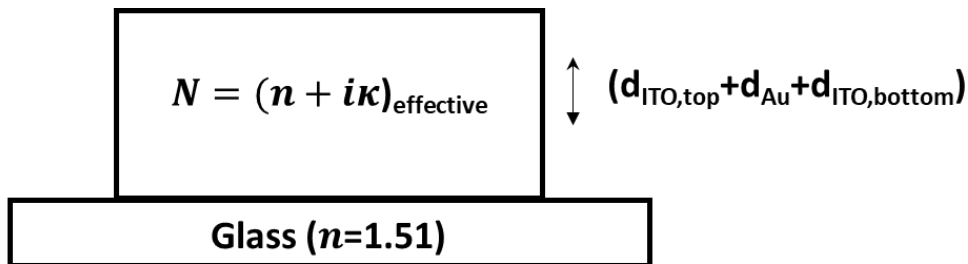


Figure 5-15 schematic diagram of TMM modeling trilayer structure by effective media approximation (EMA).

For the comparison, the transmittances were also simulated layer by layer using refractive index of individual layer to further confirm the validity of EMA. As Figure 5-16 shown, the calculation was based on the film thickness and the complex refractive index retrieved from the ellipsometry measurement. The calculated spectra were shown in Figure 5-17(c), the simulation of transmittance shows a similar tendency over the whole spectral range including the near band gap range and long wavelength including the position of peak transmittance due to the interference effect.

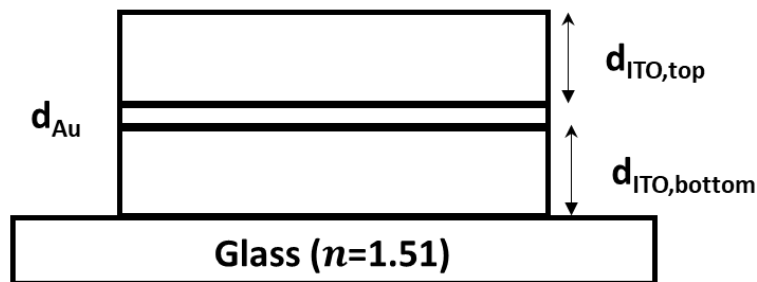


Figure 5-16 Schematic diagram of the simulated of ITO/Au/ITO layer by layer structure.

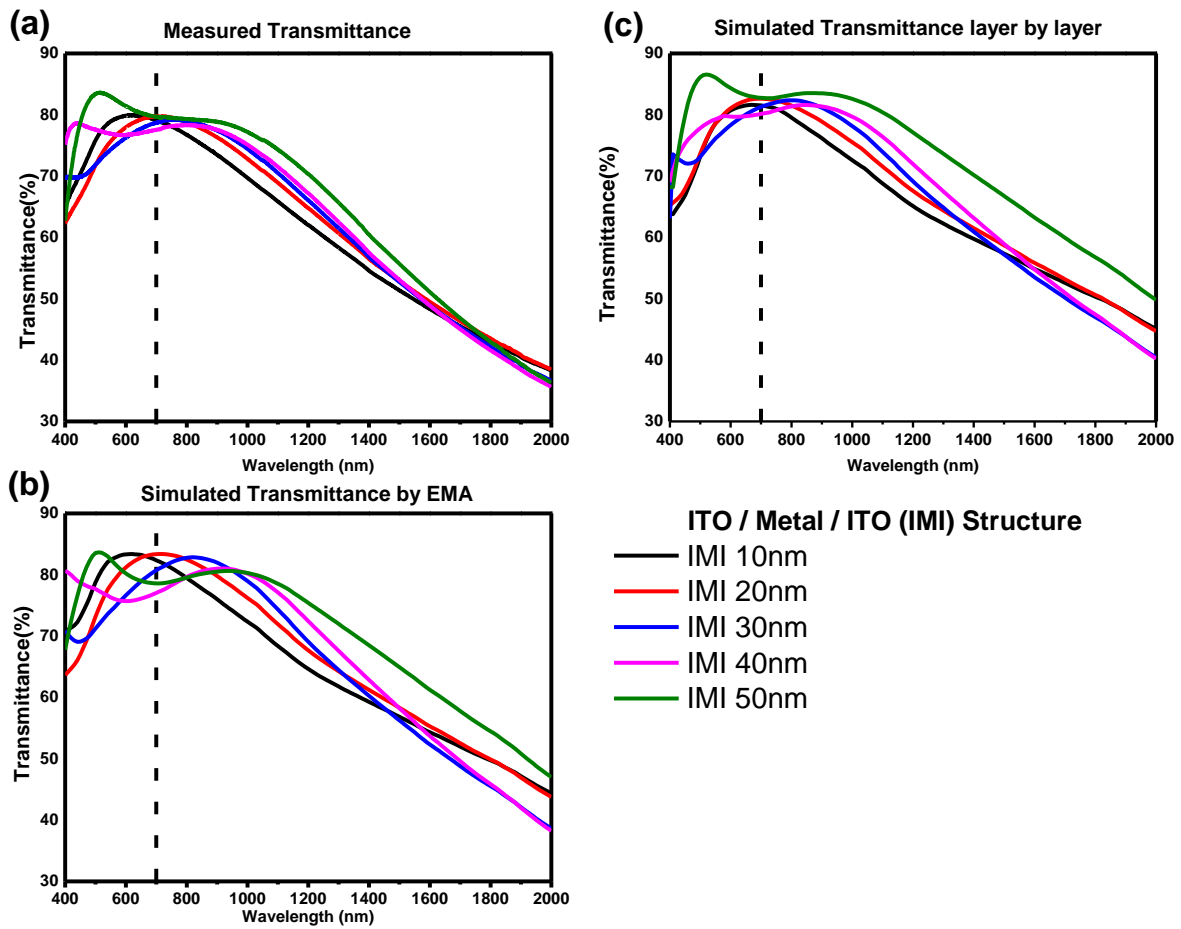


Figure 5-17 (a) spectral transmittance of trilayer samples with different top and bottom ITO thickness. (b) Simulation of transmittance of ITO/Au/ITO trilayer structure by Effective media approximation (EMA). (c) Simulation of transmittance of ITO/Au/ITO trilayer structure layer by layer.



5.5 Evaluation of trilayer structure into plasmonic application

After discussing the effective permittivity of the multilayer structure, it is needed to evaluate the applicability of such structure in various potential applications. For the materials into different applications, the performance can be compared by using a quality factor, so-called the figures-of-merit. Most of the quality factors are a function of the real part ϵ_r and imaginary part ϵ_i permittivity of such material. Since the ϵ_r is describing the field distribution in the materials which is an important consideration of the overall performance of the devices. On the other hand, the imaginary part ϵ_i quantifies the optical loss, which is also a crucial factor to evaluate a device performance.

In this section, the conventional plasmonic devices, which can be divided into three classes: surface plasmon polariton (SSP) waveguides, localized surface plasmon resonance-based devices (LSPR device) and transformation optics (TO) devices, will be discussed.

For LSPR devices, the quality factor is defined in Equation (5.40), The LSPR system enhances the localized field, thus the quality factor should be the ratio between the enhanced local field and the incident field. For the multilayer thin film system, the effective medium approximation has proven to be a reliable way to describe the multilayer structure using an effective permittivity. Therefore, the quality factor for LSPR is defined as the imaginary part of the effective permittivity divided the negative of the real part permittivity. Figure 5-18 shows the LSPR quality factor of the trilayer sample. Noticed that the curve only plotted in the range $Q_{LSPR} > 0$, because only at the positive quality factor region, the incident field is enhanced. The result shows that manipulating thickness of top and bottom ITO not only can control the spectral range of the LSPR device, but also enhance the local field to approximate maximum 2.5 to 3 times depends on the thickness of ITO layer.

$$Q_{LSPR}(\omega) = \frac{-\epsilon''(\omega)}{\epsilon'(\omega)} \quad (5.40)$$

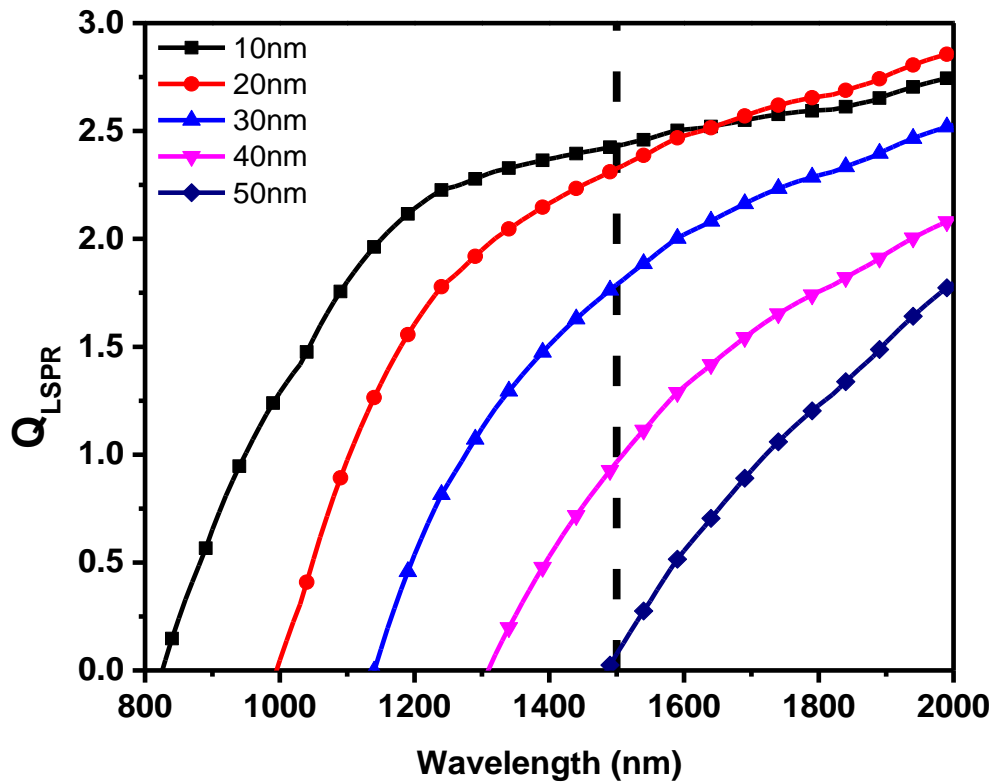


Figure 5-18 . Quality factors of the trilayer samples for localized surface plasmon resonances (Q_{LSPR})

Regarding the SPP system, the surface plasmons are the quantized state of the localized electromagnetic surface wave in the interface between the metal and dielectric materials.[51] The surface plasmon can couple with the light strongly to enhance the light matter interactions forming a surface plasmon-polariton waveguides to propagate the wave along the interface. [102] Since the trilayer structure has been regarded as a homogeneous material by effective media approximation. Therefore, the surface plasmon in the interface between the gold and two ITO layers was neglected. The SPR system discussed is in between the trilayer thin film and the silicon dioxide interface. The SPR system quality factor is given by Equation (5.41), the $\epsilon_{\perp}(\omega)$ is the effective permittivity tensor of the plasmonic material reported in the last part, and the ϵ_d is the electric permittivity of the dielectric material. Here the silicon dioxide was chosen with $\epsilon_d=2.37$ and set to be a constant in the spectral range measured. Figure 5-20 plots the quality factor trilayer samples under SPR mode. Thus, to achieve a large quality factor, the negative ϵ_{\perp} should be large and the ϵ_{\perp} should be as small as possible. The result shows the

trilayer structure can couple the surface plasmon in the visible range with the largest quality factor except the 10nm sample that have better performance in the long wavelength range.

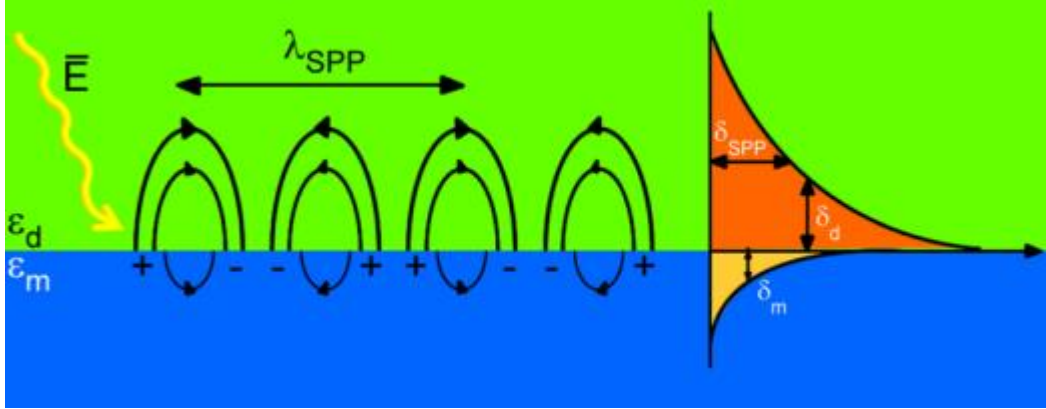


Figure 5-19 Schematic diagram of surface plasmon propagation and the related parameters.[103]

$$Q_{SPP}(\omega) = \frac{\epsilon_{\perp}^{\prime}(\omega) + \epsilon_d^{\prime}(\omega)}{\epsilon_{\perp}^{\prime}(\omega)\epsilon_d^{\prime}(\omega)} \frac{\epsilon_{\perp}^{\prime}(\omega)^2}{\epsilon_{\perp}^{\prime}(\omega)} \quad (5.41)$$

The surface plasmon polariton profile can be characterized by different parameters such as the propagation length δ_{prop} (the measured distance of a SPP propagation such that the intensity of the SPP mode drop to the 1/e of the original value), penetration lengths δ_{conf} (the penetration distance inside the material) and the SPP wavelength λ_{SPP} (the SPP oscillation period). In the relation, the ϵ_m^{\prime} and $\epsilon_m^{\prime\prime}$ is the real and imaginary permittivity of the metal layer, which is the perpendicular effective tensor ϵ_{\perp} of trilayer film. The λ_0 is the wavelength of free space.

$$\delta_{prop} = \lambda_0 \frac{\epsilon_m^{\prime}}{2\pi\epsilon_m^{\prime\prime}} \left(\frac{1 + \epsilon_m^{\prime}}{\epsilon_m^{\prime}} \right)^{3/2} \quad (5.42)$$

$$\delta_{conf} = \frac{\lambda_0}{2\pi} \left| \frac{1 + \epsilon_m^{\prime}}{(\epsilon_m^{\prime})^2} \right|^{1/2} \quad (5.43)$$

$$\lambda_{SPP} = \frac{2\pi}{k_{SPP}} = \lambda_0 \sqrt{\frac{\epsilon_d^{\prime} + \epsilon_m^{\prime}}{\epsilon_d^{\prime} \epsilon_m^{\prime}}} \quad (5.44)$$



In the NIR range, the SPP generally increases the propagation length as the wavelength increases. For the trilayer thickness increases, the maximum propagation length decreases and approached to the pure ITO film's value.

The penetration length determines the confinement of the SPP wave at the metallic layer which measure the compactness of the SPP behavior, for increasing the wavelength, the penetration length approaches to a constant value. The value decreases as the trilayer thickness decreases, which means that the reduction in thickness can impose a high localization of the SPP.

Figure 5-20(c) shows the SPP wavelength of the dielectric-trilayer interface as a function of wavelength, the propagation wavelength is greater than the SPP wavelength in all spectral range. Therefore, it is possible to bring the trilayer into real application.[103]

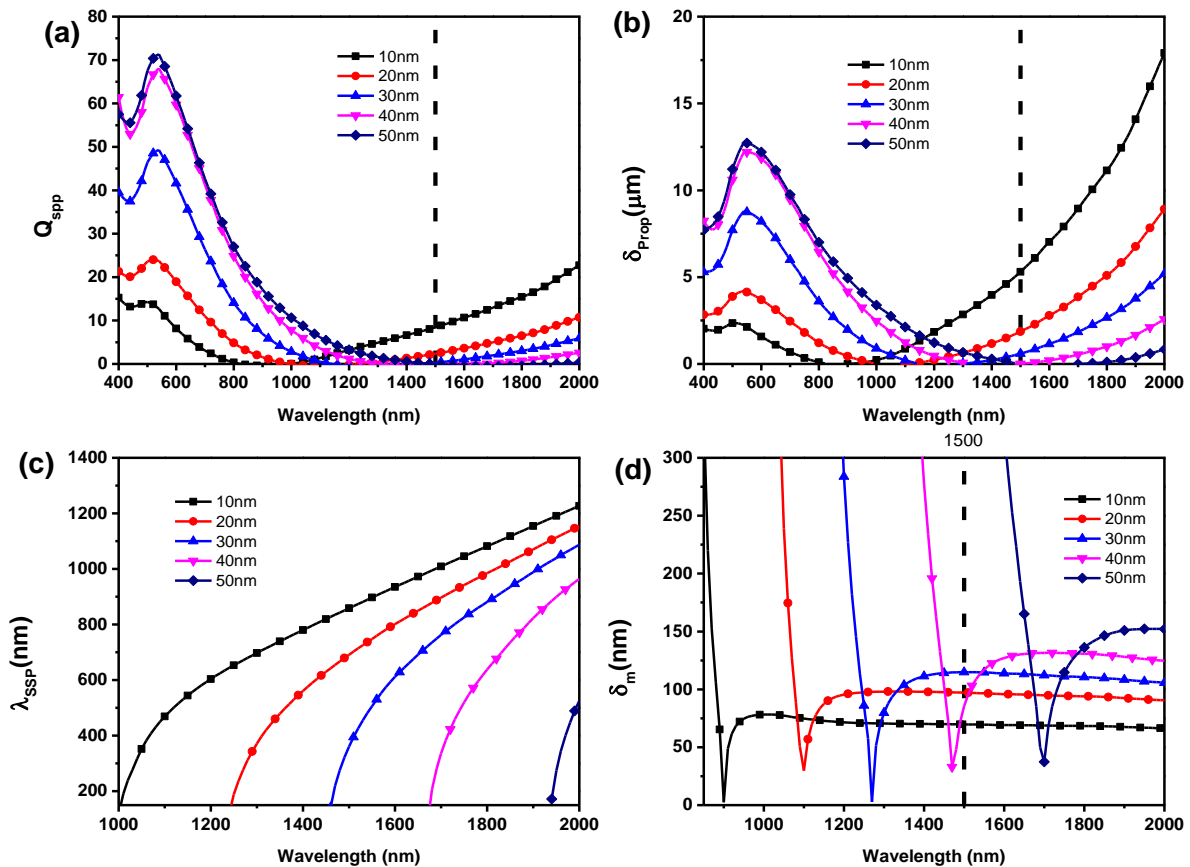


Figure 5-20 (a) Spatial profile of SPP for ITO–Au–ITO film and silicon substrate interface: (a) quality factors Q_{SPP} , (b) propagation length δ_{prop} , (c) SPP wavelength and (d) degree of confinement δ_{conf} .

The transformation optics need to be operated under the metallic response and nearly balanced with the dielectric component from the surrounding, therefore the real effective permittivity



should be negative and approximately equal to the permittivity of air, such that ϵ_d is set to be 1. The quality factor only considers reducing the optical loss in such wavelength, so the quality factor of transformation optics is the reciprocal to the imaginary effective permittivity which quantifies the optical loss. As the optical loss increases, the quality factor is decreased accordingly as shown in Equation (5.45).

$$Q_{TO}(\omega) = \frac{1}{\epsilon_{\perp}''(\omega)} \left(-\epsilon_{\perp}' \sim \epsilon_d \sim 1 \right) \quad (5.45)$$

Table 5-2 lists out the comparison of the conventional noble metals (Au and Ag), TCO (ITO) and the trilayer structure in the quality factor of different plasmonic devices. The table reports the optimal wavelength and the corresponding quality factor on the device applications. Also, the quality factors of the 1.5 μm are also reported. Such special reported wavelength is related to the nanophotonic applications.[98] Although the IMI structure is not comparable to pure metal, the overall performance is better than that of the pure ITO.



Table 5-2 Comparison of quality factors of three different plasmonic devices with different materials. The quality factor of 1.5 μm indicate the nanophotonic applications. (IAI structure data ends at 2 μm) [98]

Material	LSPR&SPR		SPP		TO Devices
	Maximum $Q_{\text{LSPR}}(\lambda)$	Q_{LSPR} (1.5 μm)	Maximum $Q_{\text{SPP}}(\lambda)$	Q_{SPP} (1.5 μm)	Q_{TO} (λ)
Ag	392 (1.08 μm)	39.3	23413 (1.08 μm)	4530	1.82 (326 nm)
Au	16.66 (0.89 μm)	10.63	1410 (1.94 μm)	1140	0.29 (207 nm)
ITO	2.72 (2.3 μm)	N/A	16 (2.3 μm)	N/A	1.54 (1.69 μm)
ITO/Au/ITO (10nm/3nm/10nm)	4.73 (1.34 μm)	4.61	96.0 (2 μm)	53.14	0.65 (0.90 μm)
ITO/Au/ITO (20nm/3nm/20nm)	2.56 (2 μm)	1.30	30.7 (2 μm)	13.28	0.94 (1.1 μm)
ITO/Au/ITO (30nm/3nm/30nm)	2.61 (2 μm)	2.39	44.9 (0.54 μm)	6.51	0.97 (1.27 μm)
ITO/Au/ITO (40nm/3nm/40nm)	1.87 (2 μm)	0.36	65.5 (0.52 μm)	0.14	0.86 (1.47 μm)
ITO/Au/ITO (50nm/3nm/50nm)	1.36 (2 μm)	0.09	173.8 (0.54 μm)	0.008	0.91 (1.70 μm)

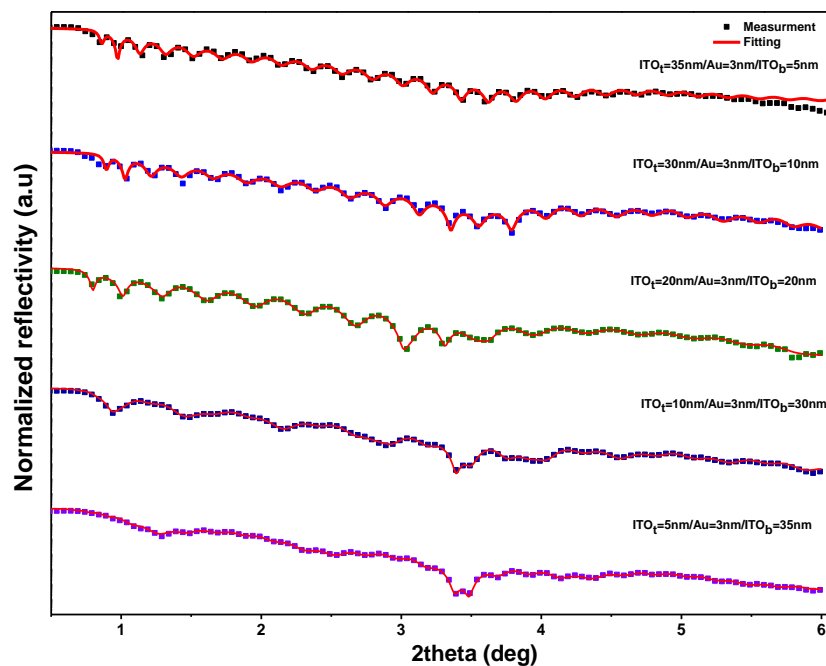


6 Characterization of optical and electrical properties of ITO/Au/ITO multilayer thin film with asymmetric geometry

6.1 Introduction

The Chapter 5 have discussed about the tuning plasmonic properties of multilayer hyperbolic materials by not only controlling the electron rich metal spacer layer, but also changing the upper and lower TCO thicknesses. The manipulation of ITO thickness provides a wide range of plasmonic tuning effect from NIR to visible range, also the optical loss can be remaining very low by keeping an ultra-thin metal layer. The five samples of ITO/Au/ITO multilayer structures (from 11nm to 55nm) with the bottom and top ITO thickness increased simultaneously. A hypothesis is proposed that the top layer of ITO and bottom layer ITO will process different crystallinity due to the insertion of a gold layer, the argument will be further proven in this chapter. As the magnetron sputtering gives a nearly constant growth rate on the ITO film under the same conditions (for example, sputtering power and sputtering ambient pressure), the ITO film thickness can precisely be controlled by the deposition time.

6.2 Structural properties on ITO/Au/ITO sandwich film asymmetric geometry



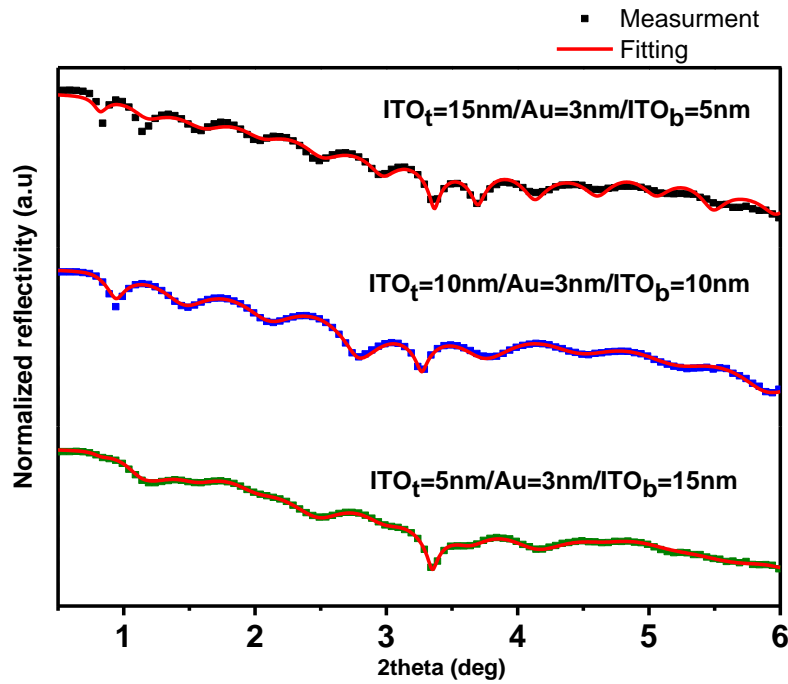


Figure 6-1(a) XRR pattern of ITO (40-t nm)/Au (3 nm)/ITO (t nm) asymmetric trilayer structures. (b) XRR pattern of ITO (20-t nm)/Au (3 nm)/ITO (t nm) asymmetric trilayer structures

Table 6-1 The deposition time and the ITO (top and bottom) thickness of (40-t nm)/Au (3 nm)/ITO (t nm) asymmetric structures.

Sample	Top Deposition time (sec.)	ITO time	Top thickness (nm)*	ITO	Bottom Deposition time (sec.)	ITO	Bottom ITO thickness (nm)*
S1	350		35		50		5
S2	300		30		100		10
S3	200		20		200		20
S4	100		10		300		30
S5	50		5		350		35

*The thickness retrieved from the XRR measurement

Table 6-2 The deposition time and the ITO (top and bottom) thickness of (20-t nm)/Au (3 nm)/ITO (t nm) asymmetric structures.

Sample	Top Deposition time (sec.)	ITO time	Top thickness (nm)*	ITO	Bottom Deposition time (sec.)	ITO	Bottom ITO thickness (nm)*
A	150		15		50		5
B	100		10		100		10



C | 50 | 5 | 150 | 15

*The thickness retrieved from the XRR measurement

Figure 6-2(a) and (b) shows the X ray diffraction spectra of the ITO/Au/ITO trilayer samples of constant total thickness but with varying top and bottom ITO thickness. The XRD results showed that as the top ITO layer thickness was swapped with the bottom ITO thickness, the crystallinity of the overall ITO films varied differently. The sharp peak at 35.1° corresponded to the ITO (400) orientations, also the sharpness of the peak can be characterized by its full width half maximum (FWHM) value. As the peak got sharper, the average grain size become larger according to the Scherrer's equation. As we showed in last chapter, the ITO film grown on the inserted Au layer was much better than the bottom ITO layer i.e. the ITO (400) peak was sharper with smaller FWHM value when the top ITO layer thickness increased. On the other hand, as the bottom ITO thickness increased only a broad peak was observed and showed almost the same grain size as indicated in previous report.[91]

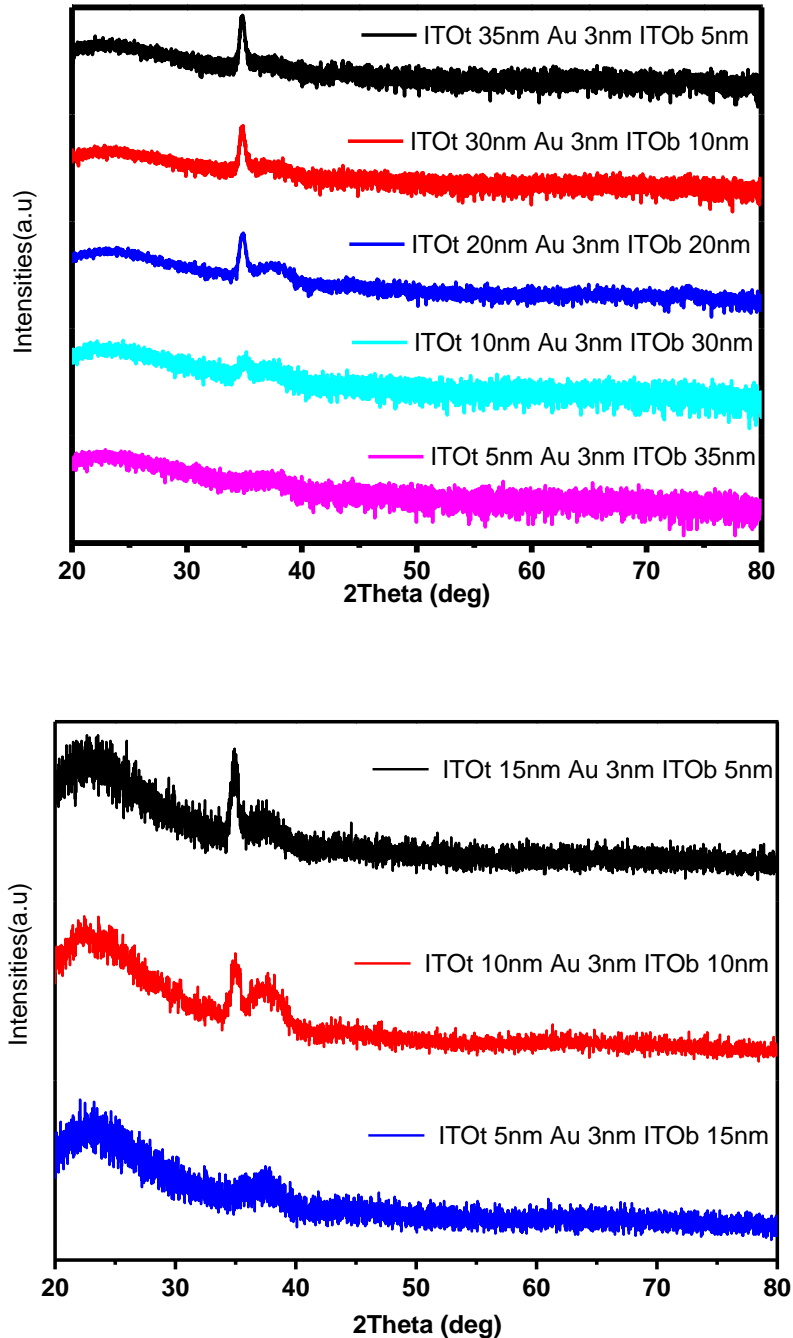


Figure 6-2 (a) XRD pattern of ITO/Au/ITO trilayer with different ITO layer thicknesses (both top and down ITO thickness in trilayer structure remain the same). (b) XRD pattern of ITO/Au/ITO trilayer with different top and bottom ITO thicknesses (total thicknesses are 43nm). (c) XRD pattern of ITO/Au/ITO trilayer with different top and bottom ITO thicknesses (total thicknesses are 23nm).

6.3 Electrical properties of the asymmetric trilayer structures

This section investigated the thickness effect on the electrical properties of the trilayers. In this section, we assumed that the ITO layers separated by a thin gold layer were treated as two



individual layers which process different crystallinity and electrical properties. However, it was difficult to measure the electrical properties layer-by-layer separately. Indeed, the overall sheet resistance was measured. Figure 6-3 is the schematic diagram showing the relationship between the overall measured sheet resistance, R_s , and the sheet resistance of top ITO layer (R_{TCO1}), the inserted Au layer (R_{metal}) and bottom ITO layer (R_{TCO2}). The substrate was assumed to be insulating [33] The effective sheet resistance is given:

$$\frac{1}{R_s} = \frac{1}{R_{TCO1}} + \frac{1}{R_{metal}} + \frac{1}{R_{TCO2}} \quad (6.46)$$

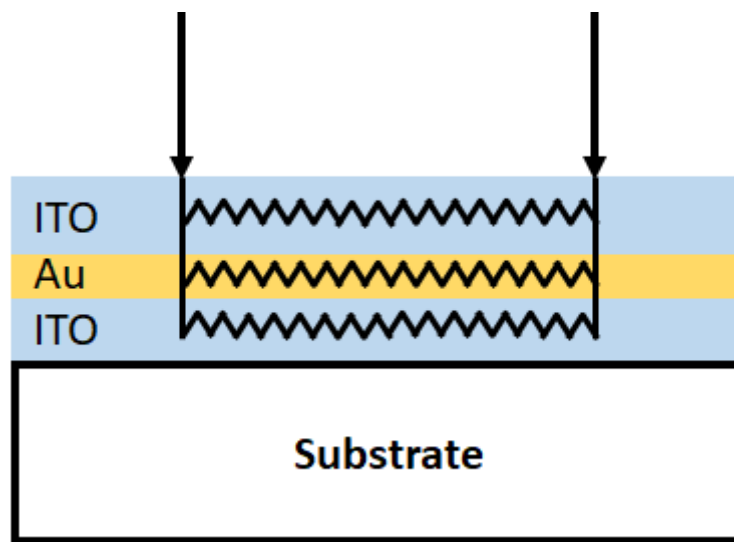


Figure 6-3 Schematic diagram of the electrical properties of TCO/metal/TCO multilayer structures.

To study the effect due to the contribution from single layer, two set of samples with the trilayer structure was investigated. One set of samples with only the top layer ITO thickness was changed, while the bottom ITO and gold thickness was kept constant ($ITO_t = t \text{ nm} / Au = 3 \text{ nm} / ITO_b = 5 \text{ nm}$), where t change from 10nm to 60nm, another set of samples was inverted in geometry ($ITO_t = 5 \text{ nm} / Au = 3 \text{ nm} / ITO_b = t \text{ nm}$) as shown in Figure 6-4.

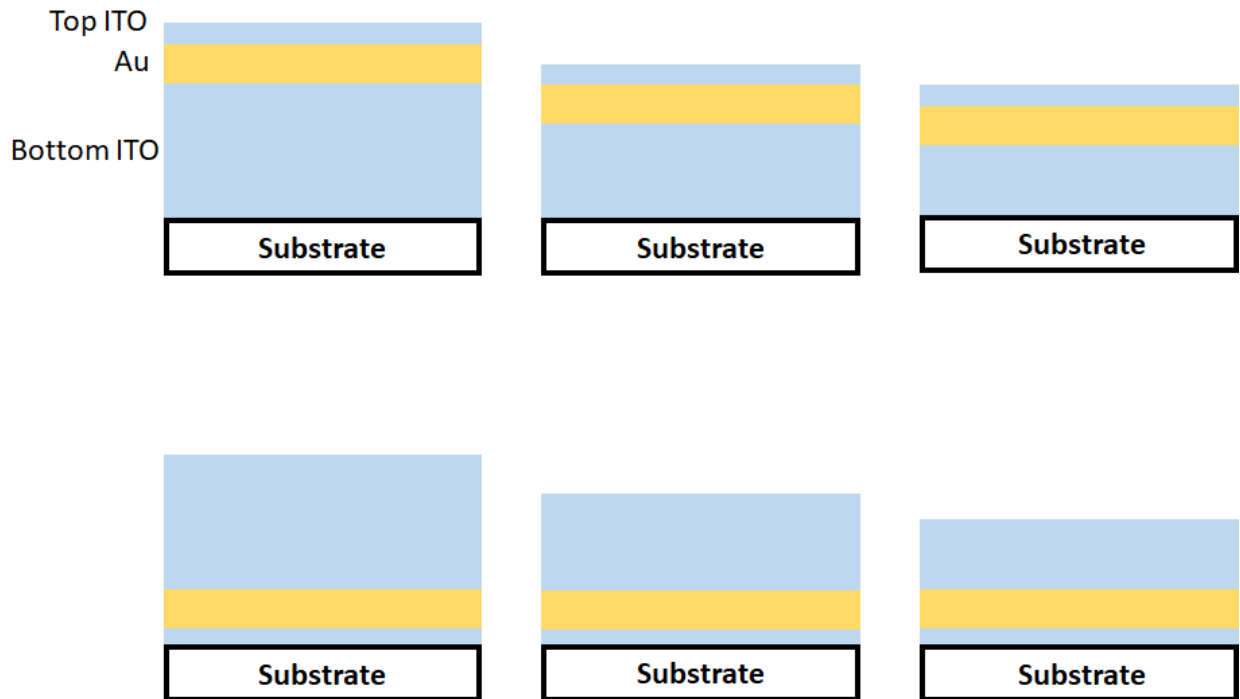


Figure 6-4 The schematic representation of the thickness variation on the asymmetric samples.

The electrical properties including carrier concentrations, hall mobility and resistivity are shown in Figure 6-5. The electrical properties of asymmetric samples with only bottom layer thickness increment from 15nm to 60nm (black curve, bottom and left axis), the top ITO and gold layer was kept 5nm and 3nm respectively and only top layer thickness increment from 15nm to 60nm (colored curve, top and right axis), the bottom ITO and gold layer was kept 5nm and 3nm respectively. Here, the electrical properties of the asymmetric samples with the bottom layer thickness increased from 15 nm to 60 nm while the thickness of top ITO layer and Au layer were kept at 5 nm and 3 nm respectively are shown in black curves, while the electrical properties of the samples with the top layer thickness increased from 15 nm to 60 nm while the thickness of the bottom ITO layer and Au layer were kept at 5 nm and 3 nm, respectively are shown as colored curve. For the carrier concentrations, the sample with increasing top ITO thickness process higher carrier density than the samples with the increasing bottom ITO thickness. It is because thickness of top layer ITO, the grain size of the top layer ITO film also increases according to XRD measurement. The larger grain size results in less grain boundaries and this reduces the scattering effect by the grain boundaries resulting in more free carriers.[104]

However, when either the top or bottom ITO thickness increased, the carrier concentration decreased. The result seems contrast to the previous studies that the carrier concentration



increases with increasing thickness.[105] Noticed that, the carrier concentration in the trilayer sample is in the order of 10^{21} cm^{-3} , which is about ten time larger than that of the pure ITO film as reported.[100] Therefore, the inserted gold layer will introduce more carrier to the ITO films. The reason behind the observation in Figure 6-5(a) maybe related to the carrier injections[106] The increment on the carrier density due to the thicker ITO is dominated by the insert gold layer. While the ITO thickness increase indicates the thickness of whole layer increase, the carrier provided by the gold layer will become insignificant.

Regarding the carrier mobility, the thicker bottom ITO layers generally have higher carrier mobility than the top counterparts. As the carrier in the TCO will have different scattering mechanism which will suppress the carrier mobility. One mechanism is grain boundary scattering, another is the ionized impurity scattering.[107] The ionized impurity scattering will be dominated at high carrier concentrations. Therefore, the mobility will increase with the carrier concentration decreases. Also, all samples with thicker top ITO layer will process lower carrier mobility compared with the thicker bottom ITO layer.

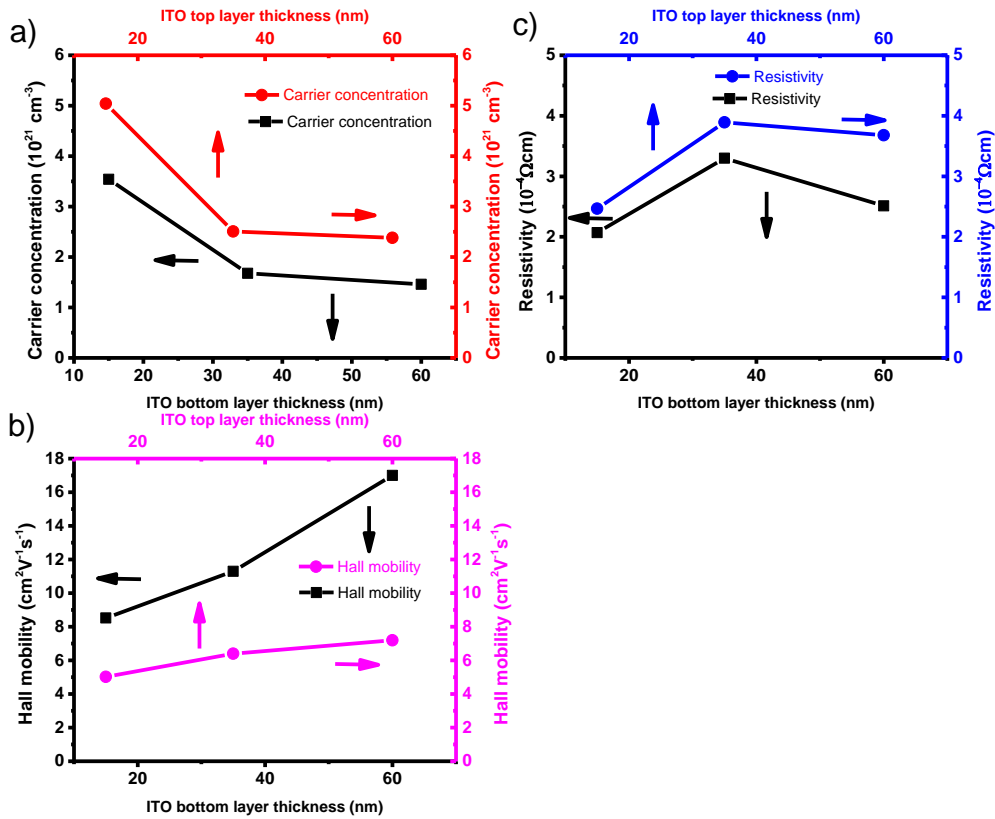


Figure 6-5 The electrical properties of asymmetric samples with only bottom layer thickness increment from 15nm to 60nm (black curve, bottom and left axis), the top ITO and gold layer was kept 5nm and 3nm respectively and only top layer thickness increment from 15nm to 60nm (colored curve, top and right axis), the bottom ITO and gold layer was kept 5nm and 3nm respectively.

Figure 6-6 (a) and (b) plot the overall electrical properties of the two sets of samples as a function of gold layer position, the x-axis indicates the gold layer position shifted from top to bottom. For both samples, the lowest resistivity is achieved when the trilayer structure is symmetric. Even though increasing the top ITO layer thickness can help the increase in carrier concentration in the whole layer, the carrier mobility will decrease generally due to ionized carrier scattering. Thus, resultant resistivity is the trade-off between the carrier concentration and the carrier mobility. Therefore, when the top and bottom ITO thickness is even, the overall resistivity will strike a balance and get an optimal value.

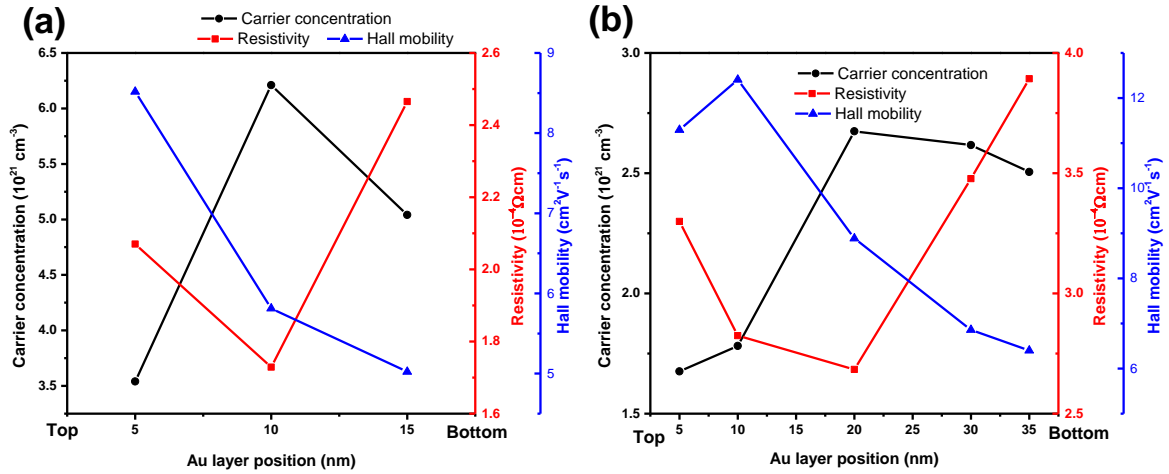


Figure 6-6 carrier concentrations, Hall mobility and resistivity as a function of ITO top layer thickness (a) different top and bottom ITO thicknesses (total thicknesses are 23nm), (b) different top and bottom ITO thicknesses (total thicknesses are 43nm).



6.4 Plasmonic properties tuning in the asymmetric trilayer structures

As shown in previous section, there is still room for further tuning the plasmonic crossover wavelength by changing the position of Au spacer layer. This can be achieved by different thickness of top and bottom ITO. The origin of the tuning effect arisen from the different crystallinity of top and bottom ITO thin films. In previous part, the effective medium approximation had successfully been modelled using the multilayer structures to give the effective permittivity. The red shift of crossover wavelength by moving the position of gold spacer layer is shown in Figure 6-7. Form the Drude-Lorentz model, the crossover frequency is directly proportional to the plasma frequency.[107] Therefore, the crossover wavelength is inversely proportional to carrier concentration. Figure 6-8 (a) and (c) shows the enlarged view of the epsilon-near-zero range of the asymmetric trilayer samples and Figure 6-8 (b) and (d) shows the crossover wavelength as a function of gold spacer positions shifting form the bottom to the top. Because of the different crystallinity of the two ITO layer, the thicker top ITO sandwich film will process high carrier density, the crossover wavelength (a.k.a. the plasma resonance frequency) will be smaller than thicker bottom ITO sample. However, for the symmetric sample, the highest carrier concentration and lowest resistivity do not show the shortest crossover wavelength. The possible reason remains unknown, more jobs will be needed in the near future to verify the possible relationship.

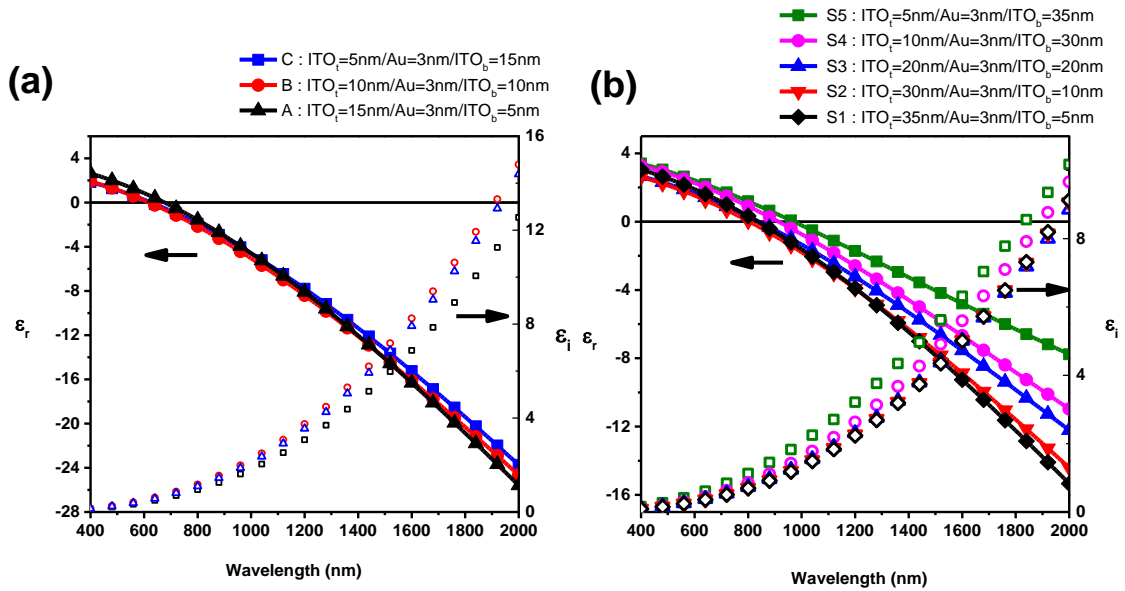


Figure 6-7 effective dielectric constant ϵ_{\perp} with the real part (solid line) and the imaginary part (dashed line) of the trilayer layer samples with different position of gold spacer layer calculated by effective medium approximation (a) different top and bottom ITO thicknesses (total thicknesses are 23nm), (b) different top and bottom ITO thicknesses (total thicknesses are 43nm).

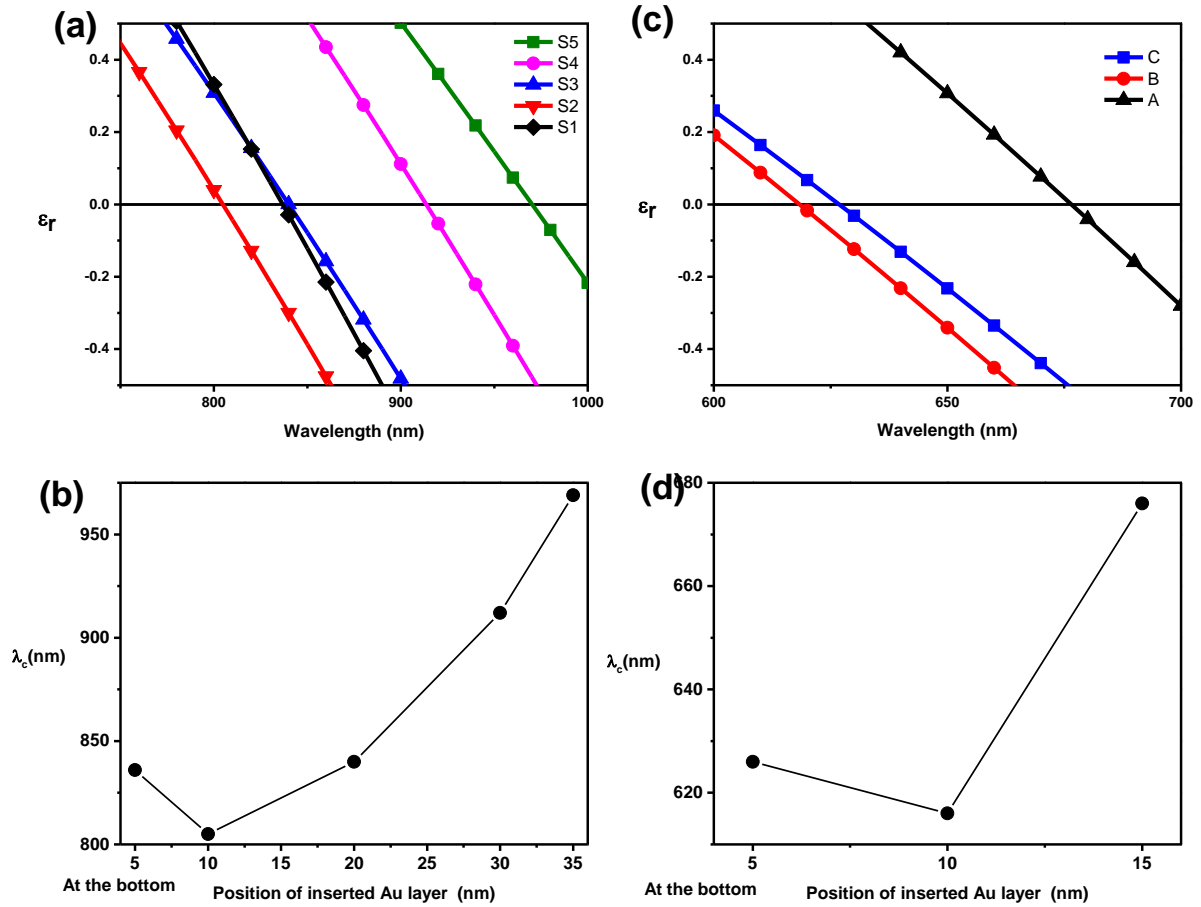


Figure 6-8 (a) Epsilon near zero (ENZ) region of ϵ_{\perp} with the real part (solid line) of the trilayer layer samples with different position of gold spacer layer (total thicknesses are 43nm). (b) crossover wavelength against the position of inserted gold layer (total thicknesses are 43nm). (c) Epsilon near zero (ENZ) region of ϵ_{\perp} with the real part (solid line) of the trilayer layer samples with different position of gold spacer layer (total thicknesses are 23nm). (d) crossover wavelength against the position of inserted gold layer (total thicknesses are 23nm).



7 Conclusion and Future work

To conclude, two jobs have been done in this project related to the transparent materials.

The first part is related to the structural and optical characterization on SBN thin film prepared by pulsed laser deposition. The Gd^{3+} ions have been successfully doped into the pure SBN system which was confirmed by the X-ray diffraction 2-theta measurement, the systematic right shifts of SBN (002) peak with increasing doping concentration showed the contraction on the c-lattice constant due to the Gd^{3+} ions replacement of Sr^{2+} ions on A1 site. Also, the SBN films have grown epitaxially on (100) MgO substrate and Pt (001)/MgO (001) system confirmed by XRD phi scan. The epitaxial in-plane alignment was described as SBN (001)/Pt (320)//MgO (320) and SBN (001)/Pt (220)//MgO (220). Then, the optical constant of SBN thin films was measured by ellipsometry and calculated by Tauc-Lorentz model. The obtained optical constant was verified by comparing with the simulation of the transmittance spectra and the results had good agreement with experimental spectra.

The effect of doping with different concentration of Gd ions from 1% to 4% atomic percentage on the ferroelectric properties on SBN were also studied. The result showed that the gadolinium dopants generally increase remnant polarization compared with the undoped SBN thin film. Especially, the 1% Gd doping concentration sample achieved the highest remnant polarization of with the P_r value about 9 times larger than the undoped sample and 4 times larger than other doped samples. For the device fabrication, the minimum thickness required was about 500nm and the optimal junction area for the ferroelectric device was also studied in order to obtain a better shape of hysteresis loop with less leakage current.

Another part of this thesis focus on the ITO/Au/ITO sandwiched structures were deposited on glass substrates via magnetron sputtering. In the symmetric geometry (the top thickness of ITO film is equal to the bottom ITO film thickness), the thicknesses were increased from 11nm to 55nm, their structural, electrical and optical properties were investigated. By XRD and TEM observation, the crystallinity of top ITO thin film was improved by the inserted gold layer which resulted in different electrical and optical performance compared with the bottom counterparts. For the electrical measurement, the sandwiched structure generally processed better electrical performance compared with those from pure ITO film. For the plasmonic properties, the trilayer structures were estimated by the effective media approximation (EMA)



and got a reliable result to fully evaluate the trilayer plasmonic properties. The plasmonic tuning ability was ranging from 830nm to 1490nm i.e. over 600 nm plasmonic resonance tuning in NIR range. Thus, our result showed these device configurations possessed high application potential in plasmonic devices.

Finally, the last part of this thesis showed that the asymmetric ITO sandwich structure (top thickness of ITO film is different to bottom ITO film thickness), gave the indication on the contribution of the overall electrical performance due to individual layer and compared their electrical performance with the symmetric structure. The plasmonic crossover wavelength for the asymmetric layer provided a further 100nm tuning ability with the symmetric structure.

This research project has shown many potential directions in the future work on the transparent oxide devices. We have demonstrated integration of Gd-doped SBN on a ferroelectric junction. The previous research reported the extraordinary pyroelectric coefficient upon doped Gd in SBN ceramics [17, 18], our GSBN ferroelectric junction may be applied into many pyroelectric thin film devices such as pyroelectric infrared detector or pyroelectric nanogenerator. Furthermore, the investigation on the plasmonic properties on ITO and Au hybrid structure can also couple with the SBN thin film to forming an electro-optic device with better performance.[108]



References

- [1] H. Zimmermann, "Examples of Optoelectronic Integrated Circuits," in *Integrated Silicon Optoelectronics*, H. K. Zimmermann, Ed. Berlin, Heidelberg: Springer Berlin Heidelberg, 2010, pp. 307-353.
- [2] C. Ren *et al.*, "Highly transparent, all-oxide, heteroepitaxy ferroelectric thin film for flexible electronic devices," *Applied Surface Science*, vol. 458, pp. 540-545, 2018/11/15/ 2018.
- [3] D. Sette, S. Girod, R. Leturcq, S. Glinsek, and E. Defay, "Transparent Ferroelectric Capacitors on Glass," *Micromachines*, vol. 8, no. 10, p. 313, 2017.
- [4] F. Bernard, M. Gorisse, F. Casset, C. Chappaz, and S. Basrour, "Design, Fabrication and Characterization of a Tactile Display Based on AlN Transducers," *Procedia Engineering*, vol. 87, pp. 1310-1313, 2014/01/01/ 2014.
- [5] M. Venet, I. A. Santos, J. A. Eiras, and D. Garcia, "Potentiality of SBN textured ceramics for pyroelectric applications," *Solid State Ionics*, vol. 177, no. 5, pp. 589-593, 2006/02/01/ 2006.
- [6] S. Manish, C. Aditya, V. Rahul, and C. Vishal Singh, "Pyroelectric materials for solar energy harvesting: a comparative study," *Smart Materials and Structures*, vol. 24, no. 10, p. 105013, 2015.
- [7] Y. Tan, F. Chen, and H.-J. Zhang, *Optical ridge waveguides in SBN crystal produced by low-dose carbon ion implantation followed by a sputter etching technique*. 2008, pp. 16696-701.
- [8] O. Kwon, O. Eknayan, H. F. Taylor, and R. R. Neurgaonkar, "Low-voltage electro-optic modulator in SBN:60," *Electronics Letters*, vol. 35, no. 3, pp. 219-220, 1999.
- [9] R. R. Neurgaonkar, W. F. Hall, J. R. Oliver, W. W. Ho, and W. K. Cory, "Tungsten bronze Sr_{1-x} Ba_x Nb₂O₆: A case history of versatility," *Ferroelectrics*, vol. 87, no. 1, pp. 167-179, 1988/11/01 1988.
- [10] "Measurement of large electro-optic coefficients in thin films of strontium barium niobate (Sr_{0.6}Ba_{0.4}Nb₂O₆)," *Applied Physics Letters*, vol. 68, no. 23, pp. 3227-3229, 1996.
- [11] J. Koo, C. Lee, J. H. Jang, K. No, and B.-S. Bae, "Measurement of the linear electro-optic coefficients of sol-gel derived strontium barium niobate thin films using a two-beam polarization interferometer," *Applied Physics Letters*, vol. 76, no. 19, pp. 2671-2673, 2000/05/08 2000.
- [12] "Pulsed laser deposition of SBN:75 thin films with electro-optic coefficient of 844 pm/V," *Applied Physics Letters*, vol. 69, no. 8, pp. 1023-1025, 1996.
- [13] "Photorefractive properties of strontium-barium niobate," *Journal of Applied Physics*, vol. 62, no. 2, pp. 374-380, 1987.
- [14] "Low-loss strain induced optical waveguides in strontium barium niobate (Sr_{0.6}Ba_{0.4}Nb₂O₆) at 1.3 μ m wavelength," *Applied Physics Letters*, vol. 66, no. 3, pp. 274-276, 1995.



- [15] M. Said, T. S. Velayutham, W. C. Gan, and W. H. Abd Majid, "The structural and electrical properties of $Sr_xBa_{(1-x)}Nb_2O_6$ (SBN) ceramic with varied composition," *Ceramics International*, vol. 41, no. 5, pp. 7119-7124, 2015.
- [16] O. Malyskhina, V. Lisitsin, A. Movchikova, J. Dec, and T. Lukasiewicz, "The Pyroelectric Properties of SBN Crystals with Different Composition," *Ferroelectrics*, vol. 426, no. 1, pp. 230-235, 2012.
- [17] Y. Yao, C. L. Mak, K. H. Wong, S. Lu, and Z. Xu, "Effects of Rare-Earth Dopants on the Ferroelectric and Pyroelectric Properties of Strontium Barium Niobate Ceramics," *International Journal of Applied Ceramic Technology*, vol. 6, no. 6, pp. 671-678, 2009.
- [18] M. Said, T. S. Velayutham, and W. H. Abd Majid, "Dielectric, pyroelectric, and ferroelectric properties of gadolinium doped $Sr_{0.53}Ba_{0.47}Nb_2O_6$ ceramic," *Ceramics International*, vol. 43, no. 13, pp. 9783-9789, 2017/09/01/ 2017.
- [19] T. S. Velayutham, N. I. F. Salim, W. C. Gan, and W. H. Abd. Majid, "Effect of cerium addition on the microstructure, electrical and relaxor behavior of $Sr_{0.5}Ba_{0.5}Nb_2O_6$ ceramics," *Journal of Alloys and Compounds*, vol. 666, pp. 334-340, 2016/05/05/ 2016.
- [20] H. Liu, S. T. Li, G. K. Liu, W. Jia, and F. E. Fernández, "Optical properties of undoped and Eu^{3+} -doped SBN thin film grown by pulsed laser deposition," *Journal of Luminescence*, vol. 83-84, pp. 367-371, 1999/11/01/ 1999.
- [21] Y. B. Yao, W. C. Liu, C. L. Mak, K. H. Wong, H. L. Tam, and K. W. Cheah, "Optical properties of rare-earth doped epitaxial $Sr_{0.5}Ba_{0.5}Nb_2O_6$ thin films grown by pulsed laser deposition," *Thin Solid Films*, vol. 519, no. 1, pp. 52-57, 2010/10/29/ 2010.
- [22] W. Cao, J. Li, H. Chen, and J. Xue, "Transparent electrodes for organic optoelectronic devices: a review," 2014, vol. 4, p. 28: SPIE.
- [23] X. Q. Gu, L. P. Zhu, L. Cao, Z. Z. Ye, H. P. He, and P. K. Chu, "Optical and electrical properties of ZnO:Al thin films synthesized by low-pressure pulsed laser deposition," *Materials Science in Semiconductor Processing*, vol. 14, no. 1, pp. 48-51, 2011/03/01/ 2011.
- [24] F. J. Serrao and S. M. Dharmaparakash, "Structural, optical and electrical properties of sol-gel prepared Ga:ZnO thin film," *Materials Research Innovations*, vol. 20, no. 6, pp. 470-474, 2016/09/18 2016.
- [25] J. T. Wang *et al.*, "Influence of Preferred Orientation on the Electrical Conductivity of Fluorine-Doped Tin Oxide Films," *Scientific Reports*, vol. 4, p. 3679, 01/14

07/25/received

12/16/accepted 2014.

- [26] A. Eshaghi and A. Graeli, "Optical and electrical properties of indium tin oxide (ITO) nanostructured thin films deposited on polycarbonate substrates "thickness effect"," *Optik - International Journal for Light and Electron Optics*, vol. 125, no. 3, pp. 1478-1481, 2014/02/01/ 2014.
- [27] T. Lin *et al.*, "Electrical study of indium doped magnesium zinc oxide by spray pyrolysis," in *2015 International Symposium on Next-Generation Electronics (ISNE)*, 2015, pp. 1-2.
- [28] R. Biswal, A. Maldonado, J. Vega-Pérez, D. R. Acosta, and M. D. L. L. Olvera, "Indium Doped Zinc Oxide Thin Films Deposited by Ultrasonic Chemical Spray Technique, Starting from Zinc Acetylacetonate and Indium Chloride," *Materials*, vol. 7, no. 7, pp. 5038-5046, 07/04



04/02/received

05/08/revised

05/14/accepted 2014.

- [29] M. Henry, P. M. Harrison, and J. Wendland, "Laser ablation of ITO thin films on glass for flat panel display manufacture," in *Photon*, 2006, vol. 6, pp. 1-6.
- [30] "Transparent heat-mirror films of TiO₂/Ag/TiO₂ for solar energy collection and radiation insulation," *Applied Physics Letters*, vol. 25, no. 12, pp. 693-695, 1974.
- [31] S. Thonglem, U. Intatha, K. Pengpat, G. Rujijanagul, T. Tunkasiri, and S. Eitssayeam, "Electrical and Optical Properties of ITO/Au/ITO Multilayer Films for High Performance TCO Films," *Ferroelectrics*, vol. 457, no. 1, pp. 117-123, 2013.
- [32] A. Indluru and T. L. Alford, "Effect of Ag thickness on electrical transport and optical properties of indium tin oxide–Ag–indium tin oxide multilayers," *Journal of Applied Physics*, vol. 105, no. 12, 2009.
- [33] C. Guillén and J. Herrero, "TCO/metal/TCO structures for energy and flexible electronics," *Thin Solid Films*, vol. 520, no. 1, pp. 1-17, 2011.
- [34] P. Yong-Seok, C. Kwang-Hyuk, and K. Han-Ki, "Room temperature flexible and transparent ITO/Ag/ITO electrode grown on flexible PES substrate by continuous roll-to-roll sputtering for flexible organic photovoltaics," *Journal of Physics D: Applied Physics*, vol. 42, no. 23, p. 235109, 2009.
- [35] S.-H. Choa, C.-K. Cho, W.-J. Hwang, K. Tae Eun, and H.-K. Kim, "Mechanical integrity of flexible InZnO/Ag/InZnO multilayer electrodes grown by continuous roll-to-roll sputtering," *Solar Energy Materials and Solar Cells*, vol. 95, no. 12, pp. 3442-3449, 2011/12/01/ 2011.
- [36] Y. Xu, *Ferroelectric materials and their applications*. Elsevier, 2013.
- [37] D. Dragan, "Ferroelectric, dielectric and piezoelectric properties of ferroelectric thin films and ceramics," *Reports on Progress in Physics*, vol. 61, no. 9, p. 1267, 1998.
- [38] I. Chilibon and J. N. Marat-Mendes, "Ferroelectric ceramics by sol–gel methods and applications: a review," *Journal of Sol-Gel Science and Technology*, journal article vol. 64, no. 3, pp. 571-611, December 01 2012.
- [39] A. A. Bokov and Z.-G. Ye, "Recent progress in relaxor ferroelectrics with perovskite structure," *Journal of Materials Science*, journal article vol. 41, no. 1, pp. 31-52, January 01 2006.
- [40] Y.-Q. Qu *et al.*, "Structure and electrical properties of strontium barium niobate ceramics," *Materials Research Bulletin*, vol. 37, no. 3, pp. 503-513, 2002/03/01/ 2002.
- [41] M. Said, T. S. Velayutham, W. C. Gan, and W. H. Abd Majid, "The structural and electrical properties of Sr_xBa(1-x)Nb₂O₆ (SBN) ceramic with varied composition," *Ceramics International*, vol. 41, no. 5, Part B, pp. 7119-7124, 2015/06/01/ 2015.
- [42] F. Guerrero, J. Portelles, H. Amorín, F. Abel, J. Siqueiros, and G. Hirata, *Sintering characteristics of the LSBN ceramics and influence of the Lanthanum content*. 1998, pp. 745-749.
- [43] I. A. Kaurova, G. M. Kuz'micheva, L. I. Ivleva, V. V. Chernyshev, V. B. Rybakov, and E. N. Domoroshchina, "X-ray powder diffraction methods for the determination of composition and structural parameters of Cr- and Ni-doped Sr_{0.61}Ba_{0.39}Nb₂O₆ crystals," *Journal of Alloys and Compounds*, vol. 638, pp. 159-165, 2015.



- [44] X. Fang, C. L. Mak, S. Y. Zhang, Z. W. Wang, W. J. Yuan, and H. Ye, "Pulsed laser deposited indium tin oxides as alternatives to noble metals in the near-infrared region," (in English), *Journal of Physics-Condensed Matter*, vol. 28, no. 22, Jun 8 2016.
- [45] E. Terzini, P. Thilakan, and C. Minarini, "Properties of ITO thin films deposited by RF magnetron sputtering at elevated substrate temperature," *Materials Science and Engineering: B*, vol. 77, no. 1, pp. 110-114, 2000/08/07/ 2000.
- [46] M. Chuang, "ITO Films Prepared by Long-throw Magnetron Sputtering without Oxygen Partial Pressure," *Journal of Materials Science & Technology*, vol. 26, no. 7, pp. 577-583, 2010/07/01/ 2010.
- [47] O. N. Mryasov and A. J. Freeman, "Electronic band structure of indium tin oxide and criteria for transparent conducting behavior," *Physical Review B*, vol. 64, no. 23, p. 233111, 12/03/ 2001.
- [48] J. J. Lin and Z. Q. Li, "Electronic conduction properties of indium tin oxide: single-particle and many-body transport," *J Phys Condens Matter*, vol. 26, no. 34, p. 343201, Aug 27 2014.
- [49] R. B. H. Tahar, T. Ban, Y. Ohya, and Y. Takahashi, "Tin doped indium oxide thin films: Electrical properties," *Journal of Applied Physics*, vol. 83, no. 5, pp. 2631-2645, 1998.
- [50] K. Reichelt, "Nucleation and growth of thin films," *Vacuum*, vol. 38, no. 12, pp. 1083-1099, 1988/01/01/ 1988.
- [51] M. Fox, *Optical Properties of Solids*. OUP Oxford, 2010.
- [52] O. Stenzel, *The Physics of Thin Film Optical Spectra: An Introduction*. Springer International Publishing, 2015.
- [53] M. Said, T. S. Velayutham, and W. H. Abd Majid, "Dielectric, pyroelectric, and ferroelectric properties of gadolinium doped Sr 0.53 Ba 0.47 Nb 2 O 6 ceramic," *Ceramics International*, vol. 43, no. 13, pp. 9783-9789, 2017.
- [54] H. Kim, T. E. Sutto, and A. Piqué, "Laser materials processing for micropower source applications: a review," *Journal of Photonics for Energy*, vol. 4, no. 1, 2014.
- [55] V. A. Dao *et al.*, "rf-Magnetron sputtered ITO thin films for improved heterojunction solar cell applications," *Current Applied Physics*, vol. 10, no. 3, pp. S506-S509, 2010.
- [56] H. Sun, M. Yu, G. Wang, X. Sun, and J. Lian, "Temperature-Dependent Morphology Evolution and Surface Plasmon Absorption of Ultrathin Gold Island Films," *The Journal of Physical Chemistry C*, vol. 116, no. 16, pp. 9000-9008, 2012.
- [57] L. Reimer, *Scanning Electron Microscopy: Physics of Image Formation and Microanalysis*. Springer Berlin Heidelberg, 2013.
- [58] Y. Liu, R. Wang, X. Guo, and J. Dai, "A cross-sectional TEM sample preparation method for films deposited on metallic substrates," *Materials Characterization*, vol. 58, no. 7, pp. 666-669, 2007/07/01/ 2007.
- [59] J. G. E. Jellison, "Spectroscopic ellipsometry data analysis: measured versus calculated quantities," *Thin Solid Films*, vol. 313-314, pp. 33-39, 1998/02/13/ 1998.
- [60] H. Fujiwara, *Spectroscopic Ellipsometry: Principles and Applications*. Wiley, 2007.
- [61] D. Salazar, R. Soto-Molina, E. Lizarraga-Medina, M. Felix, N. Radnev, and H. Márquez, "Ellipsometric Study of SiO_x Thin Films by Thermal Evaporation," *Open Journal of Inorganic Chemistry*, vol. 6, pp. 175-182, 2016.



- [62] J. A. Woollam, P. G. Snyder, and M. C. Rost, "Variable angle spectroscopic ellipsometry: A non-destructive characterization technique for ultrathin and multilayer materials," *Thin Solid Films*, vol. 166, pp. 317-323, 1988/12/01/ 1988.
- [63] L. J. Van der Pauw, "A METHOD OF MEASURING THE RESISTIVITY AND HALL COEFFICIENT ON LAMELLAE OF ARBITRARY SHAPE," *Phil. Tech. Rev.*, vol. 20, pp. 220-224, 1958.
- [64] C. B. Sawyer and C. H. Tower, "Rochelle Salt as a Dielectric," *Physical Review*, vol. 35, no. 3, pp. 269-273, 02/01/ 1930.
- [65] I. A. Santos, D. Garcia, and J. A. Eiras, "Pyroelectric properties of rare earth doped strontium barium niobate ceramics from 20K to 450K," *Ferroelectrics*, vol. 257, no. 1, pp. 105-110, 2001.
- [66] P. V. Lenzo, E. G. Spencer, and A. A. Ballman, "Electro-Optic Coefficients of Ferroelectric Strontium Barium Niobate," *Applied Physics Letters*, vol. 11, no. 1, pp. 23-24, 1967.
- [67] M. D. Ewbank, R. R. Neurgaonkar, W. K. Cory, and J. Feinberg, "Photorefractive properties of strontium-barium niobate," *Journal of Applied Physics*, vol. 62, no. 2, pp. 374-380, 1987.
- [68] S. Schwyn Thöny, K. E. Youden, J. S. Harris, and L. Hesselink, "Growth of epitaxial strontium barium niobate thin films by pulsed laser deposition," *Applied Physics Letters*, vol. 65, no. 16, pp. 2018-2020, 1994.
- [69] A. Infortuna, P. Muralt, M. Cantoni, and N. Setter, "Epitaxial growth of (SrBa)Nb₂O₆ thin films on SrTiO₃ single crystal substrate," *Journal of Applied Physics*, vol. 100, no. 10, 2006.
- [70] I. V., G. A. C., S. N. D., F. M., and D. M., "Spectroscopic ellipsometry study of amorphous Sr_x Ba_{1-x} Nb₂O₆ thin films obtained by pulsed laser deposition," *physica status solidi c*, vol. 5, no. 5, pp. 1180-1183, 2008.
- [71] W. Th., G. T., D. U., P. Ch., W. M., and P. R., "Refractive Indices of Congruently Melting Sr_{0.61}Ba_{0.39}Nb₂O₆," *physica status solidi (a)*, vol. 186, no. 1, pp. R13-R15, 2001.
- [72] V. Ion, A. Andrei, M. Dinescu, and N. D. Scarisoreanu, "Optical Properties of Complex Oxide Thin Films Obtained by Pulsed Laser Deposition," in *Laser Ablation - From Fundamentals to Applications*, 2017.
- [73] Y. H. Gao *et al.*, "Surface chemical composition and optical properties of nitrogen-doped Ba_{0.6}Sr_{0.4}TiO₃ thin films," *Journal of Applied Physics*, vol. 102, no. 6, 2007.
- [74] "Parameterization of the optical functions of amorphous materials in the interband region," *Applied Physics Letters*, vol. 69, no. 3, pp. 371-373, 1996.
- [75] D. A. Anderson and W. E. Spear, "Electrical and optical properties of amorphous silicon carbide, silicon nitride and germanium carbide prepared by the glow discharge technique," *The Philosophical Magazine: A Journal of Theoretical Experimental and Applied Physics*, vol. 35, no. 1, pp. 1-16, 1977/01/01 1977.
- [76] S. Savaş, A. Aysun, S. Tülay, and S. Necmi, "The effects of film thickness on the optical properties of TiO₂-SnO₂ compound thin films," *Physica Scripta*, vol. 84, no. 6, p. 065602, 2011.
- [77] C. David, A. Tunyagi, K. Betzler, and M. Wöhlecke, "Compositional dependence of optical and vibrational properties of strontium barium niobate (Sr_x Ba_{1-x} Nb₂O₆)," *physica status solidi (b)*, vol. 244, no. 6, pp. 2127-2137, 2007.



- [78] P. C. McIntyre, C. J. Maggiore, and M. Nastasi, "Orientation selection in thin platinum films on (001) MgO," *Journal of Applied Physics*, vol. 77, no. 12, pp. 6201-6204, 1995.
- [79] T.-Y. Yum, C.-L. Mak, and K.-H. Wong, "Fabrication and characterization of epitaxial Sr_{0.6}Ba_{0.4}Nb₂O₆/La_{0.7}Sr_{0.3}CoO₃ heterostructures," *Applied Surface Science*, vol. 252, no. 13, pp. 4829-4833, 2006/04/30/ 2006.
- [80] S. Vigne *et al.*, "Optical properties of epitaxial Ca_xBa_{1-x}Nb₂O₆ thin film based rib-waveguide structure on (001) MgO for electro-optic applications," *Opt Express*, vol. 24, no. 25, pp. 28573-28582, Dec 12 2016.
- [81] P. R. Willmott, R. Herger, B. D. Patterson, and R. Windiks, "Experimental and theoretical study of the strong dependence of the microstructural properties of Sr_xBa_{1-x}Nb₂O₆ thin films as a function of their composition," *Physical Review B*, vol. 71, no. 14, 2005.
- [82] M. J. Nystrom, B. W. Wessels, W. P. Lin, G. K. Wong, D. A. Neumayer, and T. J. Marks, "Nonlinear optical properties of textured strontium barium niobate thin films prepared by metalorganic chemical vapor deposition," *Applied Physics Letters*, vol. 66, no. 14, pp. 1726-1728, 1995.
- [83] P. Venkata Sreenivas *et al.*, "Nanoscale polarisation switching and leakage currents in (Ba_{0.955}Ca_{0.045})(Zr_{0.17}Ti_{0.83})O₃ epitaxial thin films," *Journal of Physics D: Applied Physics*, vol. 48, no. 35, p. 355502, 2015.
- [84] Masruroh and M. Toda, "Asymmetric Hysteresis Loops, Leakage Current and Capacitance Voltage Behaviors in Ferroelectric PZT Films Deposited on a Pt/Al₂O₃/SiO₂/Si Substrate by MOCVD method with a vapor-deposited Gold Top Electrode," *International Journal of Applied Physics and Mathematics*, vol. 1, no. 2, pp. 144-148, 2011.
- [85] W. Cao, "The strain limits on switching," *Nature Materials*, vol. 4, p. 727, 10/01/online 2005.
- [86] W. Lee *et al.*, "Improved Initial Growth Behavior of SrO and SrTiO₃ Films Grown by Atomic Layer Deposition Using {Sr(demamp)(tmhd)}₂ as Sr-Precursor," *Chemistry of Materials*, vol. 27, no. 11, pp. 3881-3891, 2015/06/09 2015.
- [87] X. Xiaofei, J. Limei, and Z. Yichun, "Reduction of leakage currents in ferroelectric thin films by flexoelectricity: a phase field study," *Smart Materials and Structures*, vol. 26, no. 11, p. 115024, 2017.
- [88] T. Kiba *et al.*, "Emission enhancement in indium zinc oxide(IZO)/Ag/IZO sandwiched structure due to surface plasmon resonance of thin Ag film," *Applied Surface Science*, vol. 389, pp. 906-910, 2016.
- [89] T. Tumkur, G. Zhu, P. Black, Y. A. Barnakov, C. E. Bonner, and M. A. Noginov, "Control of spontaneous emission in a volume of functionalized hyperbolic metamaterial," *Applied Physics Letters*, vol. 99, no. 15, 2011.
- [90] X. Fang, C. L. Mak, J. Y. Dai, K. Li, H. Ye, and C. W. Leung, "ITO/Au/ITO Sandwich Structure for Near-Infrared Plasmonics," (in English), *Acs Applied Materials & Interfaces*, vol. 6, no. 18, pp. 15743-15752, Sep 24 2014.
- [91] X. Fang, C. L. Mak, J. Dai, K. Li, H. Ye, and C. W. Leung, "ITO/Au/ITO sandwich structure for near-infrared plasmonics," *ACS Appl Mater Interfaces*, vol. 6, no. 18, pp. 15743-52, Sep 24 2014.



- [92] B. Ren, X. Liu, M. Wang, and Y. Xu, "Preparation and characteristics of indium tin oxide (ITO) thin films at low temperature by r.f. magnetron sputtering," *Rare Metals*, vol. 25, no. 6, Supplement 1, pp. 137-140, 2006/10/01/ 2006.
- [93] K. Carl, H. Schmitt, and I. Friedrich, "Optimization of sputtered ITO films with respect to the oxygen partial pressure and substrate temperature," *Thin Solid Films*, vol. 295, no. 1, pp. 151-155, 1997/02/28/ 1997.
- [94] H. H, T. ND, and A. TL, "Improved conductivity and mechanism of carrier transport in zinc oxide with embedded silver layer," *Journal of Applied Physics*, vol. 103, no. 1, p. 013708, 2008.
- [95] Y. S. Kim *et al.*, "ITO/Au/ITO multilayer thin films for transparent conducting electrode applications," *Applied Surface Science*, vol. 254, no. 5, pp. 1524-1527, 2007/12/30/ 2007.
- [96] "Electrical, optical, and structural properties of indium–tin–oxide thin films for organic light-emitting devices," *Journal of Applied Physics*, vol. 86, no. 11, pp. 6451-6461, 1999.
- [97] M. Losurdo *et al.*, *Parametrization of optical properties of indium-tin-oxide thin films by spectroscopic ellipsometry: Substrate interfacial reactivity*. 2002, pp. 37-42.
- [98] P. R. West, S. Ishii, G. V. Naik, N. K. Emani, V. M. Shalaev, and A. Boltasseva, "Searching for better plasmonic materials," (in English), *Laser & Photonics Reviews*, vol. 4, no. 6, pp. 795-808, Nov 2010.
- [99] G. V. Naik, V. M. Shalaev, and A. Boltasseva, "Alternative Plasmonic Materials: Beyond Gold and Silver," *Advanced Materials*, vol. 25, no. 24, pp. 3264-3294, 2013.
- [100] V. Teixeira, H. N. Cui, L. J. Meng, E. Fortunato, and R. Martins, "Amorphous ITO thin films prepared by DC sputtering for electrochromic applications," *Thin Solid Films*, vol. 420-421, pp. 70-75, 2002/12/02/ 2002.
- [101] V. M. Agranovich and V. E. Kravtsov, "NOTES ON CRYSTAL OPTICS OF SUPERLATTICES," *Solid State Communications*, vol. 55, no. 1, pp. 85-90, 1985.
- [102] G. V. Naik, V. M. Shalaev, and A. Boltasseva, "Alternative plasmonic materials: beyond gold and silver," *Adv Mater*, vol. 25, no. 24, pp. 3264-94, Jun 25 2013.
- [103] A. Calzolari, A. Ruini, and A. Catellani, "Transparent Conductive Oxides as Near-IR Plasmonic Materials: The Case of Al-Doped ZnO Derivatives," *ACS Photonics*, vol. 1, no. 8, pp. 703-709, 2014/08/20 2014.
- [104] "Effect of film thickness on the properties of indium tin oxide thin films," *Journal of Applied Physics*, vol. 88, no. 10, pp. 6021-6025, 2000.
- [105] "Physical properties of antimony-doped tin oxide thick films," *Journal of Applied Physics*, vol. 53, no. 5, pp. 3629-3633, 1982.
- [106] "Improved conductivity and mechanism of carrier transport in zinc oxide with embedded silver layer," *Journal of Applied Physics*, vol. 103, no. 1, p. 013708, 2008.
- [107] G. V. Naik, J. Kim, and A. Boltasseva, "Oxides and nitrides as alternative plasmonic materials in the optical range [Invited]," *Optical Materials Express*, vol. 1, no. 6, pp. 1090-1099, 2011/10/01 2011.
- [108] Z. Ma, Z. Li, K. Liu, C. Ye, and J. Sorger Volker, "Indium-Tin-Oxide for High-performance Electro-optic Modulation," in *Nanophotonics* vol. 4, ed, 2015, p. 198.